NOVEL APPLICATIONS OF PLASMA ACTUATORS

By

ARZU CEREN ÖZTÜRK

Bachelor of Science in Aerospace Engineering
Middle East Technical University
Ankara, TURKEY
2007

Submitted to the Faculty of the
Graduate College of
Oklahoma State University
in partial fulfillment of
the requirements for
the Degree of
MASTER OF SCIENCE
May, 2009

NOVEL APPLICATIONS OF PLASMA ACTUATORS

Thesis Approved:

Dr. Jamey Jacob

Thesis Advisor

Dr. Andrew Arena

Dr. Frank Chambers

Dr. A. Gordon Emslie

Dean of the Graduate College

ACKNOWLEDGMENTS

I have had the opportunity and pleasure of working with and learning from an advisor who not only cares to share his immense knowledge, but also the learning experience that comes along with his endless new ideas. So thank you, Dr. Jamey Jacob, for being contagiously eager to try things while teaching in the greatest possible way; I have been most comfortable asking what I did not know and have learned more than I could ever have imagined.

I would also like to thank Dr. Andrew Arena and Dr. Frank Chambers for being part of my committee, taking the time to put in their valuable ideas during my defense and helping me see a different perspective to improve my work.

Many thanks go to my lab partners Michael Bolitho, Nathan Lunsford, Ben Loh, Eric Johnson, Craig Williamson, Jacob Weierman, Shawn Fleming and Jeremy Hill for reaching out with a hand whenever I needed one throughout the period of this research.

People who study away from home know how hard it can get sometimes, so there is not too much to say to these people for they are the dearest to my heart and get the biggest thanks; my parents, family and friends who are the major contributors to me and my achievements. Thank you for the unconditional love, support and endless belief in me as a person; you were all so far, yet so near..

TABLE OF CONTENTS

Chapter Page

1 Introduction 1

2 Previous Work 6

2.1 Flow Control 6

2.1.1 Vortex Generator Jets and Other Mass Flux Devices 7

2.1.2 Synthetic Jets 9

2.1.3 Plasma Actuators 12

2.2 General Plasma Actuator Characteristics 16

2.2.1 Force Measurements 20

2.3 Plasma Synthetic Jet Actuators (PSJAs) 22

2.3.1 Thrust Vectoring Plasma Actuators 24

3 Experimental Arrangement 26

3.1 Plasma Actuator Configurations 26

3.2 Input Signal & Power Calculations 27

3.3 PIV Measurements 31

3.4 Benchtop Setup 33

3.5 Wind Tunnel Setup 34

4 Plasma Thruster 38

4.1 Single Thruster Configuration 38

4.1.1 Benchtop Tests 38

4.1.2 Wind Tunnel Tests 58

4.2 Thruster Configuration in Staged Arrays 72
4.3 Power Calculations 75

5 Jet Vectoring Plasma Actuator **81**

6 Conclusions **112**

A Input Files and MATLAB Scripts **117**
A.1 WaLPT Input File 117
A.2 MATLAB Scripts 119
A.2.1 Mask Generation 119
A.2.2 Post-processing 120

LIST OF FIGURES

Figure Page

1.1 Co and counter-flow plasma actuator configurations. 3

1.2 Linear plasma actuator. 4

1.3 Plasma thruster. 4

1.4 Jet vectoring plasma actuator. 5

1.5 Co-flow, counter-flow and jet vectoring actuator configurations. 5

2.1 Classification of flow control techniques. 7

2.2 Synthetic Jet. 10

2.3 Plasma synthetic jet actuator. 23

2.4 Flow structure of the PSJA during pulsed actuation. 23

2.5 Linear plasma synthetic jet actuator. 25

3.1 Front & side views of the plasma thruster. 27

3.2 End view of the plasma on the interior duct wall. 28

3.3 Jet vectoring plasma actuator. 28

3.4 Block diagram in Labview for two channel control. 29

3.5 Schematic of experimental setup. 30

3.6 Schematic of alternative setup for the jet vectoring actuator. 30

3.7 Schematic of PIV setup. 32

3.8 PIV setup. 33

3.9 Plasma actuator mounted on benchtop inside transparent container. . 34

3.10 Benchtop setup. 34

3.11 Raw PIV image from benchtop experiments. 35

3.12 Schematic of experimental setup for the wind tunnel. 36
3.13 Raw PIV image from wind tunnel experiments. 37

4.1 Qualitative flow visualization of the flow structure using laser sheet illuminated smoke particles. 43
4.2 Maximum & mean velocities for tubes of inner diameter 1.27 cm, 1.016 cm and 0.635 cm with 100% DC. 44
4.3 Maximum & mean velocities for tubes of inner diameter 1.27 cm, 1.016 cm and 0.635 cm. 45
4.4 Effect of DC on the maximum & mean velocity distribution. 46
4.5 Thrust, maximum velocity and mean velocity distribution with forcing frequency at 50% DC. 47
4.6 Thrust, maximum velocity and mean velocity distribution for d_i=0.635 cm. 48
4.7 Thrust, maximum velocity and mean velocity distribution for d_i=1.016 cm. 49
4.8 Thrust, maximum velocity and mean velocity distribution for d_i=1.27 cm. 50
4.9 Velocity profiles at various downstream x-locations with 100% DC. . . 51
4.10 Streamlines for tubes of 1.27 cm and 3.048 cm inner diameters. 52
4.11 Formation and advection of vortex ring with time for the 1.27 inner diameter tube. 53
4.12 Labview block diagram for phase-locked PIV measurements. 54
4.13 Hodograph for tube of inner diameter 1.27 cm at 5 Hz and 50% DC. . 54
4.14 Interior view of the jet formation using a 2D experimental model. . . 55
4.15 Streamwise distribution of non-dimensional jet characteristics for d_i=0.635 cm. 61

4.16 Streamwise distribution of non-dimensional jet characteristics for d_i=1.016 cm. 62
4.17 Streamwise distribution of non-dimensional jet characteristics for d_i=1.27 cm. 63
4.18 Streamwise distribution of non-dimensional jet characteristics for d_i=1.524 cm. 64
4.19 Streamwise distribution of non-dimensional jet characteristics for d_i=2.159 cm. 65
4.20 Streamwise distribution of non-dimensional jet characteristics for d_i=3.048 cm. 66
4.21 Velocity profiles for the tube with d_i=1.016 cm at tunnel speeds of 0.62 m/s, 1.28 m/s and 2.32 m/s. 67
4.22 Velocity profiles for the tube with d_i=1.524 cm at tunnel speeds of 0.62 m/s, 1.28 m/s and 2.32 m/s. 68
4.23 Velocity profiles for the tube with d_i=3.048 cm at tunnel speeds of 0.62 m/s, 1.28 m/s and 2.32 m/s. 69
4.24 Variation of maximum and mean velocities with wind tunnel speed. . 70
4.25 Variation of thrust and power coefficients with *Re* for different inner diameter thrusters. 71
4.26 Plasma thruster in staged arrays. 72
4.27 The effect of staged arrays & pulsed actuation on the maximum velocities for 50% DC. 74
4.28 Maximum velocity vs. forcing frequency for a single and four stage plasma thruster of d_i=1.27 cm. 75
4.29 Current and voltage output measurements using the Minipuls2 Circuit Board. 76

4.30 Current and voltage output measurements using the CMI 5012 transformers. 77
4.31 Variation of the ratio of average plasma induced and exit velocities with $\left(\frac{h}{r_i}\right)$. 80
4.32 Variation of the efficiency of the thrusters with inner diameter. 80

5.1 3-D smokewire flow visualization in freestream for the jet vectoring plasma actuator. 88
5.2 2-D smokewire flow visualization in freestream for the jet vectoring actuator. 89
5.3 Hotwire measurements for the jet vectoring actuator with both sides at 50% DC. 90
5.4 Variation of absolute maximum vorticity with changing duty cycles in both channels. 91
5.5 Effect of yaw angle on vortex strength. 91
5.6 Circulation vs. radius for varying duty cycles in both channels. 92
5.7 Circulation calculation using velocity vs. vorticity for the 50%/0% DC case. 93
5.8 Hodograph for jet vectoring actuator with varying duty cycles in both channels. 93
5.9 Expected hodograph for jet vectoring actuator with equal plasma strength on both sides. 94
5.10 Streamlines and vorticity contours for jet vectoring with 50%/0% DC for the left and right channels, respectively. 94
5.11 Streamlines and vorticity contours for jet vectoring with 50%/10% DC for the left and right channels, respectively. 95
5.12 Streamlines and vorticity contours for jet vectoring with 50%/20% DC for the left and right channels, respectively. 95

5.13 Streamlines and vorticity contours for jet vectoring with 50%/30% DC for the left and right channels, respectively. 96
5.14 Streamlines and vorticity contours for jet vectoring with 50%/40% DC for the left and right channels, respectively. 96
5.15 Streamlines and vorticity contours for jet vectoring with 50%/50% DC for the left and right channels, respectively. 97
5.16 Streamlines and vorticity contours for jet vectoring with 40%/50% DC for the left and right channels, respectively. 97
5.17 Streamlines and vorticity contours for jet vectoring with 30%/50% DC for the left and right channels, respectively. 98
5.18 Streamlines and vorticity contours for jet vectoring with 20%/50% DC for the left and right channels, respectively. 98
5.19 Streamlines and vorticity contours for jet vectoring with 10%/50% DC for the left and right channels, respectively. 99
5.20 Streamlines and vorticity contours for jet vectoring with 0%/50% DC for the left and right channels, respectively. 99
5.21 Variation of vortex strength and position with chord location for both channels at 50% DC. 100
5.22 Circulation vs. radius with varying chord location for both channels at 50% DC. 101
5.23 Circulation vs. chord location for both channels at 50% DC. 101
5.24 Formation of separate vortices along the streamwise direction. 102
5.25 Evolution of the vortex structure along the chord length for both channels at 50% DC. 103
5.26 3-D view of the field at various chord lengths for both channels at 50% DC. 104

5.27 Variation of vortex strength and position with chord location for one channel at 10% DC and the other at 50% DC. 105
5.28 Circulation vs. radius with varying chord location for one channel at 10% DC and the other at 50% DC. 106
5.29 Absolute circulation vs. chord location for one channel at 10% DC and the other at 50% DC. 106
5.30 Evolution of the vortex structure along the chord length for one channel at 10% DC and the other at 50% DC. 107
5.31 3-D view of the field at various chord lengths for one channel at 10% DC and the other at 50% DC. 108
5.32 Schematic of the actuators on the wing with NACA 0012 airfoil for the tunnel tests. 108
5.33 Field of view over the airfoil. 109
5.34 Reverse flow probability on the NACA 0012 airfoil with 0.62 m/s tunnel speed and a.o.a=10 degrees. 110
5.35 Reverse flow probability on the NACA 0012 airfoil with 1.28 m/s tunnel speed and a.o.a=10 degrees. 111

6.1 Effect of length-to-diameter ratio on the velocity profiles. 114
6.2 Unsteady jet vectoring by varying the duty cycles of the two channels with respect to each other. 116

CHAPTER 1

Introduction

Aerodynamic flow control is vitally important, particularly at low Re and high angles of attack, where separation over airfoils causes a significant increase in drag and decrease in lift. Flow control may reduce separation, thus changes in lift and drag can be minimized while aerodynamic noise produced by the aircraft and the engines can also be reduced. Popular applications consist of laminar separation control with leading edge devices, dynamic stall or separation control of low-pressure turbine blades arising from operation at low Re. Similarly, for μavs and $n$avs, the range of Re is very small and the relevant physics are hard to predict. Thus, flow control is important in terms of the fact that it improves the aerodynamic performance and enhances the flight envelope of these vehicles. Most flow control is achieved by modifying the boundary layer with devices such as vortex generator jets, synthetic jets and plasma actuators, the latter to be addressed in detail herein.

Plasma actuators are zero-net mass flux (ZNMF) devices that use atmospheric pressure electrical discharges, a class which includes corona discharges, dielectric barrier discharges (DBDs), glow discharges and arc discharges. Single DBD plasma actuators typically consist of an arrangement of two horizontally offset electrodes separated by dielectric material, seen in Fig. 1.2. Under input of a high voltage, high frequency AC or pulsed DC signal, a region of dielectric barrier discharge plasma is created in the interfacial air gap that generates a body force on the surrounding air. This results in the formation of a wall jet within the near wall boundary layer that can be used in applications such as separation control in low Re flows through the

generation of near-wall momentum and turbulence. [1–7] The geometric arrangement of the actuators determines the type of the jet while the induced body force or the intensity of the jet is dependent upon the input power, dielectric material, dielectric thickness, the separation distance between the electrodes and the electrode thickness.

Plasma actuators have a wide range of use, all of which depend on the configuration of the actuator. For applications such as separation flow control, a single linear plasma actuator works well, but this configuration can be modified as in Fig. 1.1 wherein the actuator has a significantly higher impact. Counter-flow actuators have been found to be more efficient in eliminating separation in certain cases, especially when used as leading edge devices to trip the flow. Nonlinear configurations that would suit the needs of a micro jet with two actuators in annular configuration and zero-net mass flux injection can also be considered. [8, 9] Similar to other plasma actuators, each of the two actuators is driven by a high voltage, high frequency signal, keeping in mind that the two inner electrodes should be of the same voltage potential to prevent arcing between the two actuators. The actuators are arranged such that they act in the same streamwise direction as one another, thus directing flow outward and producing a jet.

This study consists of various applications of plasma actuators in two different configurations; the first is the use of these actuators in an annular geometry for micro and nano aerial vehicles (μAVs and nAVs, respectively). The range of Re is very small and the subsequent aerodynamics are in a region of relatively unknown physics. Development of suitable propulsion systems will involve the integration of a reliable power source with sufficient energy and power density to carry out a mission. The propulsion system must be capable of demonstrating highly efficient conversion of stored energy to thrust to propel the vehicle in both hover and forward flight. Thus, highly efficient actuators are required for nano air vehicle designs.

In the current experiments, an annular plasma actuator wherein the external

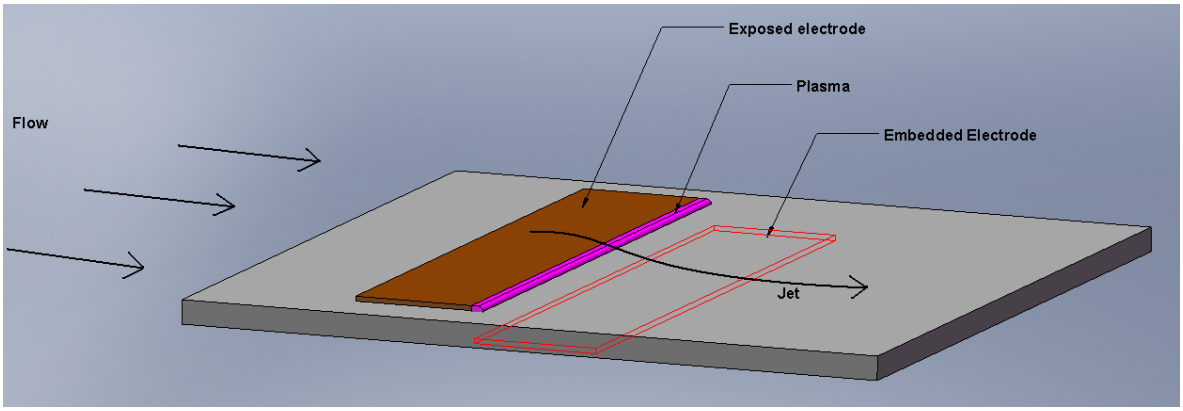

(a) Co-flow

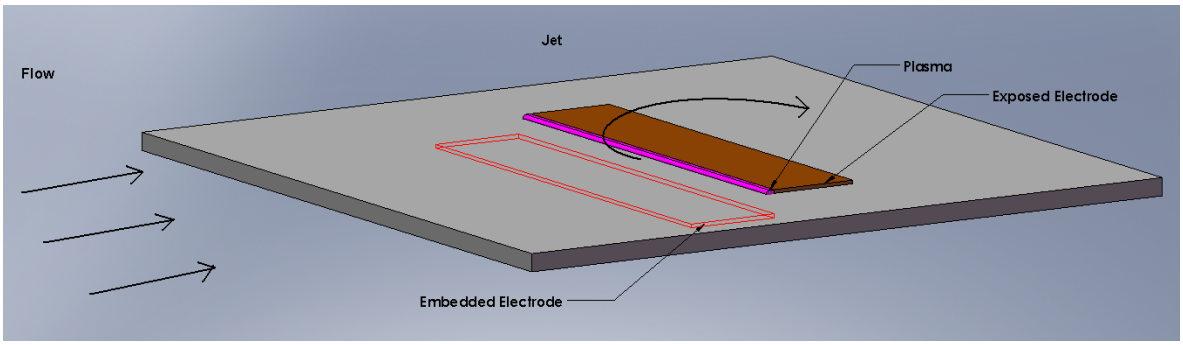

(b) Counter-flow

Figure 1.1: Co and counter-flow plasma actuator configurations.

electrode takes the place of the conventional embedded electrode is used to drive an internal flow, as can be seen in Fig. 1.3. This results in a zero-net mass flux micro thruster with no moving parts.

To increase the effectiveness that plasma actuators can have on flow fields, various actuator geometries that leverage the plasma induced jet are investigated as a second objective, most notably synthetic jet like flows with vectoring capability. These configurations can be used to generate cross- stream vortices similar to pulsed vortex generator jets, shown in Fig. 1.4. Other potential uses of these actuators are demonstrated in Fig. 1.5 where, as mentioned previously, a single actuator design can be used for co-flow, counter-flow and the jet vectoring synthetic jet flow control. It could be seen in the figure that the jet vectoring actuators can also be used as flaps

when placed along the trailing edge. Coupled with an intelligent flow monitoring system, these actuators would have the ability to modify their behavior to best suit the requirements for flow control and/or maneuvering, particularly well suited for aerodynamic flow control at the μAV/nAV scale.

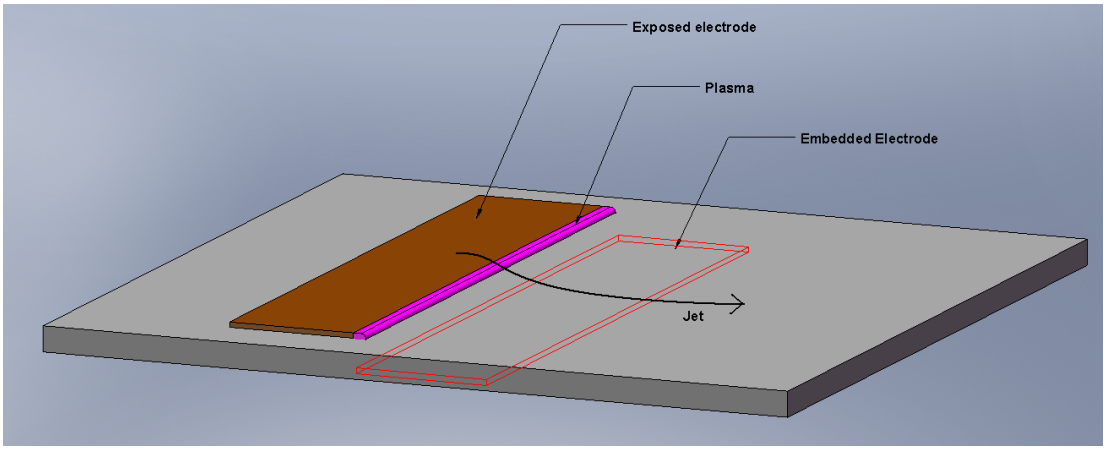

Figure 1.2: Linear plasma actuator.

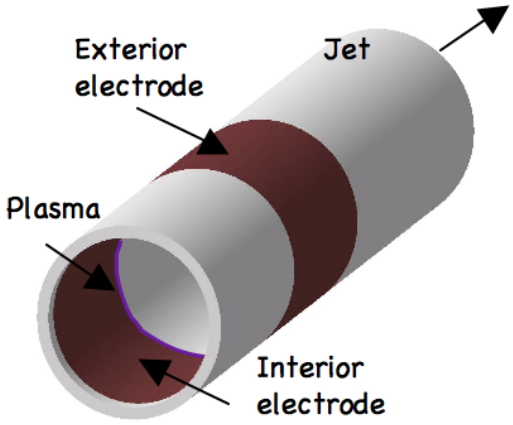

Figure 1.3: Plasma thruster.

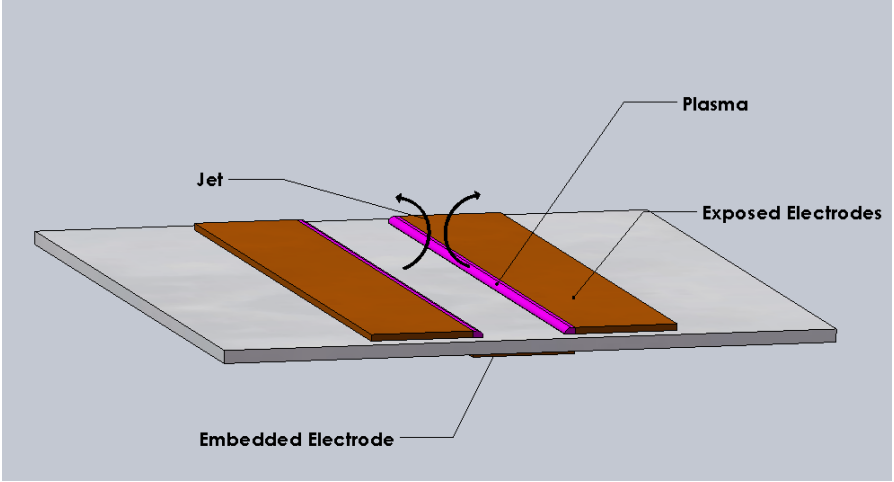

Figure 1.4: Jet vectoring plasma actuator.

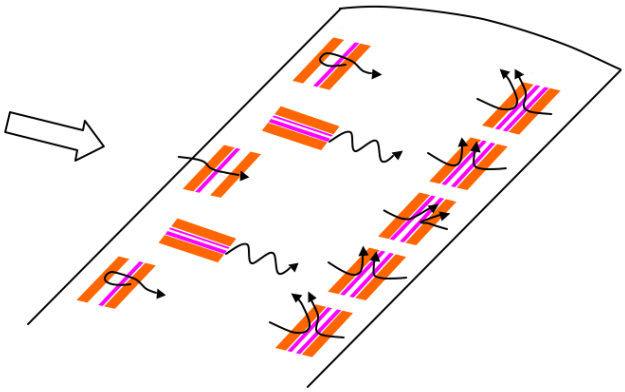

Figure 1.5: Co-flow, counter-flow and jet vectoring actuator configurations.

CHAPTER 2

Previous Work

Studies on flow control devices have primarily been focused on adding momentum to the boundary layer or using trips to initiate transition with leading edge devices. Thus in general, manipulation of the boundary layer has been the main objective for control. In order to achieve this, certain devices such as vortex generator jets (VGJs) or zero-net mass flux synthetic jets and plasma actuators in various configurations have been used. There are many parameters affecting the performance of plasma actuators, thus characteristics of these have been investigated in detail to get better results, while different configurations such as the plasma synthetic jet actuators and the thrust vectoring plasma actuators have been considered. Only a small fraction of the vast amount of flow control device research is discussed here.

2.1 Flow Control

The most common difference between active and passive flow control is based upon energy addition to the system. Synthetic jets and plasma actuators, for example, are considered to be active flow control devices since they are connected to external power sources. Vortex generators, on the other hand, do not rely on external power to operate, thus they are classified as passive control devices. Previous work on flow control investigates both types to alter the boundary layer and suppress separation.

For active control, the terms open and closed-loop arise where the latter is one that has a feedback mechanism. This means that the control device sends a command to the system according to some measurement from the system itself. An open-loop

system, however, includes a control mechanism which does not have an effect on the sensor that delivers this measurement, thus including systems with no sensors at all or ones with a feed-forward mechanism. These flow control techniques are summarized in Fig. 2.1, wherein the plasma actuators in consideration fall into active control with an open-loop system.

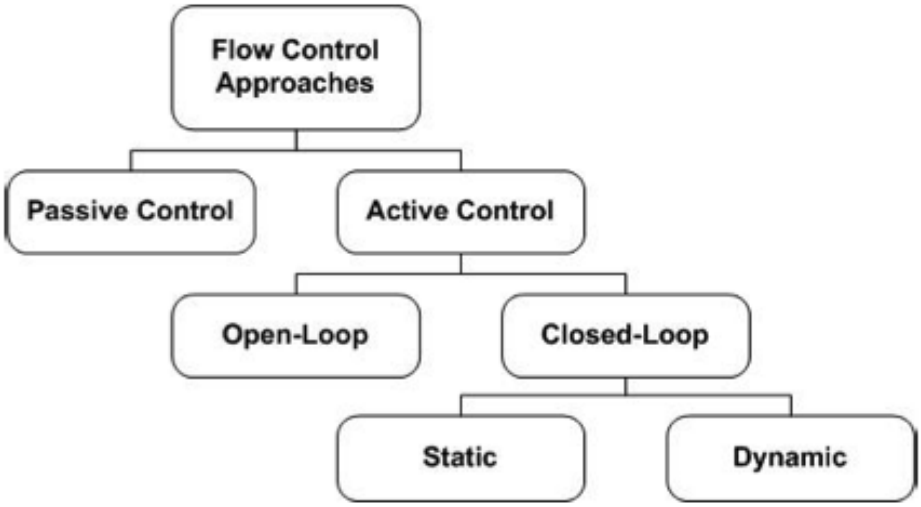

Figure 2.1: Classification of flow control techniques.

2.1.1 Vortex Generator Jets and Other Mass Flux Devices

Various methods of flow control have been studied by researchers over the years, including vortex generator jets, synthetic jets and other zero-net mass flux devices such as plasma actuators. Vortex generation is commonly used in the boundary layer to reattach flow and eliminate separation. Pulsed and steady vortex generator jets on a low pressure turbine blade cascade model were investigated by Mcquilling *et al.* [10] They conducted tests at Re=30,000 to Re=300,000 and PIV measurements indicated that for the uncontrolled case, separation occurred between 63.4% and 67.6% of the suction side length regardless of the Re, turning angle and the free stream turbulence intensity. The use of steady and pulsed VGJs at 46% of the suction side length with a 50% duty cycle however, suppressed separation for almost every case.

McQuilling and Jacob further studied pulsed vortex generator jets for separation control purposes. [11] They placed this geometry on two low pressure turbine blades at different locations of the suction surface length, one close to the leading edge at 10.5% and the other near the trailing edge at 69%. Both steady and pulsed jets with varying duty cycles were investigated and the results indicate that for the 69% location, the VGJs had the most significant effect in eliminating separation. Steady operation controlled separation at all times while the 50% and 10% duty cycles were also very effective. The 10.5% location near the leading edge, however, only eliminated separation at steady cases and was found to be ineffective for either duty cycles for pulsed blowing. It was also seen that the vortical interaction and diameter of the vortices at the 69% location were larger than the ones at 10.5% location.

Bons *et al.* studied VGJs placed on low pressure turbine blades for Re=20,000 to Re=50,000 for both steady and unsteady actuation. [12] It was seen that these cases triggered early transition and the flow reattached at the aft part of the suction side of the blade. Pulsed blowing was found to require one order of magnitude less mass flow than the steady VGJs. They also stressed out the importance of locating these VGJs closer to the separation point.

Two methods of separation control using pulsed vortex generator jets (PVGJs) were studied by Gross and Fasel on low pressure turbine blades at low Re. [13] These jets were found to transition the flow earlier and allowed increased turbulent momentum exchange which helps the boundary layer with the adverse pressure gradient, thereby providing separation control. They also employed harmonic blowing which proved to be more effective than the PVGJs with larger wall normal momentum exchange.

Recent studies on flow control using vortex generator jets were made by Krzysiak. [14] A proposed self-supplying vortex generator which uses the air from the high pressure region near the leading edge of the lower surface of the airfoil as well as a

conventional jet were employed on a NACA 0012 airfoil. Wind tunnel experiments at both low and high speeds of M=0.05-0.1 to M=0.1-0.85 were conducted for 0.5 m and 0.18 m chord lengths, respectively. It was seen that even though the self-supplying vortex generators were not as effective as the conventional ones, a reasonable amount of increase in the lift coefficient and critical angle of attack were observed. It was also noted that the highest effectiveness was achieved at about 60 deg jet skew angle and 30 deg of pitch angle.

2.1.2 Synthetic Jets

Extensive research has been conducted on synthetic jets for use as flow control devices (e.g. Glezer *et al.* [15]) Synthetic jets are zero-net momentum flux jets like the plasma driven micro thrusters in discussion that successively suck in and blow air out from a cavity in which an oscillating diaphragm is mounted, shown in Fig. 2.2. Although synthetic jets are like pulsed jets in terms of the fact that they are both produced by the advection and interaction of discrete vortical structures, they differ from them, being formed from the working fluid and transferring linear momentum without net mass injection across the flow boundary. The interaction between a synthetic jet and a cross flow was observed and flow control was achieved on scales that are one to two orders of magnitude larger than the characteristic length scale of the jet itself. Use of high actuation frequencies result in the decoupling of the aerodynamic forces from the frequency of the actuators.

Smith and Glezer investigated the interaction between a primary conventional rectangular air jet and a high-aspect-ratio co-flowing synthetic jet using PIV measurements. [16] It was seen that an entrainment region occurs, causing a low pressure region near the flow boundary and allowing the primary jet to deflect towards the synthetic jet. The volume flow rate of the conventional jet imparted into the synthetic jet and hence the vectoring force is dependent upon the driving frequency and the

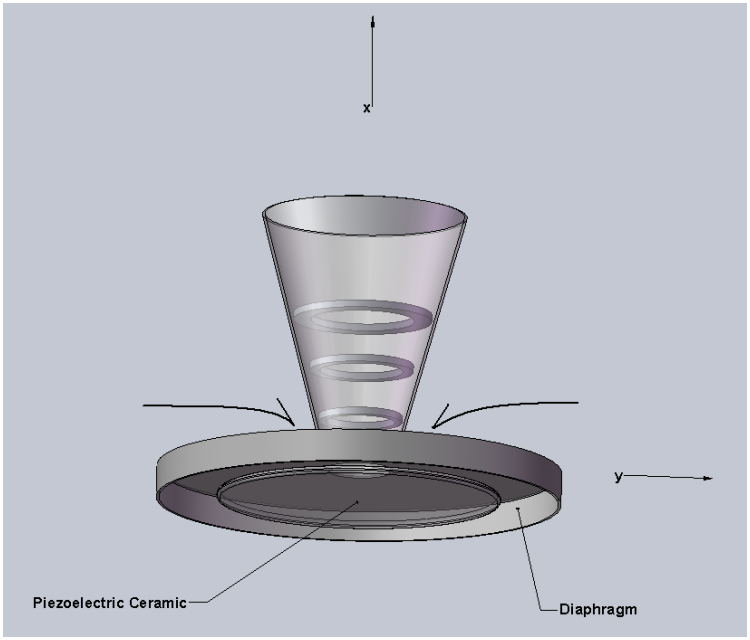

Figure 2.2: Synthetic Jet.

amount of entrainment for a given synthetic jet strength, duty cycle and primary jet speed. Both the vectoring time and angle increase monotonically as the primary jet speed is decreased while the vectoring angle oscillates at the actuation frequency for stepped modulation. The velocity within the orifice is also increased with stepped modulation of the driving frequency A stagnation point in the interaction region between the jets was observed during the suction stroke and the stagnation streamlines divided the flow into four quadrants, including of the previously mentioned low pressure region. This region becomes time-independent when the actuation frequency is relatively higher than the characteristic jet interaction relaxation time.

The control of separation on a half-cylindrical hump using a synthetic jet has been studied by Suzuki. [17] Direct numerical simulation (DNS) was performed for compressible, unsteady and laminar flow over the hump and the vorticity flux balance at the wall and its centroid were considered. It was found that the periodic actuation reduces the rate of vorticity production, breaking large-scale vortices into smaller ones and also moves the centroid upstream, delaying separation. Thus, performance

in terms of lift and drag coefficients, which can be expressed as functions of the vorticity production rate and centroid position, is greatly enhanced. Individually, the lift depends on the horizontal position of the vorticity centroid while the drag is dependent on both the vertical position and the rate of production of vorticity. The forcing frequency controls the detachment point of the separation vortex, which is determined by the centroids of vortices produced, found to be $F^+ = f_{act}D/u_\infty \approx 1$ for minimum drag where f_{act} is the forcing frequency of the actuator, D is the chord length and u_∞ is the freestream velocity. It was also concluded that the lift decreases monotonically with the frequency. The other parameter affecting vorticity centroid was found to be the actuator position at which the clockwise vorticity is created.

Another study on separation control has been conducted by Dandois *et al.* wherein they used synthetic jet actuators over a separated smooth ramp to observe the jet frequency effects on the flow and separation length. [18] Numerical simulation was employed for two different reduced frequencies of F^+=0.5 and F^+=4 corresponding to a vorticity-dominated mode and acoustic-dominated mode, respectively. The lower frequency was closer to the natural shedding frequency and the separation length was reduced by 54% while the high frequency increased the separation length by 43%. This was thought to be a result of the increase in the turbulent kinetic energy for the lower frequency case and the significant effect on the mean velocity profile.

Kotapati *et al.* observed synthetic jets in a quiescent environment and the evolution into a turbulent jet using direct numerical simulations and experiments. [19] The simulations used a different configuration with a simpler cavity, slot geometry and diaphragm placement but the agreement between the numerical and experimental results was significant. This was related to the use of the same Re, St and Stokes numbers and the fact that they determine the dominant characteristics of the jet flow. The internal flow was also investigated and they found pairs of spanwise vortices near the jet exit plane that break down due to the instability growth leading to transition.

Secondary vortex pairs around the primary pair cores that lead to the rapid evolution into the turbulent jet were observed thus a well-developed jet could be seen at a close downstream distance from the orifice as well as a region inside the cavity, the latter resulting from the primary vortex pairs.

2.1.3 Plasma Actuators

Most research conducted on plasma actuators has been limited to certain flow control applications such as separation on boundary layers of wings and other surfaces of importance by the addition of momentum. These actuators, whether single or multi phased arrays, affect the boundary layer flow on a very small scale of O(1 mm). In earlier studies, the ionic wind produced by a DC corona discharge was investigated by Malik *et al.* for boundary layer flow control over a flat plate. [20] It was seen that a 20% drag reduction was obtained at lower speeds up to 30 m/s.

Corke *et al.* stated that higher actuation amplitude levels were achieved when they spatially translated the plasma with high voltage phased inputs and varying forcing frequencies using glow discharges. [21] These glow discharge plasma actuators are scalable in size, accommodating a broad range of flows. They used this concept on an axisymmetric jet to understand the dynamics that affect the development of unsteady jets while observing that higher induced velocities compared to a steady, single phased plasma were obtained.

Jacob *et al.* investigated linear plasma actuators for boundary layer flow control purposes and placed them on a low pressure turbine blade at low Re to suppress separation. [22] Results indicate that the output from the plasma was maximized when the horizontal distance between the embedded and exposed electrodes was zero. Separation control was further studied by Jacob wherein the effects of an AC discharge plasma actuator on a boundary layer flow were observed by varying certain input parameters such as tunnel speed, driving frequency and power. [5] Flow visualization

and PIV results indicated an acceleration in the region close to the actuator while a turbulent jet was produced downstream. Upstream of the actuator, the presence of a sink-like region was noted, causing increased mass flow. Higher velocity and Reynolds stresses were also seen in the near wall viscous regions. As a result, the momentum was increased, causing a thinner boundary layer downstream of the actuator. Then, the actuator was used on an LPT blade at low Re and separation was eliminated for all cases investigated.

Similarly, Jacob and Ramakumar used AC discharge plasma actuators in quiescent flow, a flat plate boundary layer and an LPT blade for separation control. [6] As was seen before, the velocity downstream of the actuator is increased and fluctuations can be observed while the displacement and momentum thicknesses are reduced. The effect of increasing freestream velocity is significant; the effectiveness of the actuators decrease and the increase in velocities are considerably smaller, also noted by Baughn *et al.*. Velocity profiles upstream and downstream of a plasma actuator were investigated and the results indicate that low freestream velocities do not affect the force produced by the actuator. [23] However, Jacob and Ramakumar found that the velocity fluctuations were still significant, thereby allowing flow control with low power even at relatively higher speeds. The actuators suppressed separation in the turbine blades and cross-stream vortical structures were observed.

Detaching effects of the plasma actuator on airflow were investigated wherein an actuator on an inclined wall was tested; making certain wind tunnel and PIV measurements. [24] It was observed that pressure decreased downstream of the discharge and a velocity decrease was induced, allowing detachment in the flow along the wall. The effect of the actuator on the induced flow and its direction was found to be tailored by the electrode arrangement, important for thrust vectoring applications.

Corke and Post investigated several flow control applications using single plasma actuators. [25] For the separation control on the leading edge of a wing section, it was

seen that a 400% increase in the lift-to-drag ratio was obtained for angles of attack beyond stall. The actuators were also used near the leading edge of an oscillating airfoil and the results indicated that the cycle-integrated lift was improved by 13%. Actuators on the mid-chord region of blades in a linear cascade were observed, simulating the effect on the blades of an LPT stage of a gas-turbine engine. They found that the use of plasma actuators completely prevented the separation occurring in this region. In all cases observed, operation with a short duty cycle rather than steady actuation showed to be more effective. Models of the plasma generation and the body force induced on the flow were implemented into numerical flow solvers and it was seen that the results for separation control agreed with the experiments conducted.

Similar to the previous study, plasma actuators were used for certain flow control applications such as separation control over the leading edge of an airfoil. [26] Both steady and unsteady actuation was used and it was seen that unsteady actuation was more effective than the steady case. Dynamic stall vortex control over the leading edge of an oscillating NACA 0015 airfoil was studied with a single plasma actuator. Compared to the case with the actuators off, it was seen that an increase in lift of about 13% was obtained with the closed-loop smart control which operates the actuator at certain parts of the cycle. The second best improvement was observed for the unsteady case of 20 Hz pulsing frequency. Other applications include separation control for the blades of an LPT stage and control of blade tip clearance.

Corke *et al.*used single DBD plasma actuators to improve lift without having to use moving flaps, which also decreases the form drag associated with the hinge gaps. [27] A laminar airfoil with a separation ramp on the trailing edge was employed with the unsteady operation of the plasma actuator. This allowed for a 90% decrease in the power input as well as an increase in the actuator durability. An HSNLF(1)-0213 airfoil was placed on a lift-drag force balance for the experiments and a numerical model using the along with results was also presented. It was concluded that the

improvement in lift was similar to that when the flaps were used while an optimum value to scaling parameters such as the forcing frequency and the effects of Re numbers were shown. A non-dimensional frequency is defined by $F^+ = \frac{fL_{sep}}{U_\infty}$ where L_{sep} is the streamwise extent of the separation region and a value of $F^+ = 1$ yielded the highest increase in lift caused by two spanwise vortices with a wavelength of $0.5L_{sep}$.

Experiments were conducted on a swept wing, scaled UAV model to achieve flight control at low angles of attack with a plasma actuator placed on a windward surface behind a separation ramp near the trailing edge. [28] It was concluded that the ramp angle, duty cycle and the modulation frequency had a very important effect on the performance of the actuator; steady actuation had a negligible effect on the flow field whereas pulsing shifted the lift coefficient significantly. Considerable amounts of decrease in the lift coefficient were observed (15% to 25%) for 20 & 30 degree ramps with 12.5% duty cycle yielding the best results for the 20 degree ramp while a 25% duty cycle was found to be the most effective in decreasing the lift curve. As the ramp angle is increased, the adverse pressure gradient increased significantly and the actuators were ineffective in controlling separation.

Most of the research on eliminating separation consists of using the plasma actuators to add momentum to the boundary layer. However, since the amount of momentum added to the boundary layer by leading edge actuators is limited and restricted to the boundary layer, Porter *et al.* investigated the use of plasma actuators as boundary layer trips to control separation. [29] This way, instead of delaying transition by adding momentum, momentum was removed and they were able to trip the boundary layer at a 10% duty cycle.

Some earlier work was also done by Hultgren *et al.* [2] They investigated the control of boundary layer separation on a flat plate using glow-discharge plasma actuators with flow conditions similar to that of a low pressure turbine airfoil. The Re number was varied from cruise values around 50,000 to the takeoff values of about

300,000 with freestream intensities ranging from 0.2% to 2.5%. A phased-plasma-array actuator was placed streamwise on the flat plate upstream of the separation point. Measurements of static pressure and hot wire anemometry indicated that the actuators caused earlier transition in the layer above the separation bubble, thus reattaching the flow. For low freestream turbulence values, the actuators were found to be much more effective because of the laminar boundary layer at separation although they were also useful for the higher intensity values.

Recent studies on plasma actuators were focused on controlling the free shear layer mixing at the exit of a nozzle caused by an axisymmetric turbulent jet. Benard *et al.* used two linear plasma actuators on the lips of a 22-degree-angle diffuser in order to either reattach the flow to the 30-mm-long bevel or to excite the flow where instabilities occur. [30] Stereoscopic PIV and laser Doppler velocimetry were employed for speeds ranging from 10 m/s to 40 m/s and it was seen that full or partial reattachment was attained for the given speeds, respectively. It was also observed that the vortex shedding frequency was the same as that of the forcing frequency applied to the actuators. They concluded that quasi-steady actuation provided a significant amount of increase in jet spreading and turbulent kinetic energy along with a decrease in the jet core length. Unsteady actuation showed that St numbers ranging from 0.25 to 0.32 was effective in increasing the flow turbulent kinetic energy.

2.2 General Plasma Actuator Characteristics

There have been numerous amounts of research on plasma actuators these past recent years. Work done by Enloe *et al.* has resulted in several interesting and important conclusions on the characteristics of plasma actuators. [31, 32] They observed that the actuators are a form of dielectric barrier discharge and since its gross structure has an effect on the momentum coupling, the bulk heating was not considered to be an aspect that affects the flow. It was stated that the electrostatic body force and the

following momentum transfer to the surrounding fluid is a result of the interaction of the plasma with the electric field in the discharge. This electrostatic force per unit volume induced by the plasma is proportional to the net charge density and the strength of the electric field, given by $f = \rho E = -\frac{\epsilon_0}{\lambda_D^2}\phi E$ where ϵ_0 is the permittivity of free space, λ_D is Debye length which is the characteristic length for electrostatic shielding in a plasma, ϕ is the local electric potential and E is the electric field. The force density was determined the largest in the region around the edge of the exposed electrode. Based on voltage and plasma emission measurements, numerical simulations and large scale integral measurements of thrust output, the authors also concluded that the power input to the plasma is nonlinear with the voltage drop across the dielectric while both the maximum induced velocity and thrust are proportional to input power. The power and thrust are directly proportional whereas power was found to be proportional to $V^{7/2}$.

The effect of atmospheric pressure on the electromechanical properties of DBD plasma actuators were investigated by Benard and Balcon. [33] They studied the jet created by a linear actuator in a vacuum chamber under different pressure values. It was seen that the extent of the plasma was improved significantly at low pressures around 0.2 atm and high velocities with thicker velocity profiles were obtained despite the drop in the mass flow rate. Two different electrode configurations with different length grounded electrodes were used and they observed that a longer embedded electrode length allows the maximum velocity to be maintained on a 15 mm wide distance.

Benard *et al.* also investigated the effect of relative humidity (RH) on a simple dielectric barrier discharge plasma actuator, where they used values ranging between 40% to 85% and observed the time-averaged and time resolved measurements of the induced electric wind. [34] Upon analyzing the plasma discharge produced, it was found that both negative and positive current peaks decrease, although after

85%, the number of positive peaks increased due to condensation over the dielectric material. Even though the effectiveness of the momentum transfer decreases as the humidity is increased along with the resulting velocities, the actuators are still capable of transferring momentum and thus are able to operate at high humidities.

Recent work has been done by Enloe *et al.*, stating that the plasma exists as a series of microdischarges with three stages to the process; ignition, expansion and quenching. [35] Microcharges deposit charge on the surface of the dielectric during expansion which starts decreasing the electric field. The plasma is self-limiting in that there comes a point where the applied negative or positive voltage cannot maintain the discharge anymore. These stages exist both in the forward stroke (negative-going half cycle) and the backward stroke (positive-going half cycle). The exposed electrode is driven to increasingly negative voltage and the electrons are emitted from the electrode to the dielectric surface in the forwards stroke while the opposite happens for the backward stroke. Enloe *et al.*found that the drag associated with the very high velocities near the surface in between plasma discharges is mostly made up for by the force produced in the negative-going half cycle. [36]

Research on plasma has not only been limited to dielectric barrier discharge actuators. Glow discharges were also used in addition to the arc discharges and DC corona discharges mentioned previously. Roth *et al.* used One Atmosphere Uniform Glow Discharge Plasma (OAUGDP) actuators on planar panels for laminar, transitional and fully turbulent flow in the frequency range of 2 kHz to 10 kHz. [37] As a result of formation of vortical structures due to paraelectric electrohydrodynamic forces on the fluid, they found that asymmetric streamwise or spanwise configurations of plasma generating electrode arrays produced significant thrust, whereas the symmetric actuator configurations caused a large increase in drag. Roth *et al.* also studied certain physical properties of OAUGDP plasma actuators, particularly the relationship between the power input and output. [38] It was found that the power

supplied to the actuator was divided between the heating of the dielectric material and the power needed for plasma generation. The results showed that the fraction of total power loss to dielectric heating was 48% to 100% in single actuators.

Roth and Dai studied the physics of OAUGDP plasma actuators and their optimization as electrical devices. [39] Certain input signal, dielectric material and geometry parameters were varied to observe their effects on the induced flow. It was seen that the type of dielectric material was important since it was effective on the main source of power loss from the dielectric heating. The plasma volume and the distribution of electric field lines were also found to be affected from the dielectric material, thus it was concluded that a material with a higher dielectric constant, strength and lower heating loss factor should be used. They found that using teflon rather than quartz resulted in a stronger induced jet. In terms of geometry, the parameters varied were the horizontal distance between the electrodes and the width of the embedded electrode, the latter having an insignificant effect on the induced velocity or power requirements. The separation distance between the embedded and exposed electrodes however, had a drastic effect on these parameters. Out of a small gap, a zero gap and a slight overlap, the small gap of 1 to 2 mm yielded the highest velocities. Input signal parameters were also varied and it was observed that for a constant forcing frequency, an increase in the voltage resulted in a higher velocity. Keeping the applied voltage constant and varying the frequency, however, resulted in the increase of induced velocity up to a certain maximum after which it decreased with further increases in the frequency and polarization of the plasma.

AC and pulsed DC glow discharges were studied by Rivir *et al.* [40] They used electrode lengths of 26 cm, 56 cm and 78 cm from 3 kHz to 10 kHz for AC glow discharges, whereas for the pulsed DC discharges, 100 Hz of pulsing rate was employed for the same length electrodes with pulse widths ranging from 22 nanoseconds to 2 microseconds. Single electrodes of lengths of 15-20 cm were also used to observe

their effect in 2D boundary layers. It was seen that PIV measurements at freestream velocities of 1.5 m/s resulted in a 250% increase in near wall velocity.

2.2.1 Force Measurements

The plasma induced force is significantly important in terms of the fact that it determines the effectiveness of the actuator, especially in the current study where the actuator is employed as a thruster. Porter *et al.* investigated the effects of pulsing at different frequencies (5-20 kHz) and voltages (7.5-10 kV) by measuring the time averaged body force using a pendulum arrangement while the time dependent (temporal) forces were measured with an accelerometer. [41] They found that for constant voltage, the time averaged body force and power dissipation were proportional with the frequency while the efficiency defined by force/power for the actuator as well as the impulse and energy dissipation during one cycle were independent of frequency; they remained constant. For fixed frequency, it was observed that the body force was also proportional to the applied voltage. The temporal force analysis from the accelerometer revealed that the actuator produces one large force and a smaller force in the opposite direction during each cycle.

The force created by a linear plasma actuator was directly measured by Enloe *et al.* [42] The operation of the actuator at low duty cycles revealed the working mechanism along with the relationship between the plasma and the overall inertia of the neutral fluid. It was seen that this momentum coupling occurred in timescales much less than the motion of the bulk fluid. Thus, they concluded that the actuator could be considered as a heat and momentum source limited to a small control volume or a boundary. Plasma parameters such as the forcing frequency and waveform were found to be significant in determining the amount of momentum coupling to the fluid.

A study by Abe *et al.* observes significant effects of voltage waveform, different ambient gas pressure and species, electrode configurations and dielectric plate mate-

rial on the momentum transferred to the flow. [43] It was seen that the momentum transfer to the flow first increased before decreasing with the pressure of the ambient gas, unlike the results Gregory *et al.* obtained. [44] For varying pressure, they found that the efficiency of the actuator decreased linearly as the pressure was decreased. The chemical nature was also effective; different amounts of momentum transfer were observed for different types of gas species. They also discovered that the steeper the increasing part of the wave, comparing a square and sine wave in example, the larger the net momentum transfer was. Both the negative and positive parts of the wave were found to be effective in determining the momentum transfer performance. Finally, it was shown that the electrode configuration and dielectric plate also affected the flow, the latter having an effect depending on the ambient gas pressure. Similarly, all of the other parameters were found to be less significant on the momentum transfer when the gas pressure was decreased.

Likhanskii *et al.* presented a detailed physical and numerical model for an asymmetric DBD plasma actuator driven by nanosecond voltage pulses combined with positive dc bias. [45] Then, the effects of these series of high voltage negative and positive nanosecond pulses were compared to low voltage pulses. Although they experienced a reverse breakdown at negative pulses, the use of high voltages and nanosecond pulses resulted in stronger induced forces and more integral momentum was transferred to the gas. It was also seen that positive nanosecond pulses with a positive dc bias was very effective at high voltages and had a similar performance to that of negative pulses with positive dc bias at relatively lower voltages.

Opaits *et al.* observed the effect of the dielectric material on the surface charge in a plasma actuator driven by ionization pulses with a positive dc bias. [46] They found that a slightly conductive dielectric actually decreases the surface charge between pulses, in turn increasing the force produced. Out of two materials used, it was seen that zinc oxide was too convective while linen based phenolic was resistive.

The effect of actuator and embedded electrode size on the induced force was studied by Hoskinson *et al.* with 2-D simulations using single- and double-barrier plasma actuators. [47] For the full scale actuators, they found that more negative ions were produced and these played a very significant role in the simulations than the reduced scale. It was also observed that the single-barrier actuators resulted in smaller forces than the double-barrier actuators because of larger periods of inactivity. Larger electrode diameters decrease the induced body force but the dependence decreases for the full scales. These simulations were then verified with experiments using a probe for velocities and an electronic balance to directly measure the forces. [48] Again, it was seen that decreasing the diameter of the narrow electrode increased the force produced, more notably in the double-barrier plasma actuators. It was also observed that the material of the electrodes did not affect the force or force efficiencies.

2.3 Plasma Synthetic Jet Actuators (PSJAs)

The plasma synthetic jet actuator (PSJA) configuration studied by Santhanakrishnan and Jacob and shown in Fig. 2.3 consists of an exposed annular electrode and a circular embedded electrode. [49] These differ from the rest of the research conducted on plasma flow control in that the actuator is not used inside the boundary layer but rather outside it. Results indicate that the induced normal jet is very similar to that of the synthetic jet and a maximum velocity of 1 m/s can be obtained. It was also observed that the actuator decreased in effectiveness as the Re number was increased.

Continued studies on plasma synthetic actuators, which are zero net mass flux devices consisting of annular electrode arrays, have been made for use on flow control and thrust generation. [8, 9] It was found that unlike synthetic jets, this configuration can be reversed to be used for suction. The actuator was mounted on a plate and pulsed with modulation frequencies of 1 Hz, 10 Hz & 100 Hz. It was found that pulsed actuation creates a starting vortex ahead of the induced jet while a secondary

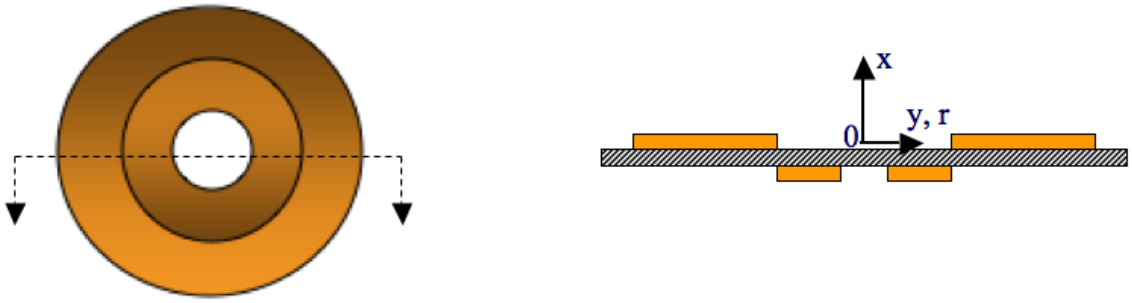

(a) Top view (b) Cross-section

Figure 2.3: Plasma synthetic jet actuator.

vortex ring is trapped, and a tertiary ring near the surface is observed as a result of entrainment in the boundary layer as seen in Fig. 2.4. This starting vortex was seen to be important in determining the maximum velocity and streamwise extent of the jet. When the forcing frequency was varied, it was observed that multiple vortex rings were formed and the interaction of the primary vortex rings resulted in an increase of the peak velocity, a value of $O(1$ m/s) at a frequency of 10 Hz found in previous research. The effect of a cross-flow was also investigated where the jet penetrates into the mean flow, thereby acting like a conventional jet with reduced effectiveness on the flow and boundary layer characteristics as the mean velocity is increased.

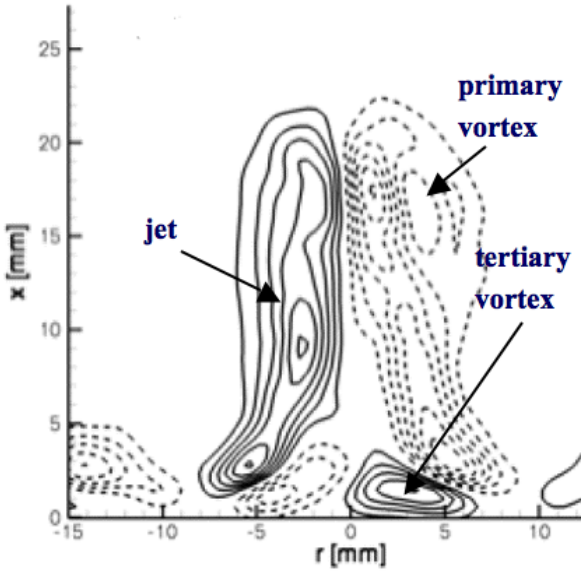

Figure 2.4: Flow structure of the PSJA during pulsed actuation.

Other studies on PSJAs have been made by Segawa *et al.* [50] They studied two different plasma actuator configurations and used Schlieren photography to observe the structure of the jets induced. It was seen that using an annular (PSJA) and linear PSJA configuration at temperatures of 20°C and 200°C resulted in mushroom cloud plumes.

2.3.1 Thrust Vectoring Plasma Actuators

A number of thrust vectoring applications using plasma actuators were investigated recently by Porter *et al.* [51], Benard *et al.* [52] and Bolitho and Jacob. [53] The variation of spanwise force in a plasma actuator was observed by Porter *et al.* [51] This was done by changing the shape of the embedded electrode so that the volume of the plasma created could be controlled, which in turn directly affects the body force produced. PIV measurements showed that steady jets with varying force along the actuator span could be generated by changing the width of the embedded electrode. Steady jet vectoring was also achieved wherein two linear actuators facing each other were used and their strengths were varied asymmetrically via changes in the applied voltage. Results showed that the jet can be controlled 180 degrees with small voltage variations.

A similar study was made by Benard *et al.* [52] They also used two opposite single DBD actuators to create two impacting wall jets that result in a wall normal jet of maximum velocity of 1.9 m/s. This configuration was then used to control separation at the leading edge of a NACA 0015 airfoil at a freestream of 15 m/s. Lift and drag force measurements showed that a significant increase in lift and a reduction in drag occurred when the jet was normal to the wall or at a pitch angle of +18 degrees.

Steady and unsteady vectoring of flow in a linear dielectric barrier discharge plasma synthetic jet actuator shown in Fig. 2.5 for a number of flow control applications were examined by Bolitho and Jacob. [53] It was shown that the direction

of the steady jet produced could be controlled by varying the strength of the continuous dielectric barrier discharge. Similar to the current study, unsteady jet vectoring was also investigated wherein the duty cycle and the plasma frequency of the actuators was varied asymmetrically. The results obtained showed that the latter was more effective. It was also seen that the pulsing frequency controlled the type of jet produced; near wall jets, standing vortices, or wall normal jets were obtained. Further discussion can be found in Bolitho. [54]

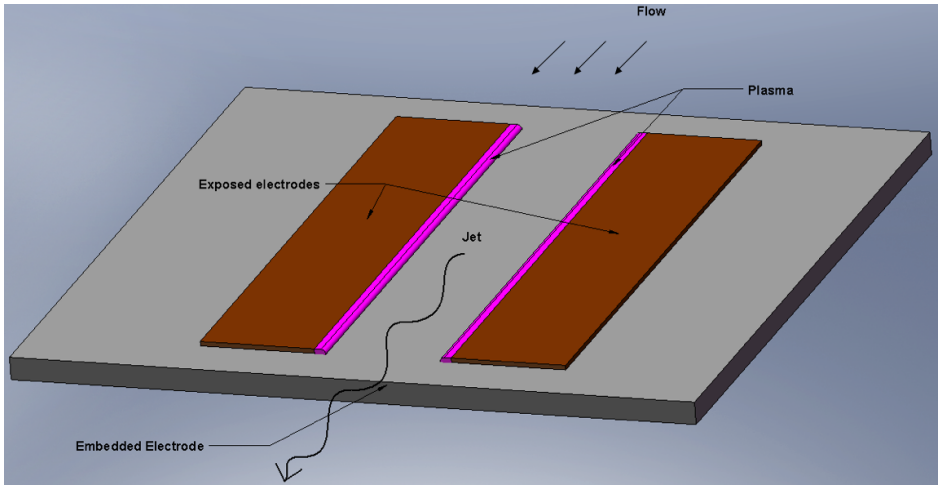

Figure 2.5: Linear plasma synthetic jet actuator.

CHAPTER 3

Experimental Arrangement

3.1 Plasma Actuator Configurations

Two actuator arrangements were investigated in the current study, a circumferential thruster configuration as well as a jet vectoring geometry. The plasma thruster is constructed of 5.08 cm long teflon tubes of various diameters and thicknesses with 1.27 cm thick copper tapes both in the exterior and interior of the tubes, separated by 1 mm, shown in Fig. 1.3. As with the linear plasma actuators, a zero-net mass flux jet is produced when a potential difference is applied across the exterior and interior electrodes. These exterior and interior electrodes can be thought of as the embedded and exposed electrodes in the linear case, thus the axial extent of the plasma is determined by this exterior electrode, about 1.47 cm in this case, which also drives the internal flow. The front and side views of this actuator configuration can be seen in Fig. 3.1 along with the plasma ring created on the interior during actuation, shown in Fig. 3.2.

The jet vectoring configuration, also referred to as the linear plasma synthetic jet actuator (linear PSJA), is much more similar to the linear case wherein a single embedded electrode is separated from two exposed electrodes on either side by the dielectric, shown in Fig. 3.3. For the experiments conducted with these vectoring actuators, Alumina ($\epsilon \sim 10$) and Teflon ($\epsilon \sim 2.1$) plates with respective thicknesses of 0.064 cm and 0.16 cm were used as the dielectric materials.

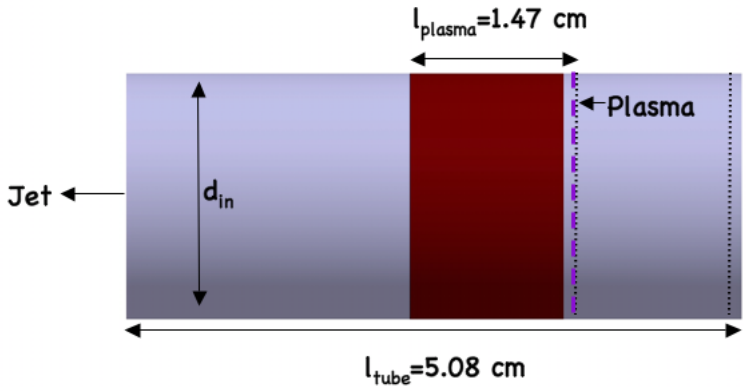

(a) Side view

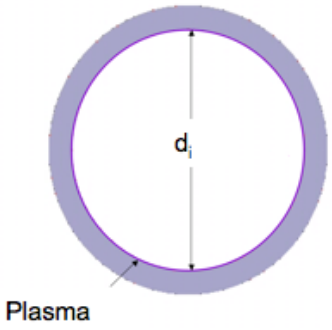

(b) Front view

Figure 3.1: Front & side views of the plasma thruster.

3.2 Input Signal & Power Calculations

For the benchtop experiments, a power supply with about 5-30 V input is connected to the actuator through a Minipuls2 Circuit Board by Electrofluid Systems. An input signal in the form of a square wave and frequency range of 5-9 kHz is generated by a program in Labview with a block diagram for two channels in Fig. 3.4. The signals are then provided to the actuator by a data acquisition unit. The schematic for this

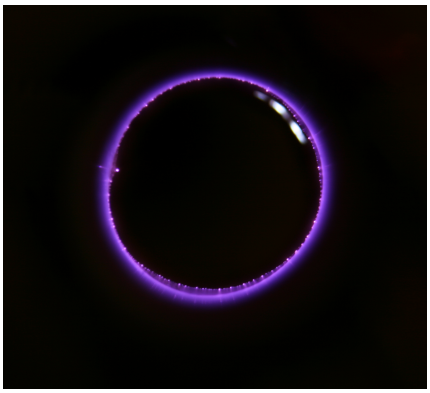

Figure 3.2: End view of the plasma on the interior duct wall.

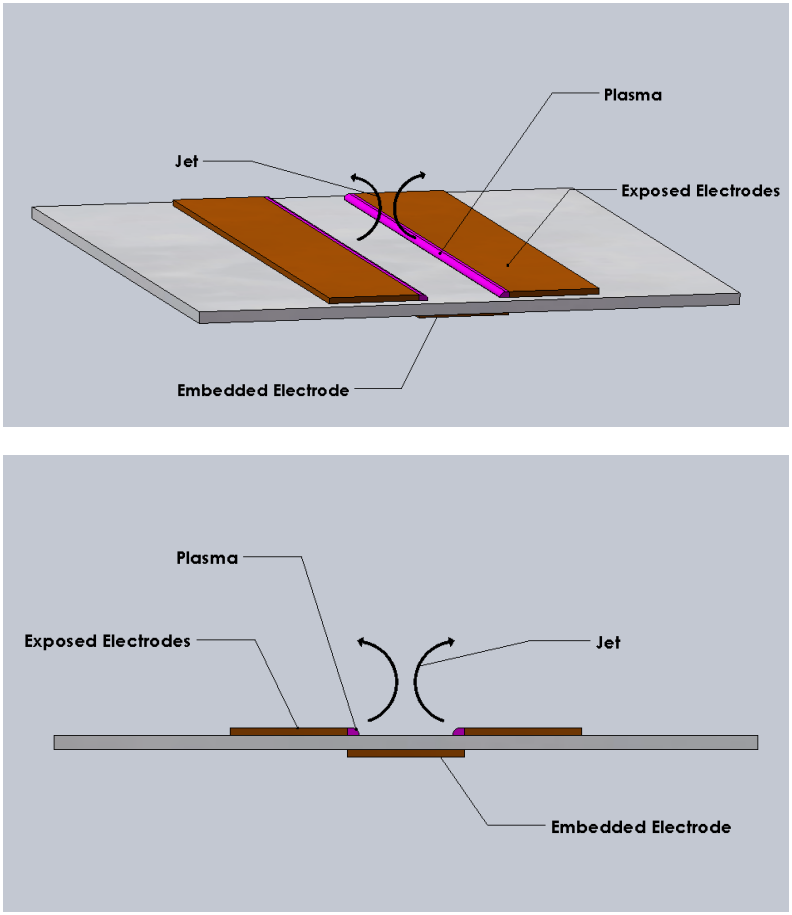

Figure 3.3: Jet vectoring plasma actuator.

arrangement can be seen in Fig. 3.5. Two CMI 5012 transformers and a QSC RMX 1450 amplifier with an amplification ratio of 1/60 were used instead whenever two channels needed to be used simultaneously, seen in Fig. 3.6. For all the wind tunnel

tests, the same setup with the CMI 5012 transformers were used. Detailed information about the input and output values of the transformers at the given operating frequencies can be seen in Table 3.1

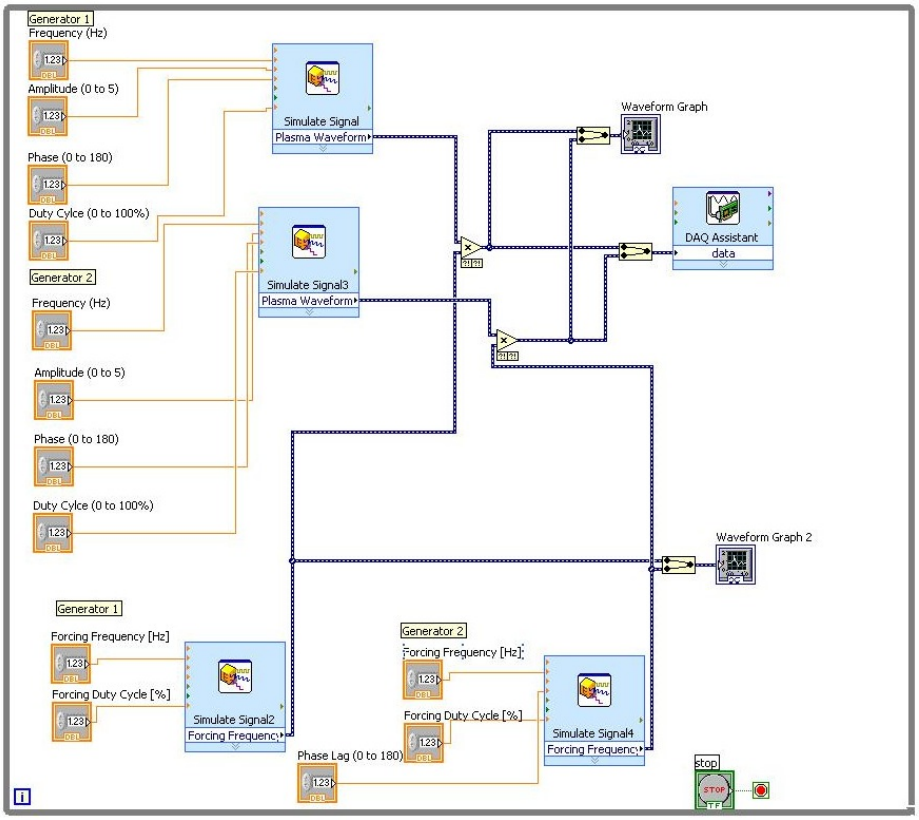

Figure 3.4: Block diagram in Labview for two channel control.

Table 3.1: Specifications of the Minipuls2 Circuit Board & CMI 5012 transformers.

	Minipuls2 Circuit Board	**CMI 5012**
Operating Frequency	8 kHz	6 kHz
Input Voltage	15-40 V	40 V
Output Voltage	<18 kV	5,5 kV

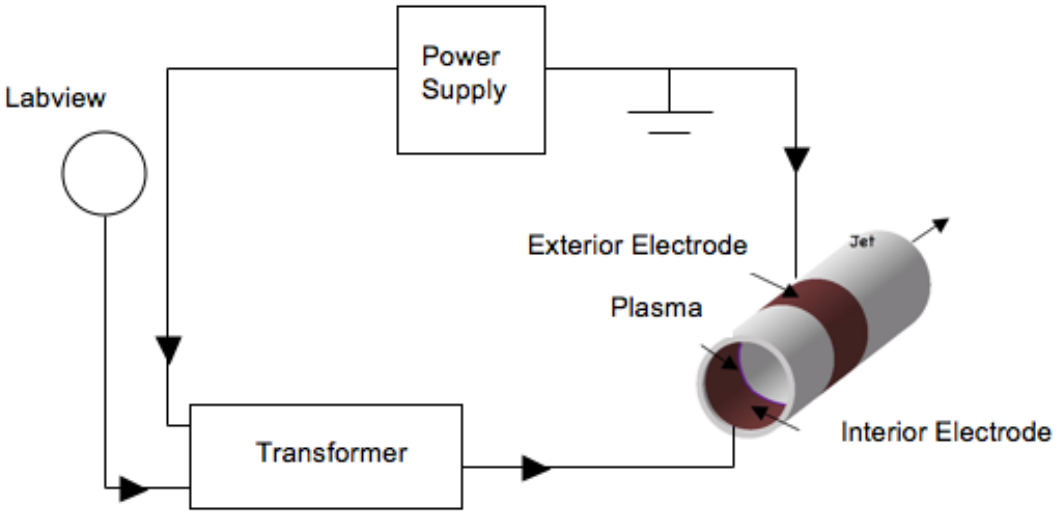

Figure 3.5: Schematic of experimental setup.

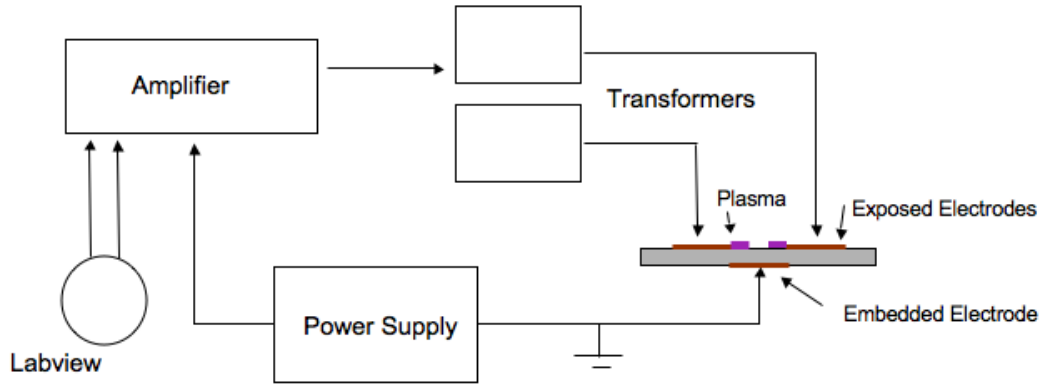

Figure 3.6: Schematic of alternative setup for the jet vectoring actuator.

Current and voltage measurements for several cases were made with a NK Technologies AC current transducer and a North Star PVM-11 1000:1 high voltage probe, respectively. An oscilloscope was employed to obtain these readings and plot them, later to be used in power calculations.

3.3 PIV Measurements

The induced velocity of the jet was measured with a PIV system with the schematic shown in Fig. 3.7. Components include a monochrome Kodak Megaplus ES 1.0 CCD camera with a resolution of 1008 x 1018 pixels and a double exposure capability to capture an image pair within a small period of time, a dual-head Nd:YAG laser from Big Sky Lasers with 45 mJ of output energy, wavelength of 532 nm, pulse width of 6 ns and beam diameter of 2.8 mm, a Quantum Composer timing box that controls and synchronizes the camera and laser heads, an oscilloscope to monitor timing of the laser pulses, a Turbofog fog generator to introduce particles into the flow field, optics for laser sheet generation, a computer with frame grabber hardware (PIXCI D) and software (XCAP) for image acquisition and finally, PIV processing software as discussed below.

To acquire PIV measurements, a transparent box for the benchtop tests or the wind tunnel itself containing the actuator is seeded with smoke particles on the order of 1 micron in diameter. A 2-D light sheet of about 2 mm thickness is projected in the vertical plane through the center of the circular tube using the Nd:YAG laser. The set of optics consists of three lenses that create the laser sheet. The laser first goes through a converging lens, is focused, then passes from a diverging lens placed at the focal length of the first lens and becomes more concentrated. Finally, the last circular lens diffuses the beam and the 2-D laser sheet is formed. The timing control unit is used to pulse the lasers in synchronization with the CCD camera. These individual components can be seen in Fig. 3.8. The vertical field of view is approximately 4 to 10 cm with a resolution ranging from 97 pixels/cm to 269 pixels/cm. Epix frame grabbing hardware and software is used to acquire binary image pairs. For each run, either 63 or 191 image pairs were captured at a rate of approximately 10 Hz with 50 microseconds of delay between the laser pulses and these images were processed using the algorithm given below. The velocity and vorticity fields obtained in post-

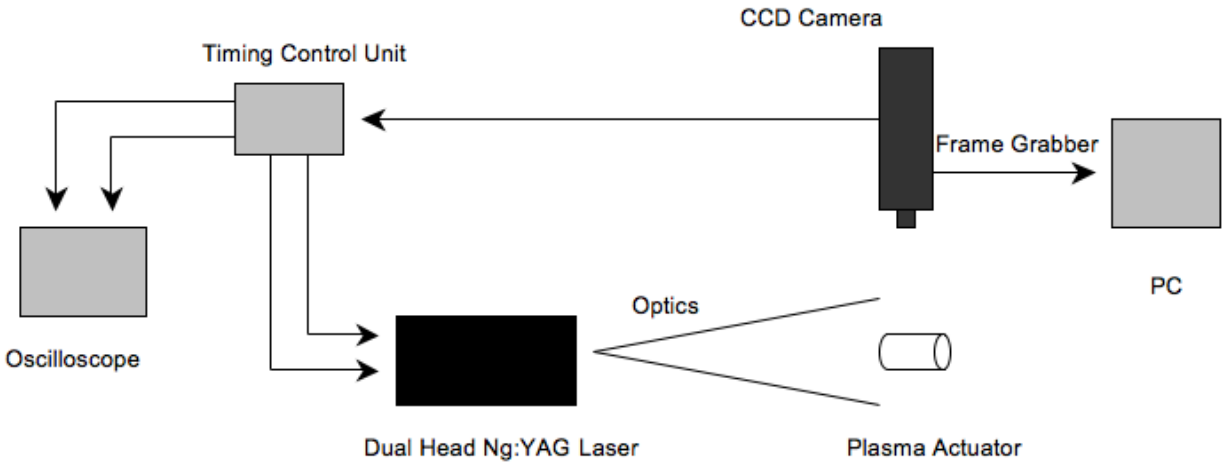

Figure 3.7: Schematic of PIV setup.

processing were then averaged over the data set.

The PIV algorithm utilizes the wall adaptive Lagrangian particle-tracking algorithm (WaLPT) developed by Sholl and Savaş. [55] This algorithm treats the seeding as fluid particles and determines their translations and deformations. Fluid parcels registered by CCD pixels are advected with individually estimated velocities and total accelerations. A standard DPIV algorithm is employed to determine the initial velocity field, and the routines in WaLPT allow for highly accurate measurement of the velocities near surfaces by mirroring the flow about the wall using an image parity exchange routine. [56] Velocity and vorticity are calculated as part of the PIV algorithm and scaled accordingly; vorticity is determined spectrally and does not suffer from typical numerical differentiation problems.

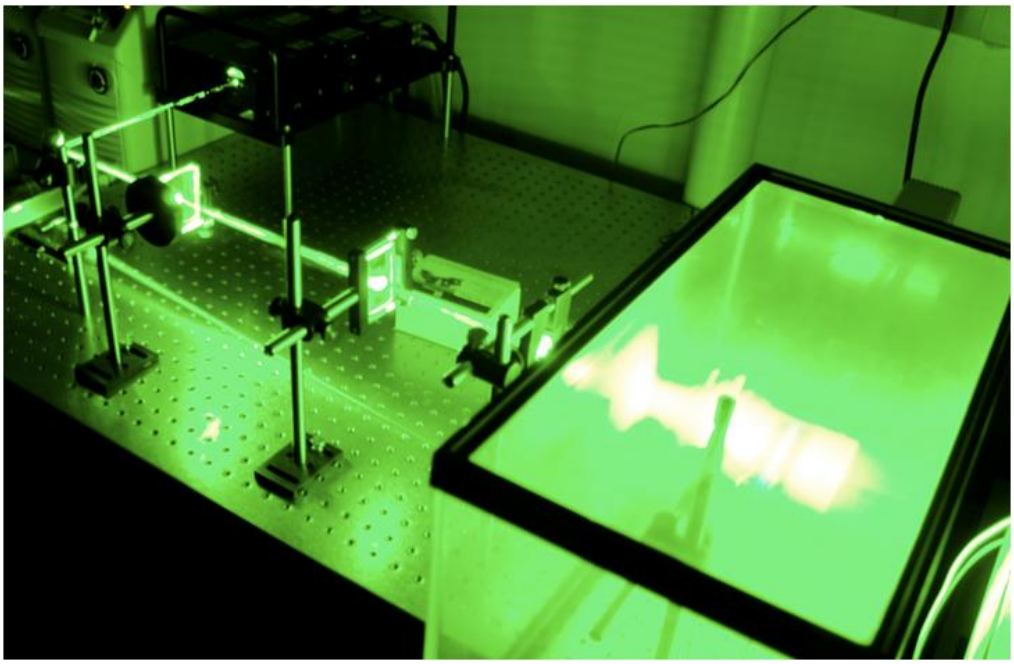

Figure 3.8: PIV setup.

3.4 Benchtop Setup

For the benchtop experiments conducted in quiescent flow, only the plasma thruster configuration was used wherein the actuator is mounted inside a 50.8 cm x 25.4 cm x 30.5 cm transparent container for seeding purposes, seen in Fig. 3.9. The CCD camera is placed such that it is perpendicular to the laser sheet which passes through the vertical centerline of the thruster tube. All these components can be seen in Fig. 3.10 of the setup. This allows for a cross section of the induced jet to be captured and later to be analyzed with the WaLPT algorithm mentioned previously. For all tests, the field of view was about 6 cm,the resolution was between 150 pix/cm and 175 pix/cm while 191 image pairs were captured and averaged over the single case observed. A raw PIV image can be seen in Fig. 3.11.

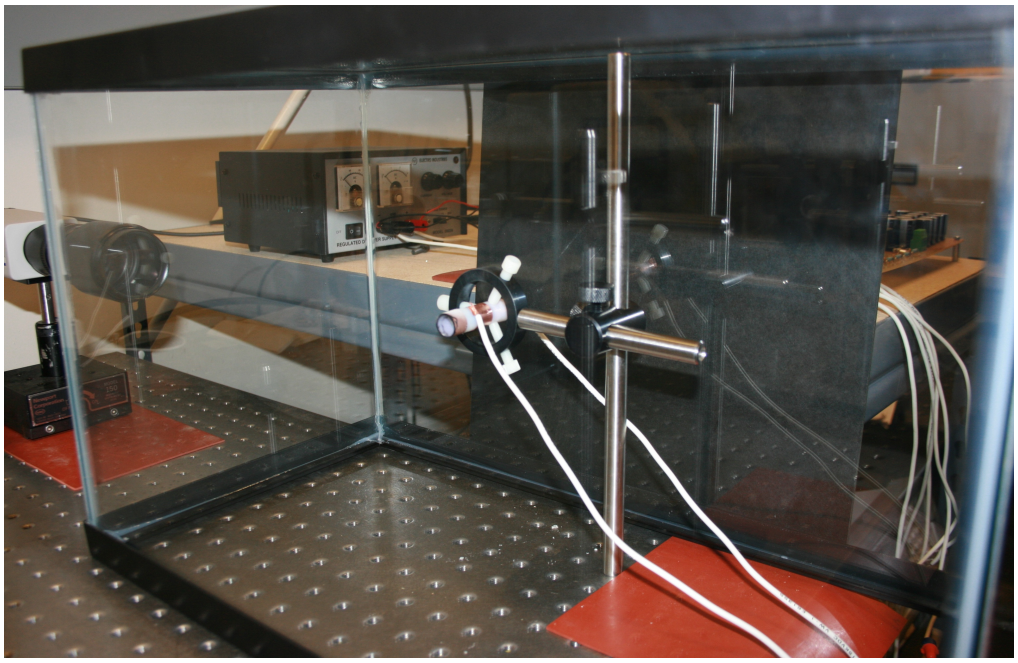

Figure 3.9: Plasma actuator mounted on benchtop inside transparent container.

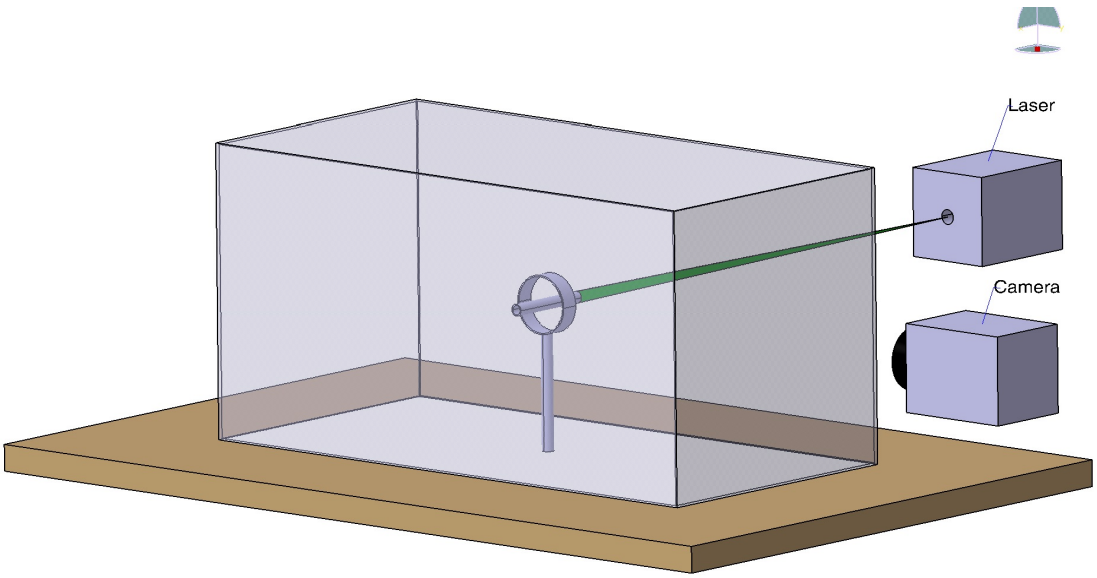

Figure 3.10: Benchtop setup.

3.5 Wind Tunnel Setup

The effect of freestream was observed on both configurations where the thrusters were first placed inside the 30.5 cm x 30.5 cm test section and just as in the benchtop

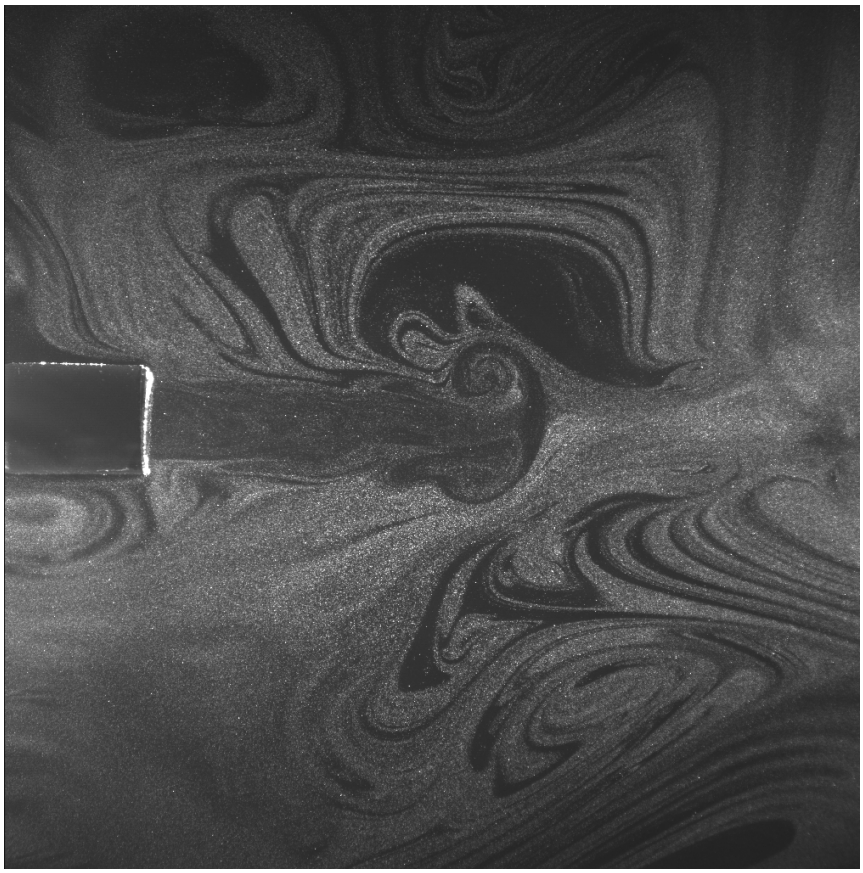

Figure 3.11: Raw PIV image from benchtop experiments.

cases, the camera was mounted perpendicular to the laser sheet passing through the centerline of the tube exit cross section. The schematic for this arrangement is shown in Fig. 3.12.

As for the jet vectoring configuration the same setup was used except in cross flow measurements wherein a prism was placed just downstream of the actuators so that the CCD camera, the laser and optics could all be mounted outside the wind tunnel. 63 pairs of images were captured for all these wind tunnel tests while the resolution was between 97 pix/cm and 269 pix/cm. The vertical field of view was about 4 cm for the thrusters and around 10 cm for the vectoring actuators. Similar to the benchtop experiments, a raw PIV image from the jet vectoring actuators can be seen in Fig. 3.13 where due to the small amounts of mixing at low tunnel speeds,

circular flow structures can be observed. These structures, however, do not affect the velocity calculations due to the WaLPT algorithm used.

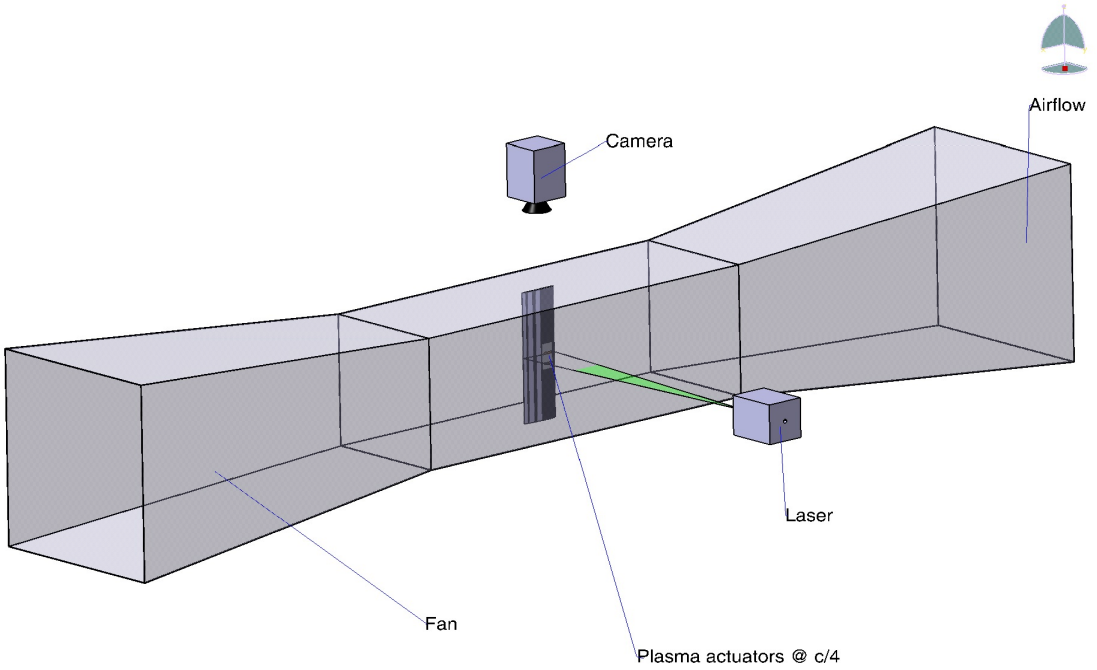

Figure 3.12: Schematic of experimental setup for the wind tunnel.

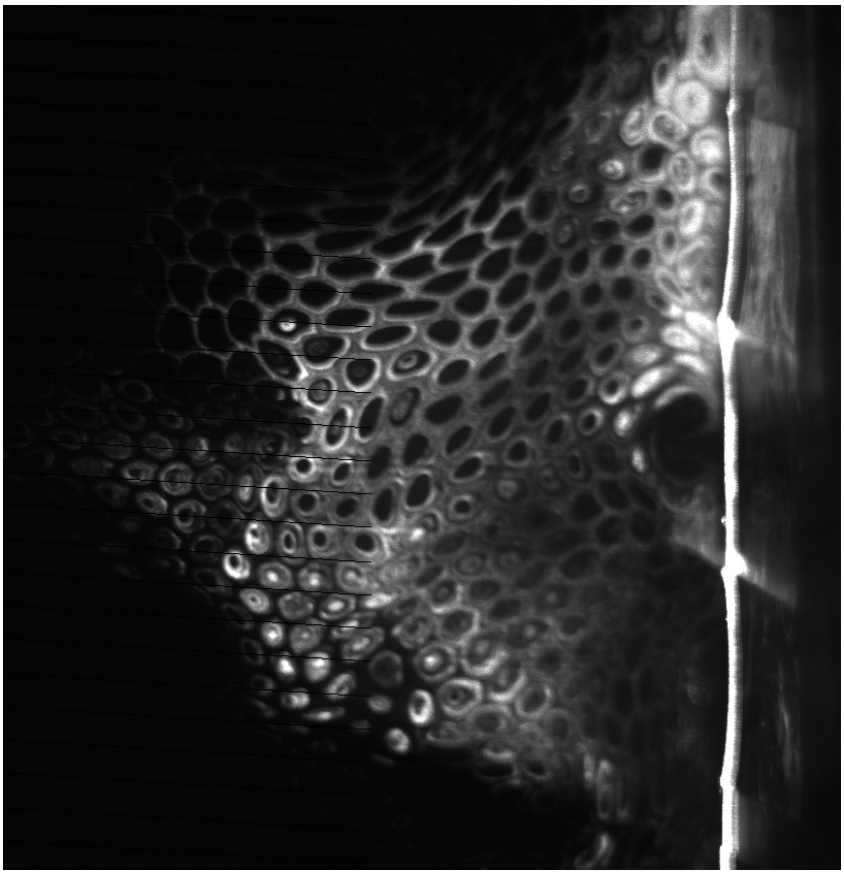

Figure 3.13: Raw PIV image from wind tunnel experiments.

CHAPTER 4

Plasma Thruster

4.1 Single Thruster Configuration

The micro thruster capabilities of the plasma actuator configuration shown in Fig. 1.3 were investigated by varying several important parameters in the tests: the inner diameter, forcing frequency and the duty cycle. The thrust obtained is dependent upon the area of the jet, density of the air and the square of the velocity. Thus, the velocity induced by the actuator was measured by PIV in order to get transient & averaged results. Laser flow visualization was also utilized to observe detailed flow structure at the jet exit. In Fig. 4.1(a), multiple vortex rings immediately after pulsed actuation can be seen. During this pulsed plasma actuation, the vortex rings evolve into a turbulent jet as in Fig. 4.1(b) and (c).

4.1.1 Benchtop Tests

The first set of runs were carried out using three cylindrical tubes of d_i=0.635 cm, d_i=1.016 cm and d_i=1.27 cm inner diameters having the same length of ℓ=5.08 cm and t=0.127 cm thickness. This thruster configuration was tested for 50% DC at plasma waveform frequencies of 5000 Hz and different modulation frequencies of 1 Hz, 2 Hz, 5 Hz, 10 Hz, 100 Hz and 500 Hz for a single diameter. The same procedure was repeated for the other two thrusters with all other parameters identical.

One other set of runs consisted of varying only the duty cycle to observe its effect on the velocities induced. All three tubes of different diameters were tested for DC values of 100%, 90%, 50% and 10% for several cases of constant forcing frequency.

The data obtained for the induced velocity was used to calculate the thrust for these tubes. Then, the thrust, maximum velocity and mean velocity were plotted against the forcing frequencies for 50% and 10% duty cycles.

Three larger tubes of diameters d_i=1.524 cm, d_i=2.159 cm and d_i=3.048 cm were included in the analysis of the velocity profiles so that the influence of the (ℓ/d_i) ratio could be observed more clearly. Note that even though the lengths of these tubes are the same, the radial thicknesses vary for the largest three, being 0.254 cm and 0.508 cm for the first two and the last one, respectively.

Downstream variation of the maximum and mean velocities for steady runs and different diameters is shown in Fig. 4.2. These time averaged velocities increase, reach their peak value at a certain downstream location, then decrease for all three tubes. The effect of pulsing with different forcing frequencies on these velocities can be seen in Fig. 4.3. Note that the curves for different diameters are offset for clarity. When the plots are considered, it can be observed that the frequency at which a peak velocity occurs for each tube is different. It is also clear that the maximum velocity changes in the range of 50 cm/s and 120 cm/s for the 1.27 cm diameter tube for all frequencies whereas for the 1.016 cm diameter tube, the limits of the range have decreased; they are between about 15 cm/s and 45 cm/s. What is interesting to note is that the maximum velocity distribution of the 0.635 cm diameter tube differs significantly from the other two. The values are in the range of 20 cm/s and 100 cm/s and are much higher than that of the 1.016 cm diameter. The average velocity distribution for all three tubes follow the same trend but the peak velocities are the highest for the 1.27 cm, 0.635 cm and 1.016 cm diameter tube respectively.

Fig. 4.4 reveals the effect of changing the duty cycle on the maximum and mean velocity. It is clear that increasing the duty cycle results in higher velocities and in Fig. 4.4(a) and (b), it can be seen that all plots are similar and follow the same trend. This suggests that the distribution of the velocities is dependent upon the (ℓ/d_i) ratio.

In going from the 5 Hz to the 100 Hz case, the velocity levels increase as well, but note that there is a considerable increase in the maximum velocity for the 50% DC case while the changes are not that apparent fro the 90% and 100% DC cases. It can then be said that the effect of the forcing frequency is reduced at higher duty cycles. Fig. 4.4(c) presents the effect of 10% DC, the resulting velocities are very low relative to the 50% and steady cases. It could also be seen from Fig. 4.4(d) that the values of both the maximum and the average velocities increase for the 1.27 cm diameter tube, once again proving the effect of a larger inner diameter.

Comparisons for the thrust, maximum velocity and mean velocity distributions for the three diameters at 50% DC can be observed in Fig. 4.5. The 1.27 cm diameter tube provides the largest thrust; a peak value of 4.695 mg at 100 Hz. The maximum thrust value for the 1.016 cm diameter tube is 0.284 mg at 5 Hz, while for the smallest diameter of 0.635 cm, this value goes down to 0.00977 mg at 100 Hz. It can be seen that there is a considerable amount of drop in the thrust as the (ℓ/d_i) ratio increases. This is not the case for the velocity distributions though, as the maximum velocity for the 0.635 cm diameter tube is greater than that of the 1.016 cm diameter tube; having values of 98.66 cm/s and 62.92 cm/s respectively. The average velocities of these two diameters are very close, which can be explained by the fact that the smaller diameter has a "peakier" velocity profile with higher maximum velocities while the larger diameter tube has a "broader" profile with smaller maximum velocities.

Fig. 4.6, 4.7 and 4.8 consist of these distributions at 50% DC for each diameter separately. For the 0.635 cm diameter tube in Fig. 4.6, the peak values of thrust, maximum and mean velocity occur at 100 Hz; 0.00977 mg, 98.66 cm/s and 15.77 cm/s respectively. Even though the maximum values occur at the same point, the distribution of the thrust, maximum and mean velocity with the frequency differs. Similarly, the values obtained for the 1.016 cm diameter tube are as in Fig. 4.7 with 0.284 mg of maximum thrust and 16.76 cm/s of peak average velocity at 5 Hz, whereas

the peak for maximum velocity is 62.92 cm/s at 10 Hz. Fig. 4.8 reveals the 1.27 cm diameter tube and its distribution for the thrust, maximum and mean velocities. The peak values are found to be 4.695 mg, 115.12 cm/s and 54.48 cm/s respectively at 100 Hz.

The velocity profiles for all six tubes were plotted for different downstream values and compared to one another to see the effect of the (ℓ/d_i) ratio. For tests conducted at a forcing frequency of 5 Hz and 100% DC, it can be seen that the effect of the inner diameter is significant. In the first three cases, Fig. 4.9(a), (b) and (c), where the diameters are smaller, the profile is nearly parabolic with the maximum velocities occurring near the centerline. As the diameter is increased, high velocities are observed in the near wall regions and the centerline velocities are reduced, although they are still considerably large. These profiles at Fig. 4.9(d) occur at downstream locations close to the actuator; the flow starts to develop at further downstream locations. For the last case in Fig. 4.9(e) and (f), the velocities are highest near the walls, leaving the centerline velocity very low throughout the flow field. Note that for the largest diameter examined, a recirculation region with negative velocity is seen at the center of the tube. [57]

Velocity contours and streamlines obtained via PIV detail the difference in the flow field for decreasing the length-to-diameter (ℓ/d_i) ratio from the tube of 1.27 cm inner diameter to the largest 3.048 cm diameter tube, shown in Fig. 4.10. As previously mentioned, the smaller inner diameter would typically yield a parabolic profile while the recirculation region is very apparent in the larger inner diameter tube. The formation and downstream advection of the vortex ring during the initial jet stage for the inner diameter of 1.27 cm can also be observed, shown in Fig. 4.11. It can be seen that at the beginning of the pulse, the vortex ring forms and within a very short time, moves downstream and evolves into the highly turbulent jet. While these streamlines are very effective for the tracking of the vortex rings, phase-locked PIV tests were also

conducted for the same thruster pulsed at a forcing frequency of 5 Hz and 50% DC. This was performed by adding a phase angle between the image capturing process and the input signal. The block diagram can be seen in the modified Labview control panel in Fig. 4.12. Then, the coordinates of the vortex centers were plotted for phase angles varying from -30 degrees to -120 degrees, sufficient to observe an entire pulse, shown in Fig. 4.13. It is clear that the vortex centers spread away in both directions with time as they move downstream of the thruster exit. To investigate how the jet is formed near the plasma, 2D models of the thrust configuration were generated using parallel plates since the teflon tubes are not transparent. While the ranges of values for aspect ratio are expected to be different between the 2D and axisymmetric cases, the formation of the basic structure will be similar within the range of large curvatures used for the ducts (compared to the plasma height). Fig. 4.14 shows the results for 3 different plate gap widths (aspect ratios). In each case, one can easily see that the duct jet is formed by the characteristic plasma wall jet. For small distances between the plates (Fig. 4.14a correlating to high aspect ratio), the jets nearly interact directly with one another, even creating a small region of reverse flow immediately downstream of the wall jets. However, the main flow quickly develops into a parabolic profile. As the channel width increases, the jets become distinct from one another (Fig. 4.14b), resulting in a flow field similar to an annular jet. As the duct length increases, the flow field's double hump profile transitions to a single peak. At high channel widths (Fig. 4.14c), the wall jets become essentially independent and a reverse flow region forms in the interior region between the two.

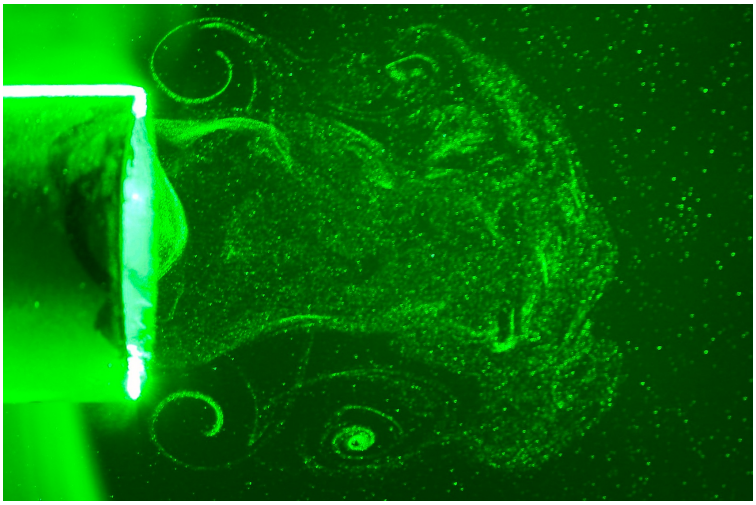

(a) Vortex rings following pulsed actuation

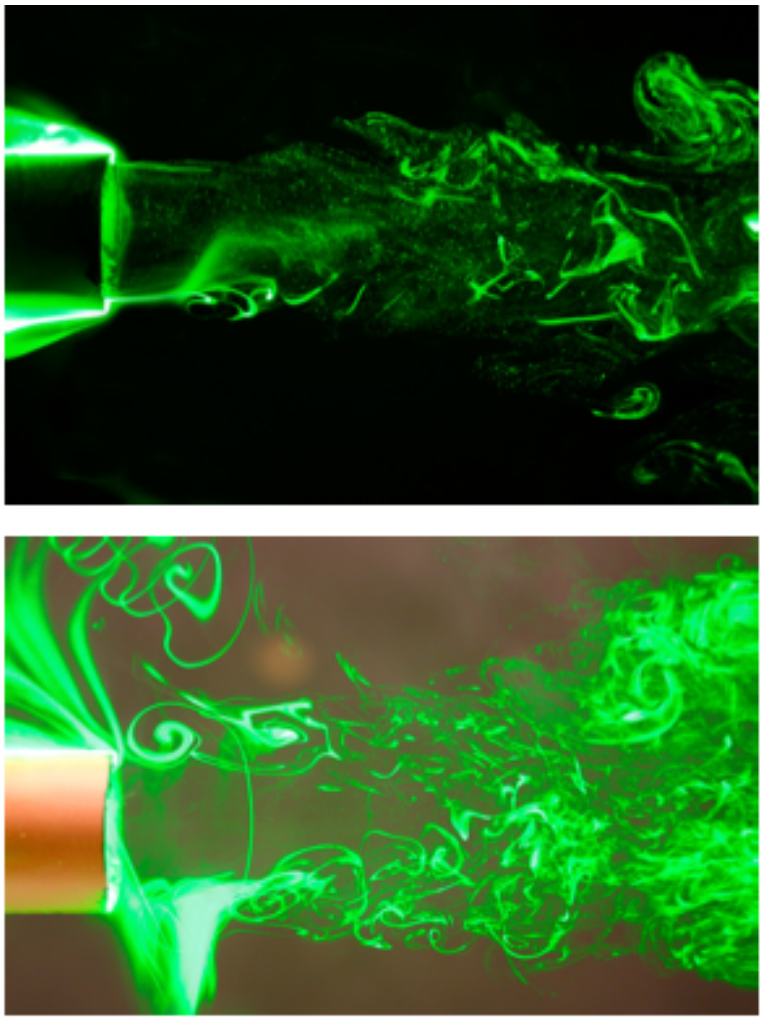

(b) Formation of the turbulent jet as vortex rings evolve

Figure 4.1: Qualitative flow visualization of the flow structure using laser sheet illuminated smoke particles.

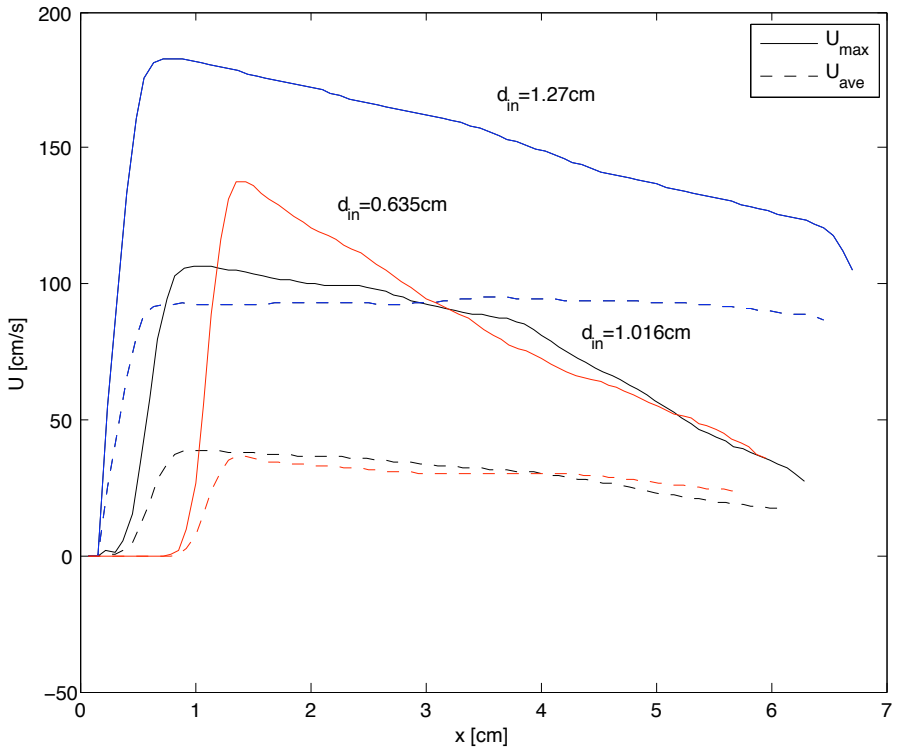

Figure 4.2: Maximum & mean velocities for tubes of inner diameter 1.27 cm, 1.016 cm and 0.635 cm with 100% DC.

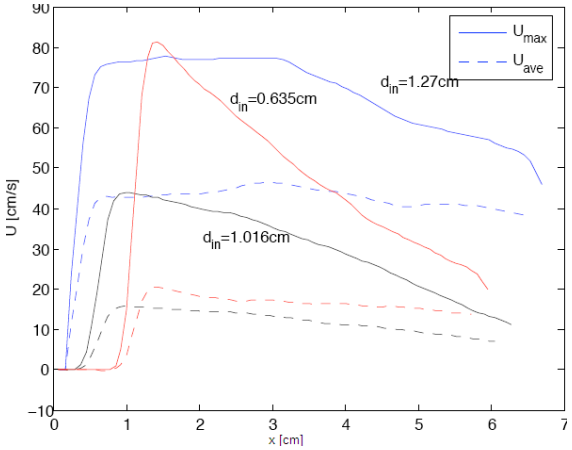

(a) f_p=1 Hz

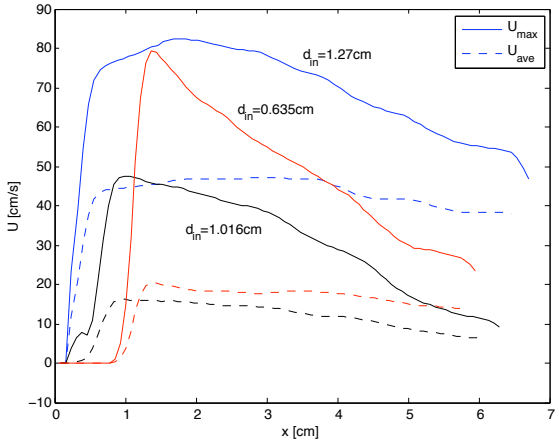

(b) f_p=2 Hz

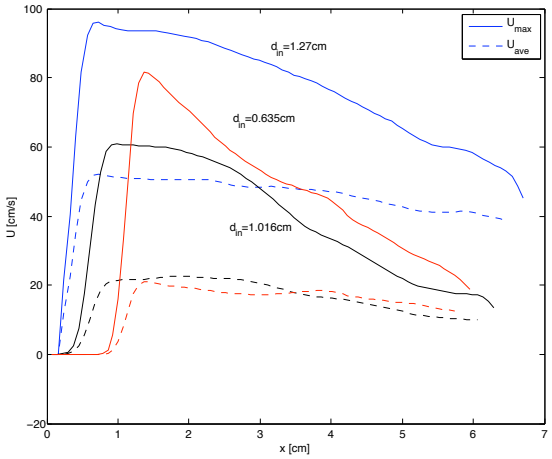

(c) f_p=5 Hz

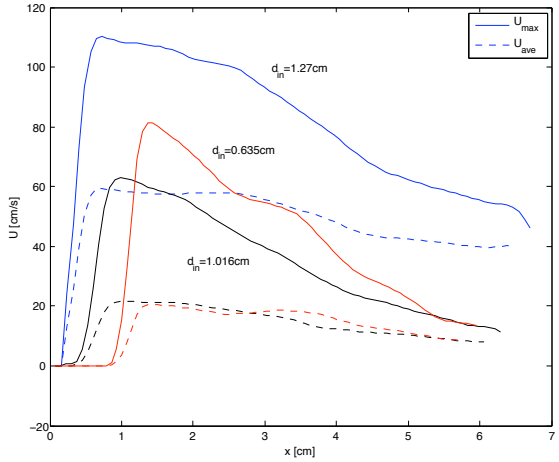

(d) f_p=10 Hz

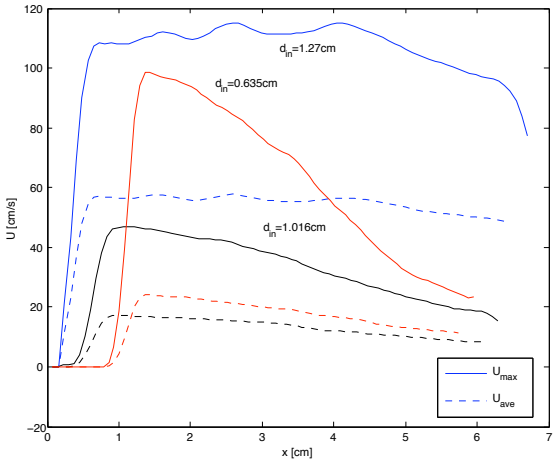

(e) f_p=100 Hz

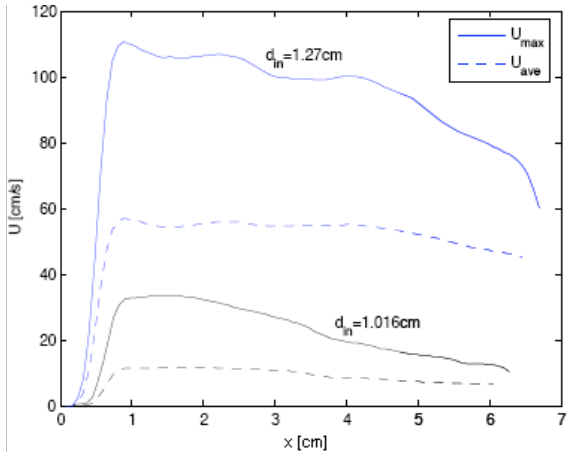

(f) f_p=500 Hz

Figure 4.3: Maximum & mean velocities for tubes of inner diameter 1.27 cm, 1.016 cm and 0.635 cm.

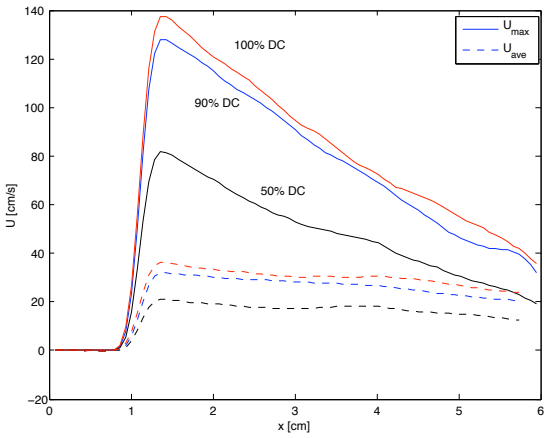

(a) d_i=0.635 cm; f_p=5 Hz

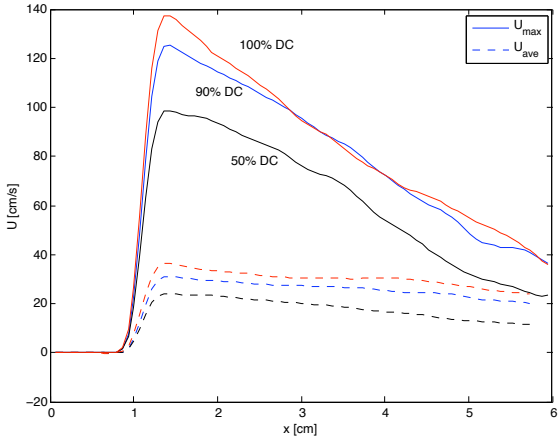

(b) d_i=0.635 cm; f_p=100 Hz

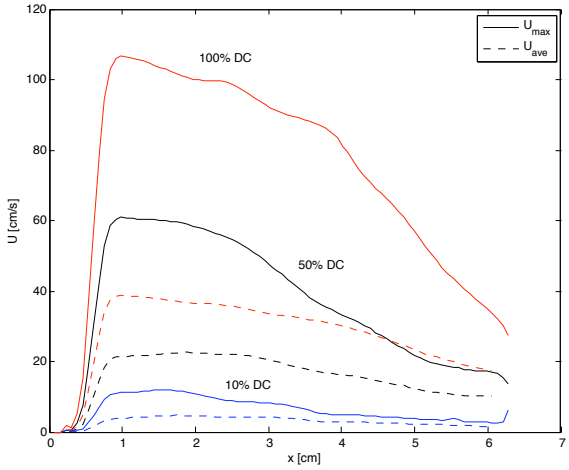

(c) d_i=1.016 cm; f_p=5 Hz

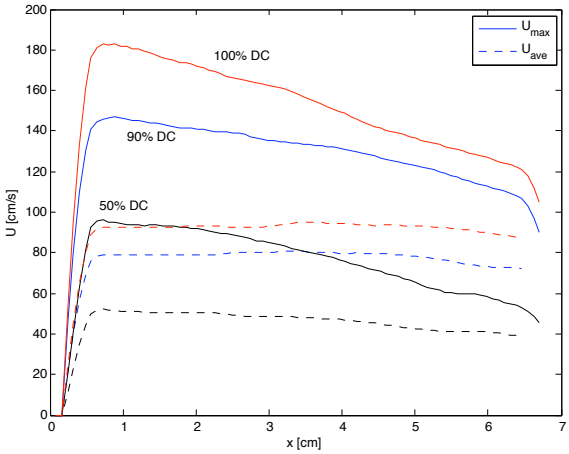

(d) d_i=1.27 cm; f_p=5 Hz

Figure 4.4: Effect of DC on the maximum & mean velocity distribution.

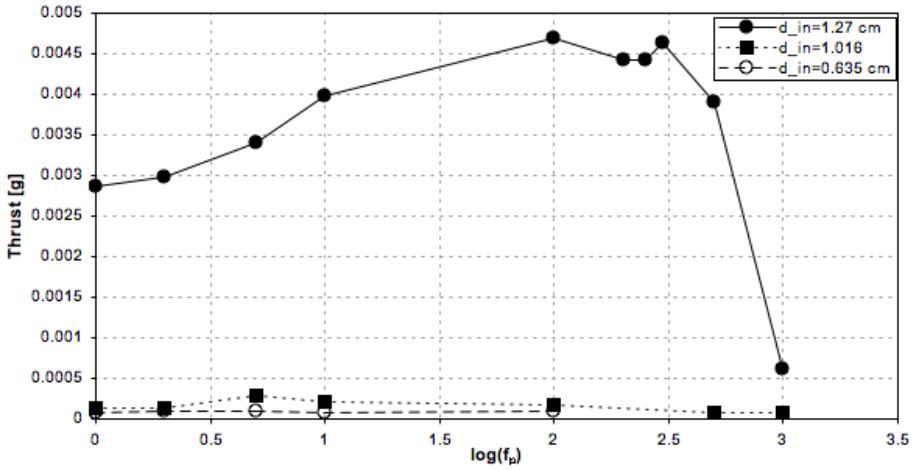

(a) Thrust vs forcing freq.

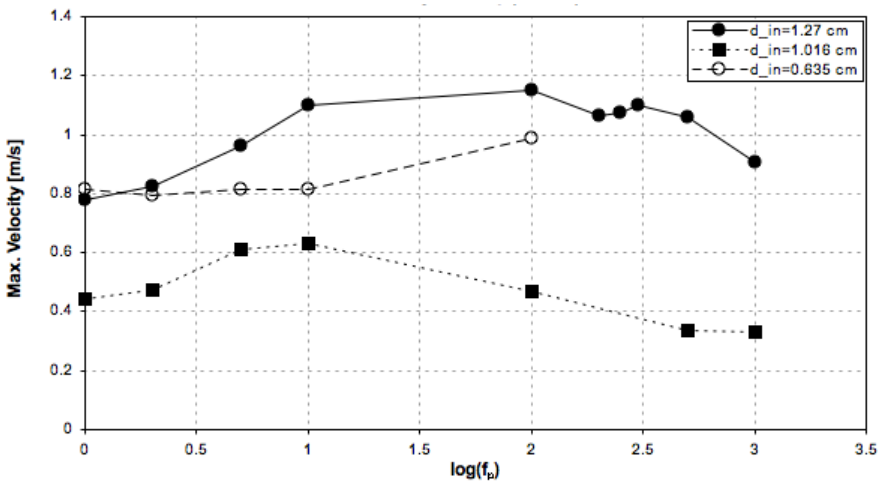

(b) Max velocity vs forcing freq.

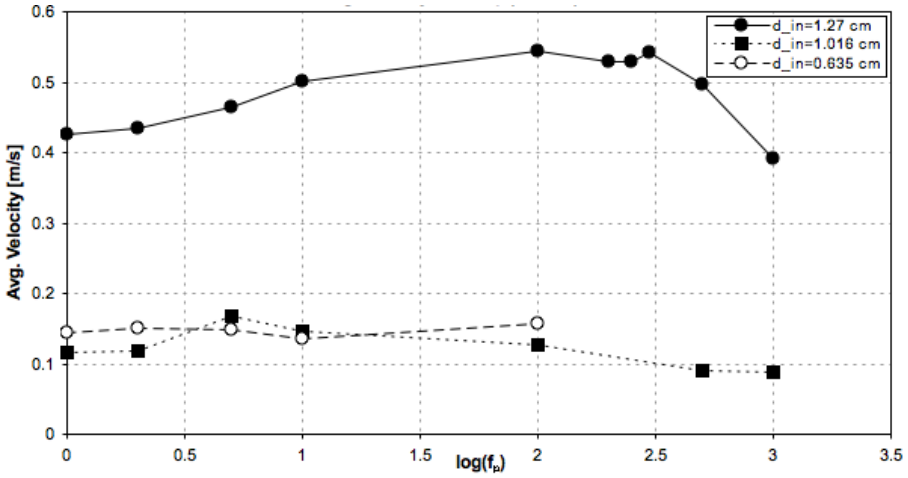

(c) Avg. velocity vs forcing freq.

Figure 4.5: Thrust, maximum velocity and mean velocity distribution with forcing frequency at 50% DC.

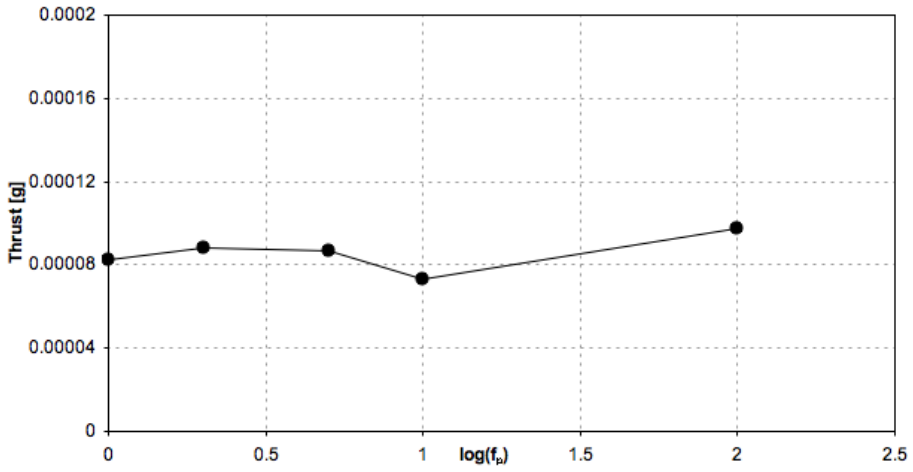

(a) Thrust vs forcing freq.

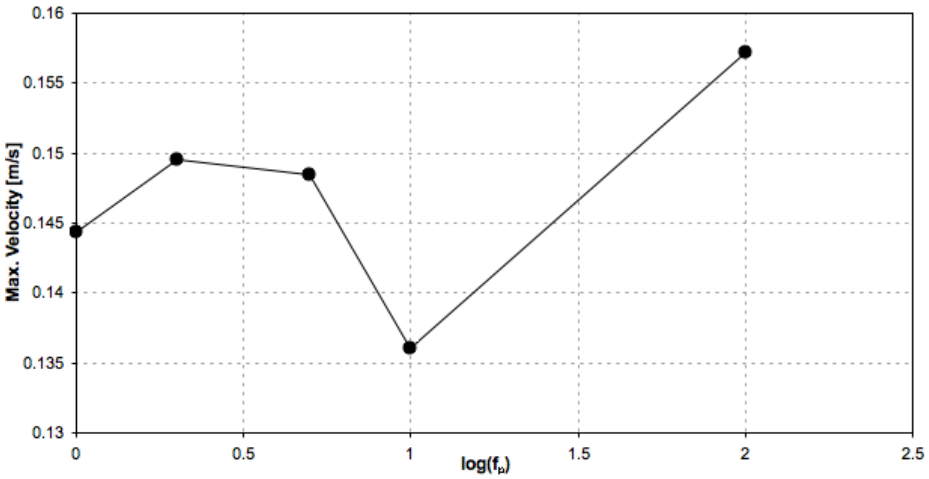

(b) Max velocity vs forcing freq.

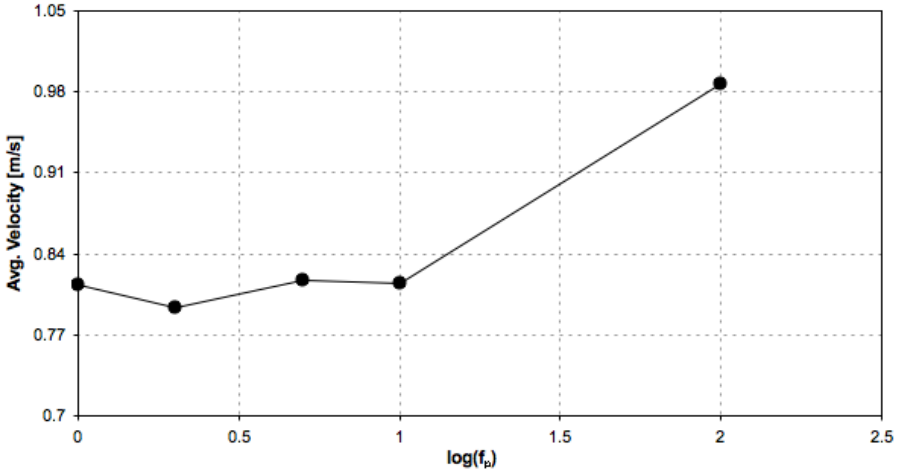

(c) Avg. velocity vs forcing freq.

Figure 4.6: Thrust, maximum velocity and mean velocity distribution for d_i=0.635 cm.

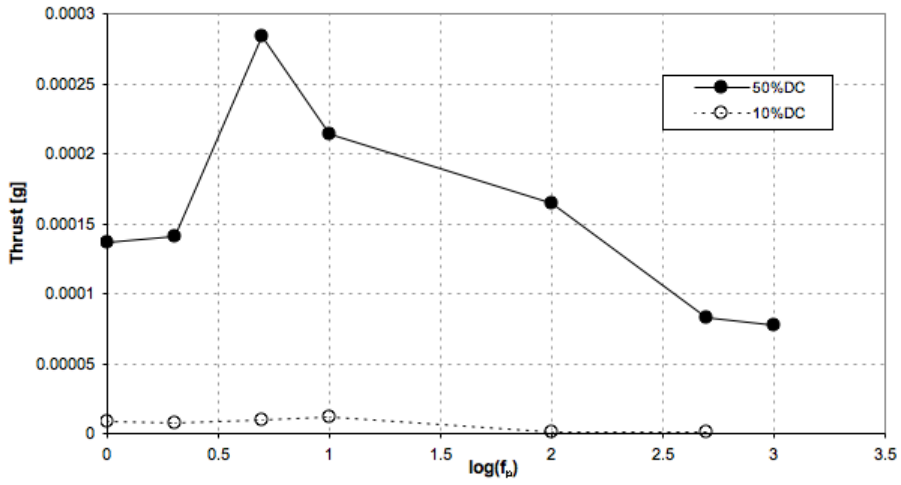

(a) Thrust vs forcing freq.

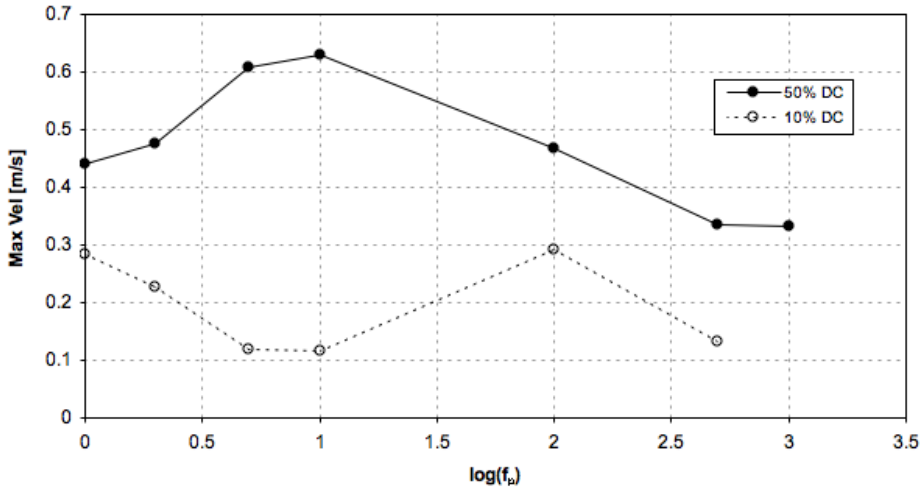

(b) Max velocity vs forcing freq.

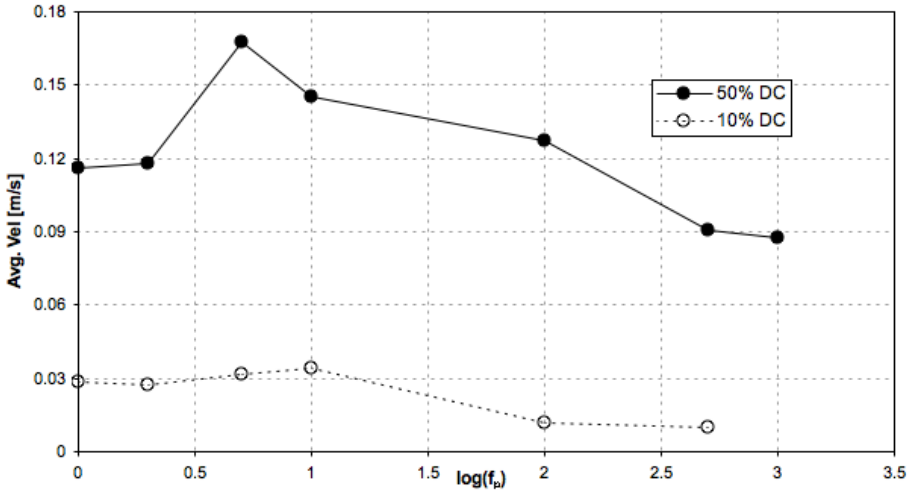

(c) Avg. velocity vs forcing freq.

Figure 4.7: Thrust, maximum velocity and mean velocity distribution for d_i=1.016 cm.

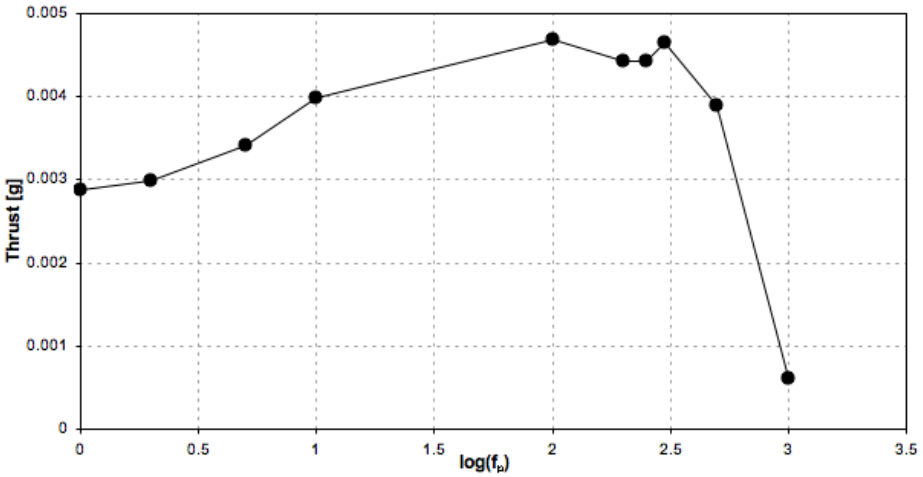

(a) Thrust vs forcing freq.

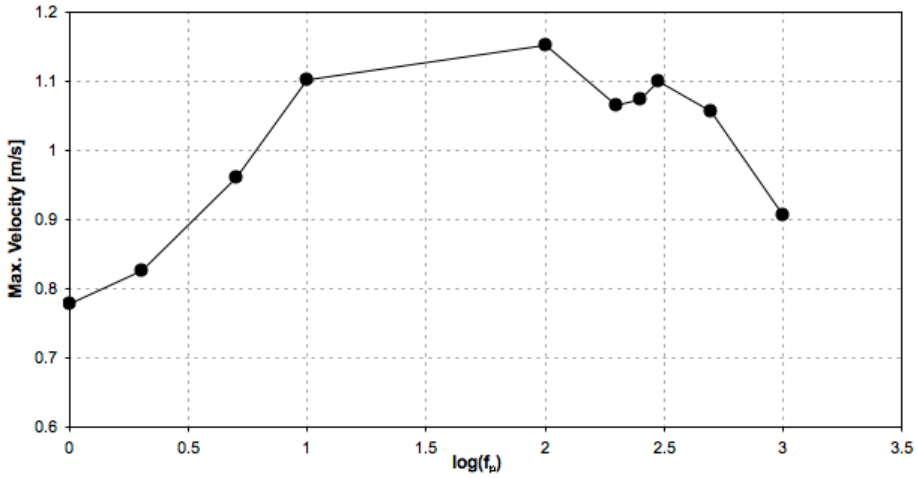

(b) Max velocity vs forcing freq.

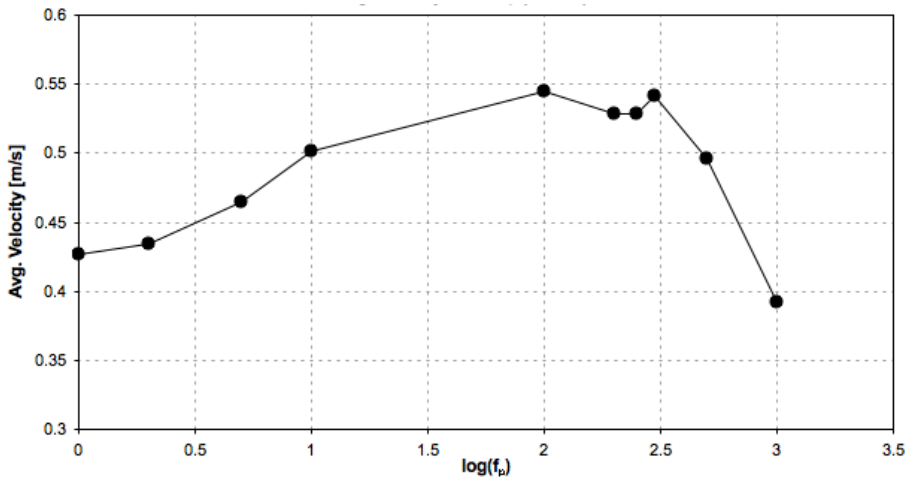

(c) Avg. velocity vs forcing freq.

Figure 4.8: Thrust, maximum velocity and mean velocity distribution for d_i=1.27 cm.

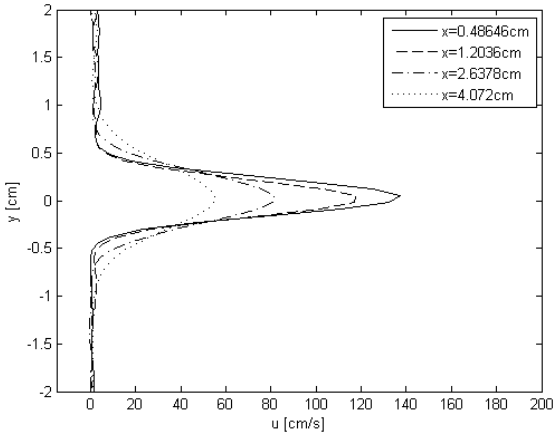

(a) d_i=0.635 cm

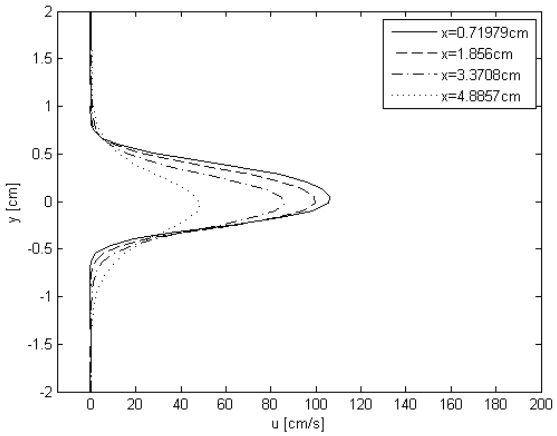

(b) d_i=1.016 cm

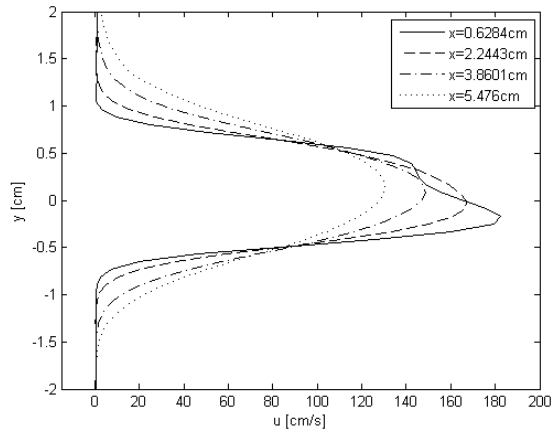

(c) d_i=1.27 cm

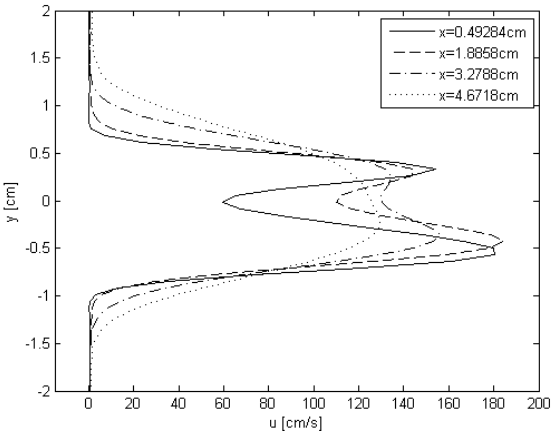

(d) d_i=1.524 cm

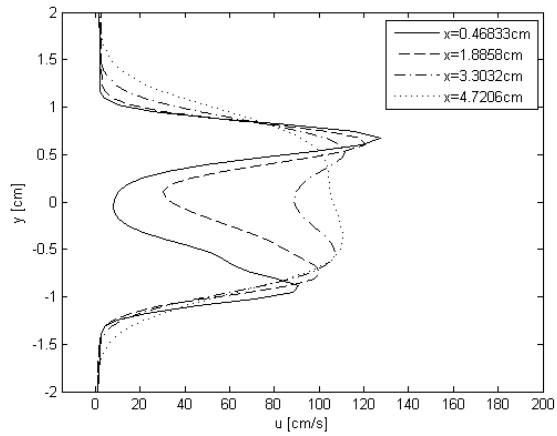

(e) d_i=2.159 cm

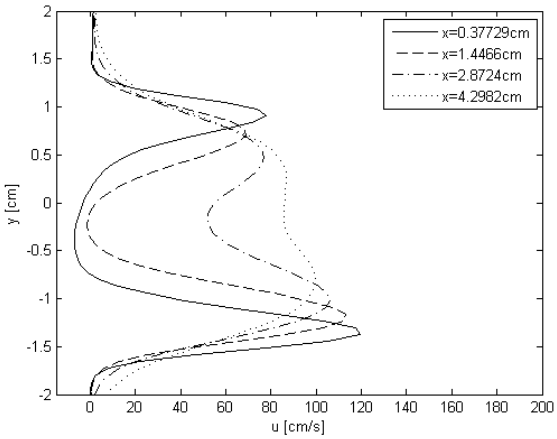

(f) d_i=3.048 cm

Figure 4.9: Velocity profiles at various downstream x-locations with 100% DC.

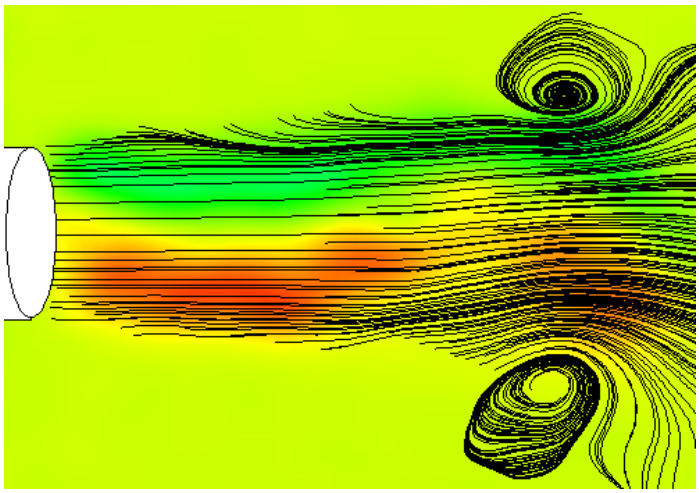

(a) d_i=1.27 cm

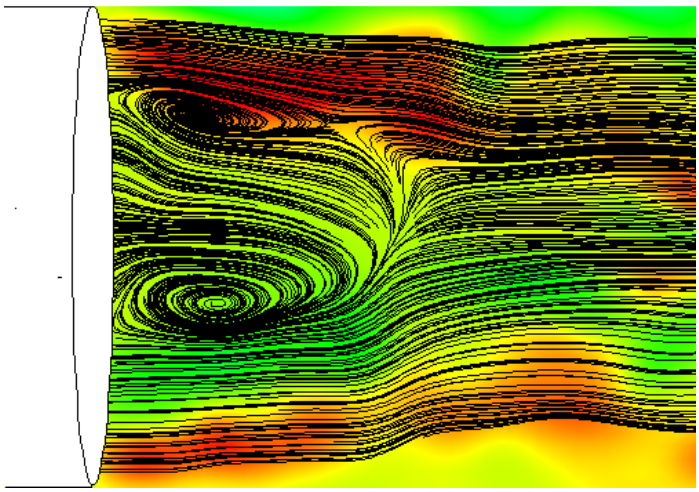

(b) d_i=3.048 cm

Figure 4.10: Streamlines for tubes of 1.27 cm and 3.048 cm inner diameters.

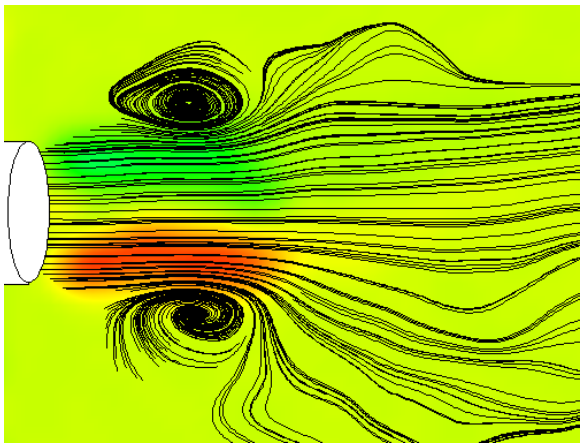

(a) t=50.084 s

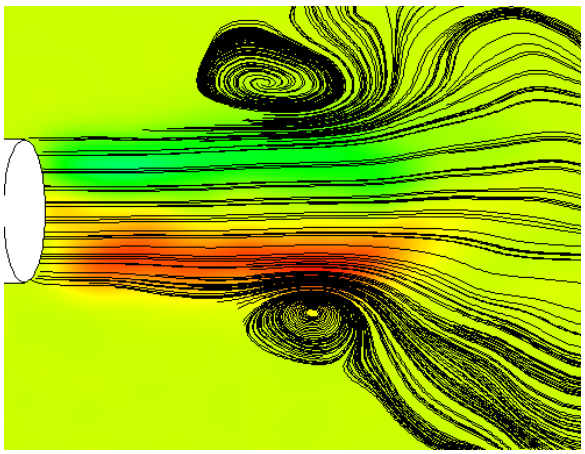

(b) t=50.632 s

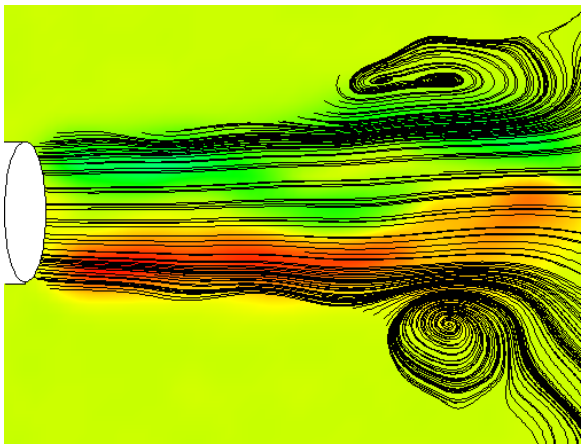

(c) t=51.179 s

Figure 4.11: Formation and advection of vortex ring with time for the 1.27 inner diameter tube.

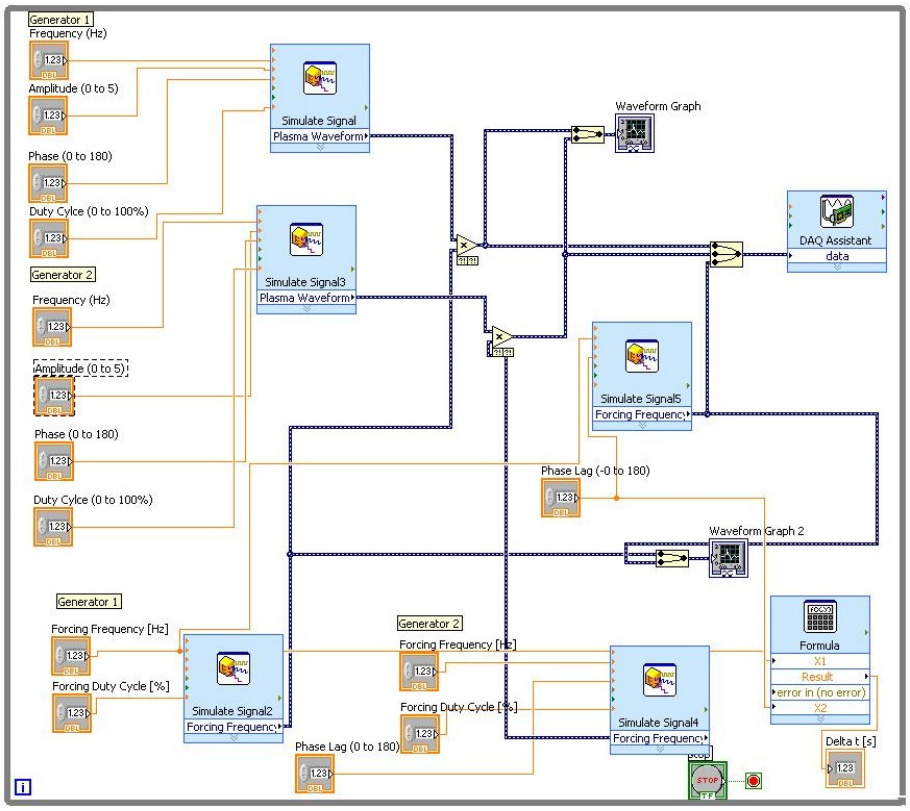

Figure 4.12: Labview block diagram for phase-locked PIV measurements.

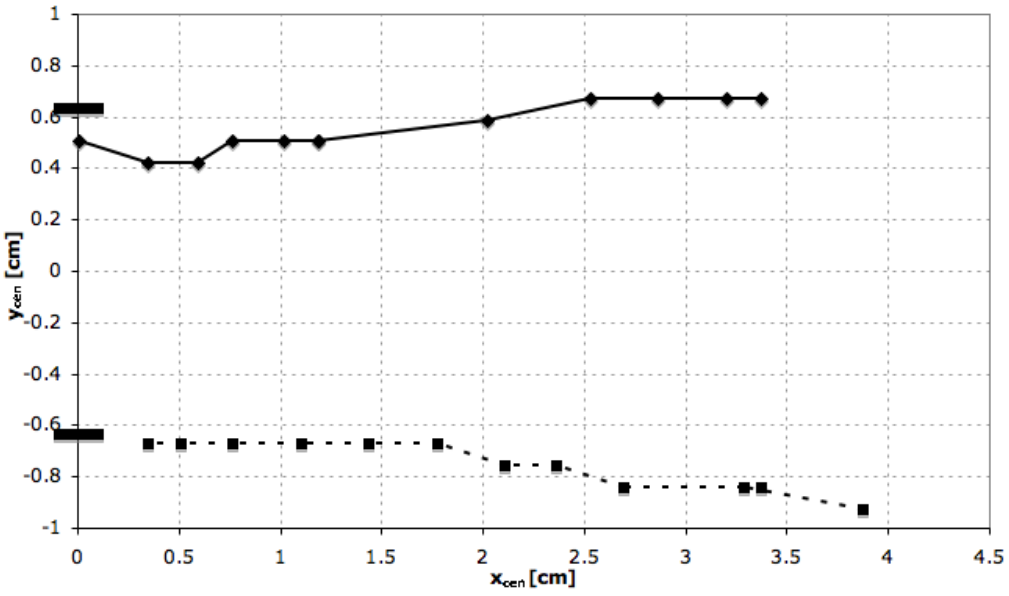

Figure 4.13: Hodograph for tube of inner diameter 1.27 cm at 5 Hz and 50% DC.

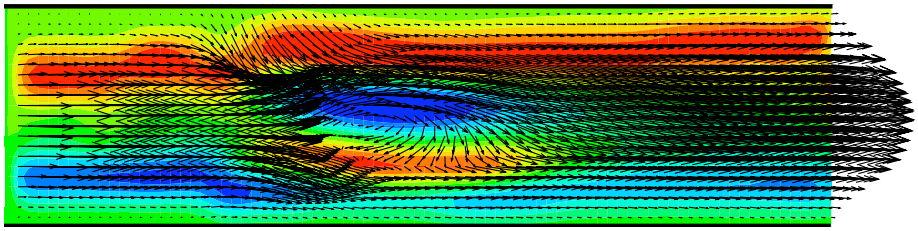

(a) High aspect ratio.

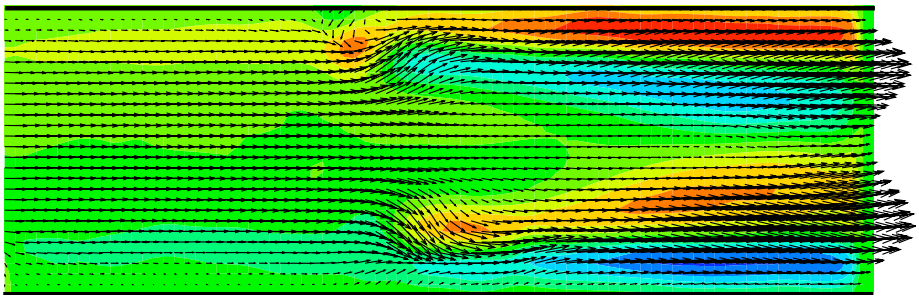

(b) Moderate aspect ratio.

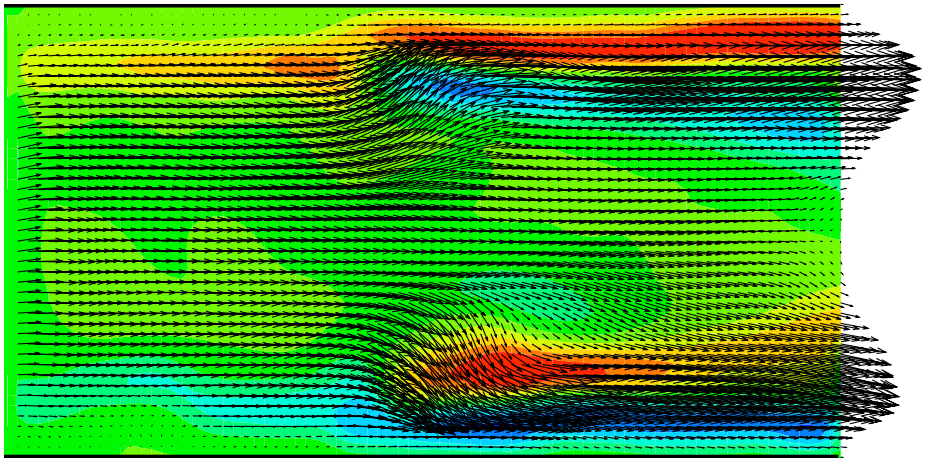

(c) Low aspect ratio.

Figure 4.14: Interior view of the jet formation using a 2D experimental model.

The flow field characteristics of the plasma thruster were compared to that of other devices such as zero-net-mass-flux plasma synthetic jet actuators or synthetic jets as well as conventional jets. The local maximum mean and the inner diameters are used as the normalization parameters for the annular plasma actuators, whereas the normalization parameters for the synthetic and conventional jets are the centerline velocity and the half width. Thus, for the following comparisons, the local maximum mean velocity U_{max}, centerline velocity U_c and the half-width b of the jet are observed. The velocities are non-dimensionalized using the respective peak value of each while the inner diameter is used for the half-width. The half-width is defined as the cross-stream location in the jet at which the mean velocity value at a given streamwise position is half of the peak value at the same location. [58] The downstream distribution of the above non-dimensional values for the smallest tube of inner diameter d_i=0.635 cm are shown in Fig. 4.15. The experimental data for the plasma thrusters are shown with the symbols while the PSJA, synthetic and conventional jets are shown with the solid, dash dotted and dotted lines respectively. The relations for the PSJA's are obtained from experimental data by Santhanakrishnan [59] are shown below.

$$\frac{U_{max}}{U_p} \sim x^{-0.82}, \frac{U_c}{U_{c,p}} \sim x^{-0.93}, \frac{b}{d_i} \sim x^{0.5} \tag{4.1}$$

Using findings from hot wire anemometry by Smith & Glezer [60] and PIV measurements by Béra *et al.* [58] the following relations for synthetic jets was presented.

$$\frac{U_{max}}{U_p} \sim x^{-0.4}, \frac{U_c}{U_{c,p}} \sim x^{-0.58}, \frac{b}{d_i} \sim x^{0.88} \tag{4.2}$$

For the conventional jets, analytical formulations by Schlichting & Gersten [61] below were used.

$$\frac{U_{max}}{U_p} \sim x^{-0.5}, \frac{U_c}{U_{c,p}} \sim x^{-0.5}, \frac{b}{d_i} \sim x \tag{4.3}$$

It can be seen that for all cases, there is a sharp increase in the velocity up to a certain downstream distance, after which it starts decreasing. The decay in the centerline velocity for the thruster and PSJA, shown in Fig. 4.15(a), is much faster than the synthetic and conventional jets which experience this process over significantly larger downstream distances. The maximum velocity distribution in Fig. 4.15(b) illustrates the same behavior, the velocities for the plasma actuators reach their peak value at close downstream distances while this location is further away in synthetic jets. The entrainment near the actuator causes a local minimum velocity to occur, whereas for the conventional jets, unlike the previous three, the immediate exit of the cavity through which air is supplied to create the jet is the location at which the peak values are observed. The peak centerline and maximum velocity (which occur at the same location as seen in Fig. 4.15(a) and (b)) in plasma actuators is explained by the formation, advection and interaction of discrete vortical structures, the mechanism by which the synthetic jet operates, where the starting vortex causes the rapid increase of velocity at locations close to the actuator. Looking at Fig. 4.15(c), one can see that the spreading in both plasma actuators are less than the synthetic and conventional jets; the thruster jet having almost constant width along the streamwise direction. For a larger inner diameter of d_i=1.016 cm, Fig. 4.16(a), (b) and (c) again shows the variation of the maximum and centerline velocities as well as the half-width of the jet. Note that the decrease in the velocities have become more gradual rather than the sharper trend in the smaller inner diameter case, suggesting a resemblance to conventional jets as the inner diameter is increased. Even though the width of the jet has naturally increased, the spreading is very little and even though the PSJA shows a similar behavior to the thruster, the rapid changes in the velocities and the jet spreading is apparent. The changes in the behavior of

the jet are even more significant for the largest inner diameter of d_i=1.27 cm where the velocity variations occur over very large streamwise distances and the spreading of the jet has decreased even more compared to the smallest inner diameter results. Fig. 4.18 - Fig. 4.20 illustrate the variation of the same non-dimensional parameters for the larger three tubes of inner diameters d_i=1.524cm, d_i=2.159 cm and d_i=3.048 cm. For Fig. 4.18(a), it can be seen that the decay in the centerline velocity is now very slow and happens over a significantly large streamwise distance. As seen in the previous velocity profiles, this inner diameter corresponds to a case where the centerline velocities have started decreasing and max velocities can be observed in the near wall regions. Going to the larger inner diameter in Fig. 4.19(a), the centerline velocities are extremely reduced throughout the flow field and the centerline velocity does not reach its peak value until further downstream distances. For the largest tube, recirculation occurs and the centerline velocity is negative as shown in Fig. 4.20(a). The velocity starts increasing in the streamwise direction, but as in Fig. 4.19(a), the peak is not observed until a further downstream location in the flow field. The maximum velocity behaves almost the same for all three tubes; the decay rate has decreased and the decrease occurs gradually along the whole flow field

4.1.2 Wind Tunnel Tests

The plasma thruster configuration was also employed in a low speed wind tunnel to observe effects of the actuator on the induced jet in the presence of a freestream flow. Regarding the results of the benchtop experiments, three of the tubes known to have significantly different velocity profiles with inner diameters of d_i=1.016 cm, d_i=1.524 cm and d_i=3.048 cm were tested in the wind tunnel. Three different tunnel speeds of 0.62 m/s, 1.28 m/s and 2.32 m/s were used while two sets of PIV runs were made for each speed, one with steady actuation and the other with the actuator off.

Fig. 4.21 shows the velocity profiles for the tube with inner diameter d_i=1.016 cm

for the tunnel speeds considered. The effect of the actuator on the jet exit characteristics can be seen clearly in Fig. 4.21(a) and (b) where adding momentum to the boundary layer on either side of the tube reduces the initial momentum deficit and the wake drag is significantly improved while a considerable amount of increase in the velocity values is observed. As the tunnel speed is increased, however, this effect is reduced as seen in Fig. 4.21(c), (d), (e) and (f) where the profiles on the left column with the actuators off are not greatly different than the ones on the right column with nearly the same velocity values.

The velocity profiles for the 1.524 cm inner diameter tube can be seen in Fig. 4.22, where similar to the previous figure, the actuators are efficient for the smaller tunnel speeds and have almost no effect as the speed is increased. It can finally be seen in Fig. 4.23 that the largest tube of inner diameter d_i=3.048 cm is not as effective as the other two and tends to alter the velocity profile primarily for the smallest tunnel speed of 0.62 m/s.

The variation of the maximum and mean velocities with the tunnel speeds is given in Fig. 4.24. It can be observed that higher values are obtained for both the maximum and mean values as the tunnel speed is increased for the three tubes. As mentioned previously, the velocities are also increased for cases with actuation, up to twice its value for the smallest diameter tube at the lowest tunnel velocity. Note that, however, as the tunnel speeds and tube inner diameters are increased, the effect diminishes and the changes in the values are less. In fact, for the two larger tubes with inner diameters 1.524 cm and 3.048 cm, the actuators are totally ineffective when the maximum velocities are considered. No such condition is observed for the mean values though, the actuators have an influence on the velocities for each case observed.

The effectiveness of the actuators were also observed using the non-dimensional parameters of Re, thrust coefficient and power coefficient given by

$$Re_d = \frac{U_\infty d_i}{\nu} \tag{4.4}$$

$$C_T = \frac{T}{\frac{1}{2}\rho U_o A} = \left(\frac{U_e}{U_o}\right)^2 - 1 \tag{4.5}$$

$$C_P = \frac{1}{2}\left(\frac{U_e}{U_o} + 1\right)\left(\frac{U_e}{U_o}\right)^2 - 1 \tag{4.6}$$

where U_o and U_e are the inlet and exit average velocities of the thruster, thus $U_o = U_\infty$. Fig. 4.25 illustrates the behavior of the three thrusters. Re number is an indicative of the tunnel speed and the tube inner diameter, thus it combines both parameters in one. It can be seen that both the thrust and power coefficients follow the same trend (power coefficient values are higher) in that they decrease with increasing Re, which agrees with the velocity vs. tunnel speed plots and profiles shown previously, indicating that the efficiency of the actuators decrease with increasing inner diameter and tunnel speed. Thus, as the inner diameter increases, it can be observed that the curve shifts down and negative coefficients can start to be seen for the largest tube. If the actuators were not on, all coefficients would be negative because of the increased adverse pressure gradient in small diameter tubes and so, the smallest inner diameter tube would yield the lowest coefficients. However, the actuators help overcome this and the coefficients become positive. As noted though, increasing inner diameters and tunnel speeds decrease actuator effectiveness and this is why lower negative values are obtained for the thruster with inner diameter d_i=1.524 cm at higher tunnel speeds (the value is close to its original place with the actuator off), thus taking both parameters into account, the inner diameter and the tunnel speed that yields positive values of the coefficients should be chosen.

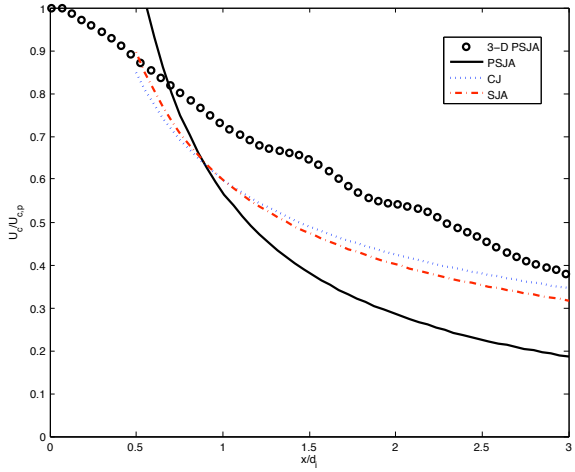

(a) Centerline velocity vs x/d_i.

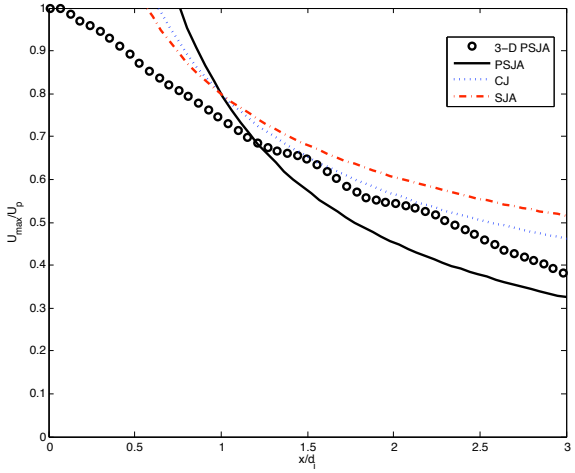

(b) Maximum mean velocity vs x/d_i.

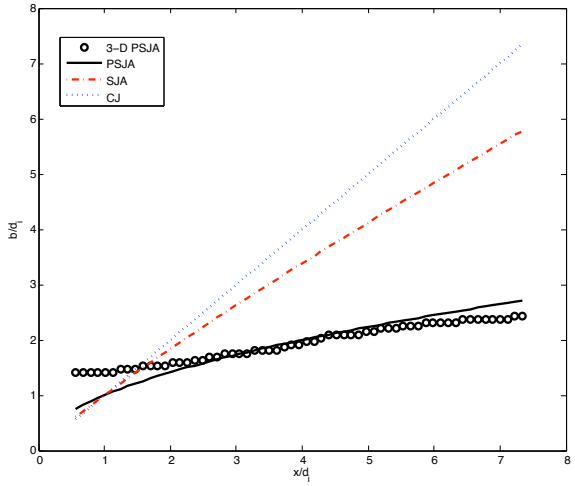

(c) Half width vs x/d_i.

Figure 4.15: Streamwise distribution of non-dimensional jet characteristics for d_i=0.635 cm.

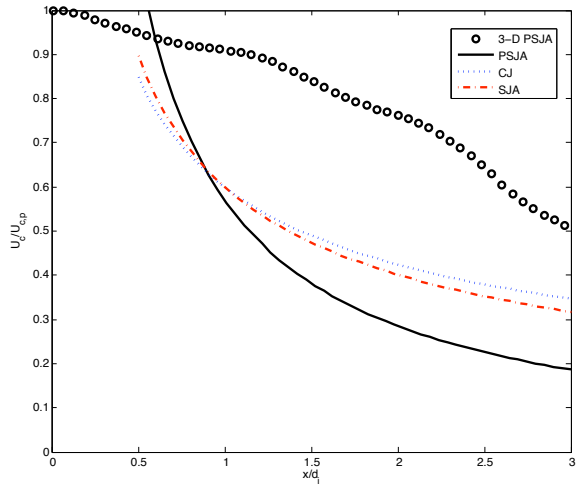

(a) Centerline velocity vs x/d_i.

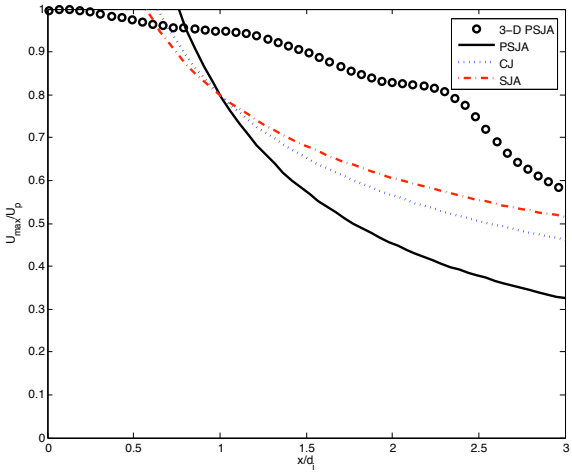

(b) Maximum mean velocity vs x/d_i.

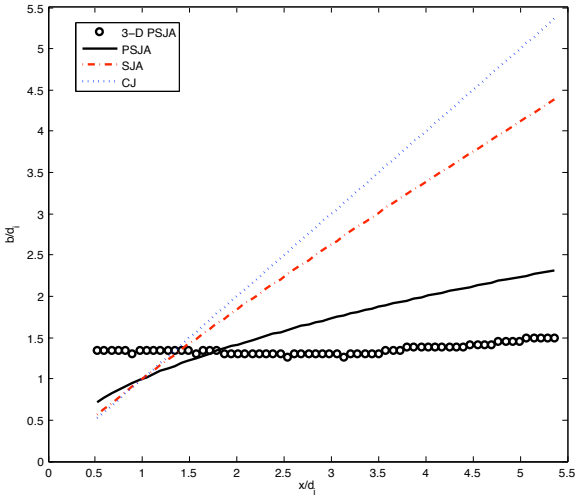

(c) Half width vs x/d_i.

Figure 4.16: Streamwise distribution of non-dimensional jet characteristics for d_i=1.016 cm.

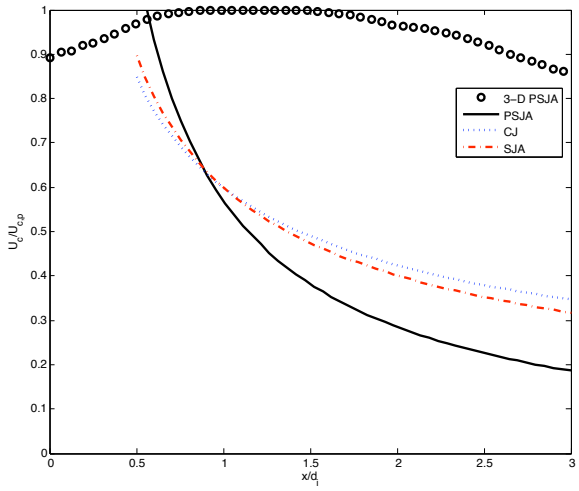

(a) Centerline velocity vs x/d_i.

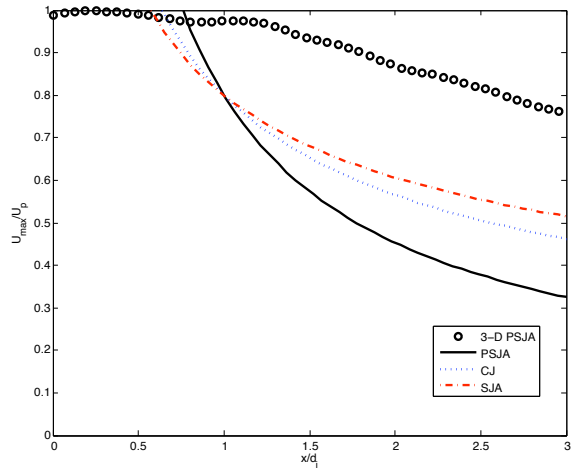

(b) Maximum mean velocity vs x/d_i.

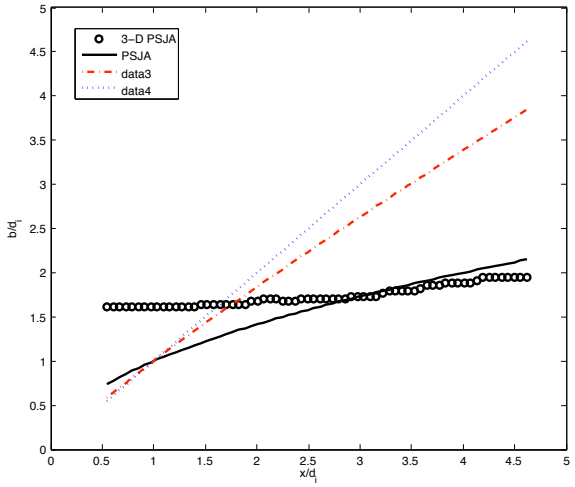

(c) Half width vs x/d_i.

Figure 4.17: Streamwise distribution of non-dimensional jet characteristics for d_i=1.27 cm.

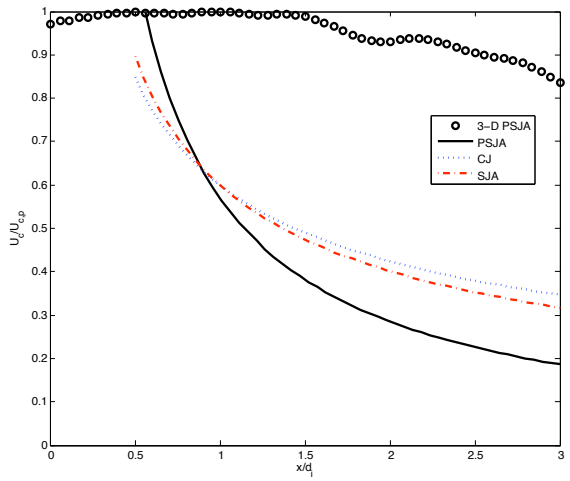

(a) Centerline velocity vs x/d_i.

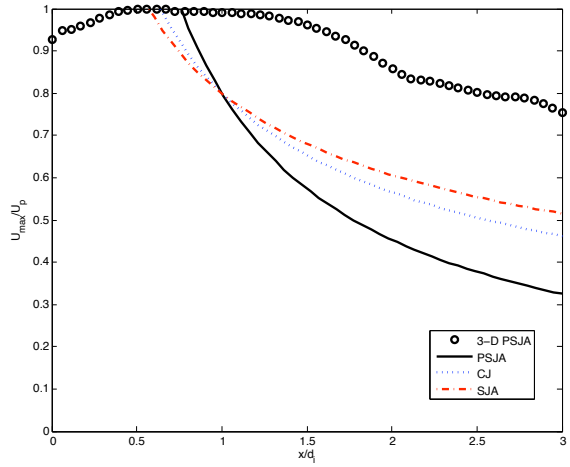

(b) Maximum mean velocity vs x/d_i.

Figure 4.18: Streamwise distribution of non-dimensional jet characteristics for d_i=1.524 cm.

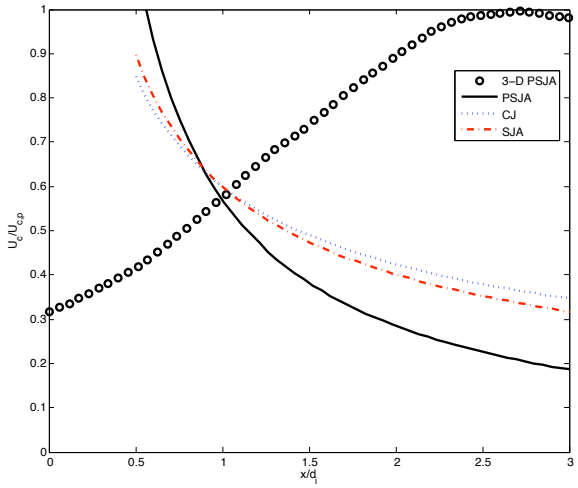

(a) Centerline velocity vs x/d_i.

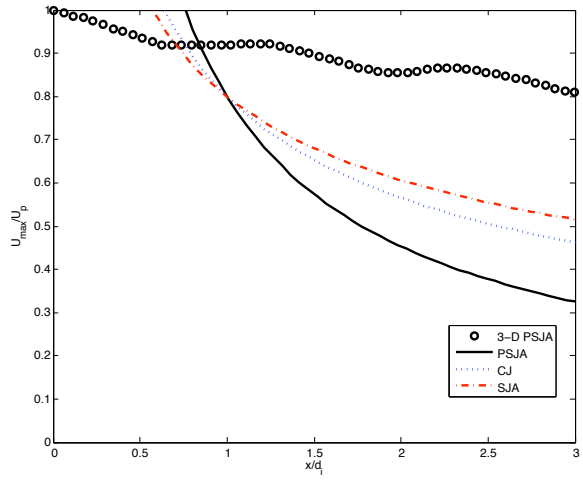

(b) Maximum mean velocity vs x/d_i.

Figure 4.19: Streamwise distribution of non-dimensional jet characteristics for d_i=2.159 cm.

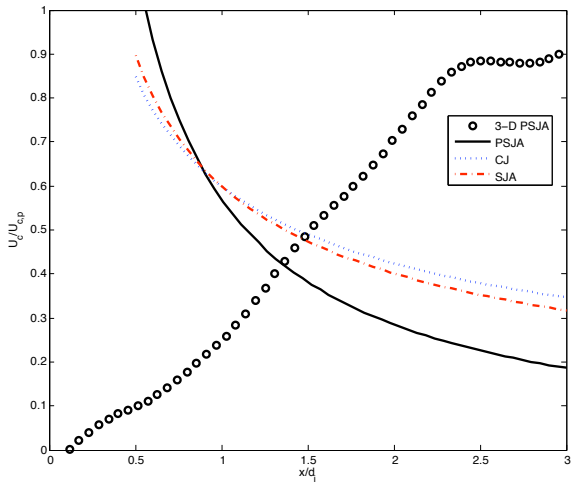

(a) Centerline velocity vs x/d_i.

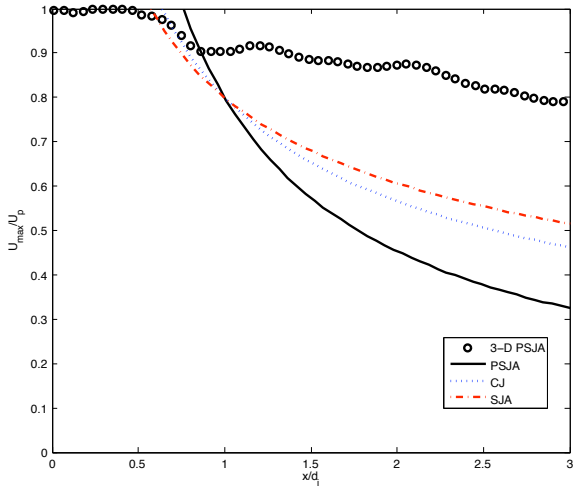

(b) Maximum mean velocity vs x/d_i.

Figure 4.20: Streamwise distribution of non-dimensional jet characteristics for d_i=3.048 cm.

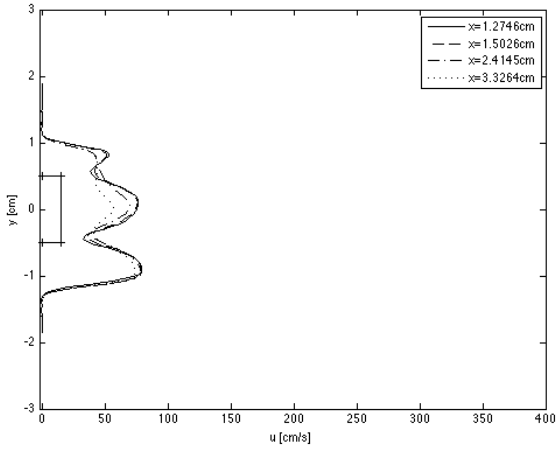

(a) Actuator off, tunnel speed=0.62 m/s

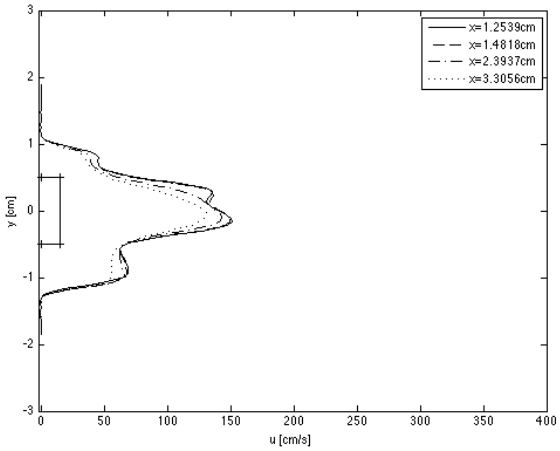

(b) 100% DC, tunnel speed=0.62 m/s

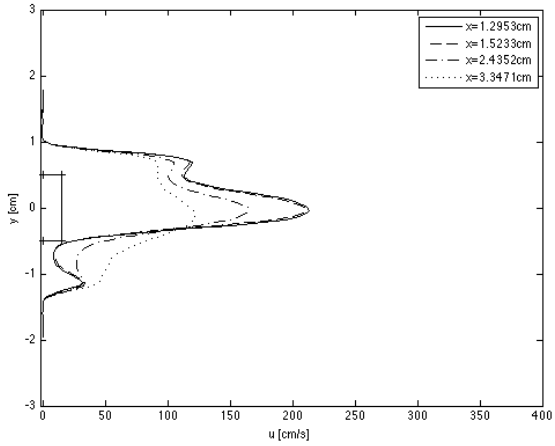

(c) Actuator off, tunnel speed=1.28 m/s

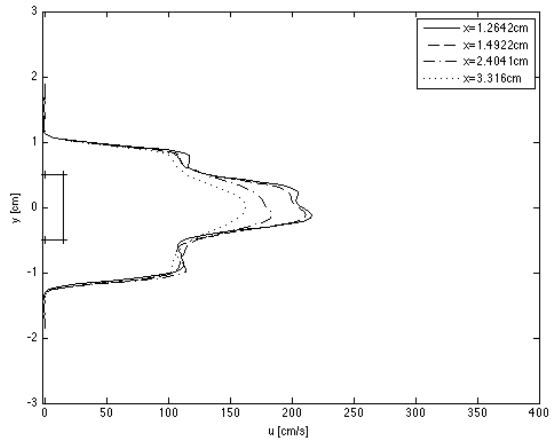

(d) 100% DC, tunnel speed=1.28 m/s

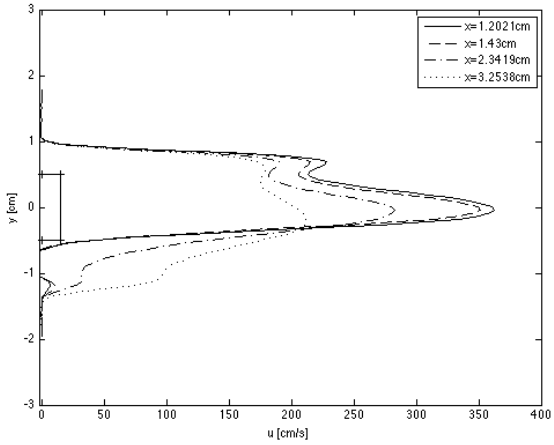

(e) Actuator off, tunnel speed=2.32 m/s

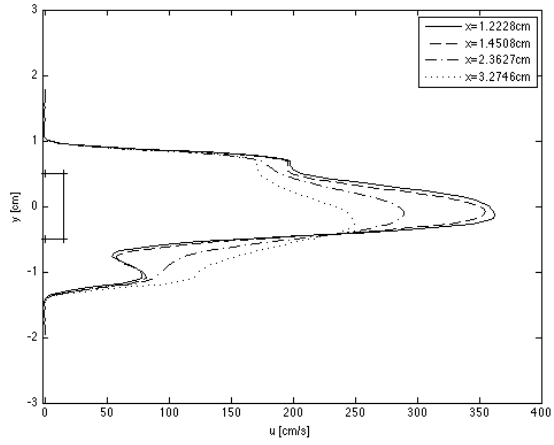

(f) 100% DC, tunnel speed=2.32 m/s

Figure 4.21: Velocity profiles for the tube with d_i=1.016 cm at tunnel speeds of 0.62 m/s, 1.28 m/s and 2.32 m/s.

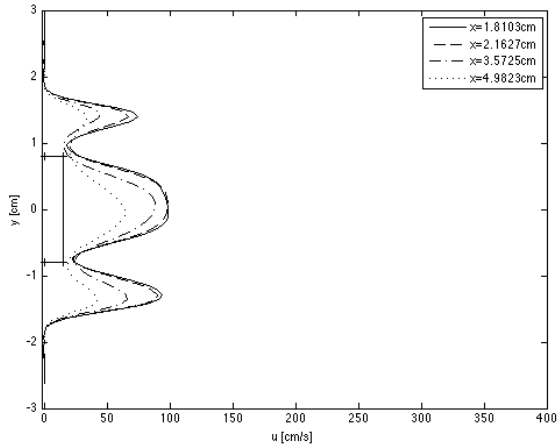

(a) Actuator off, tunnel speed=0.62 m/s

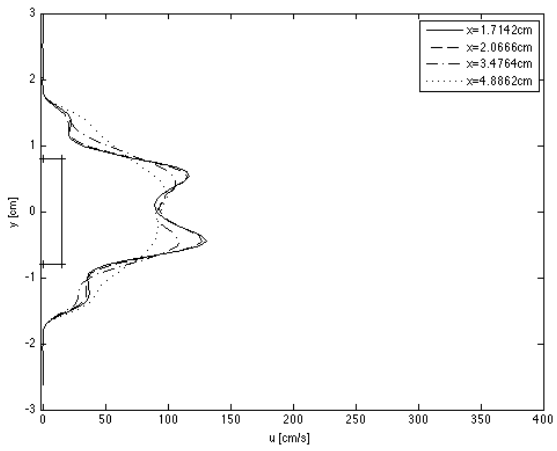

(b) 100% DC, tunnel speed=0.62 m/s

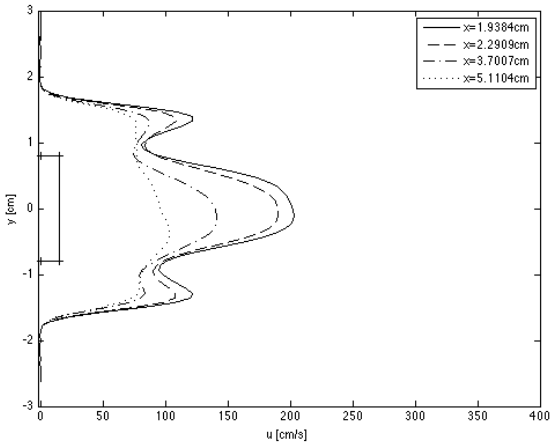

(c) Actuator off, tunnel speed=1.28 m/s

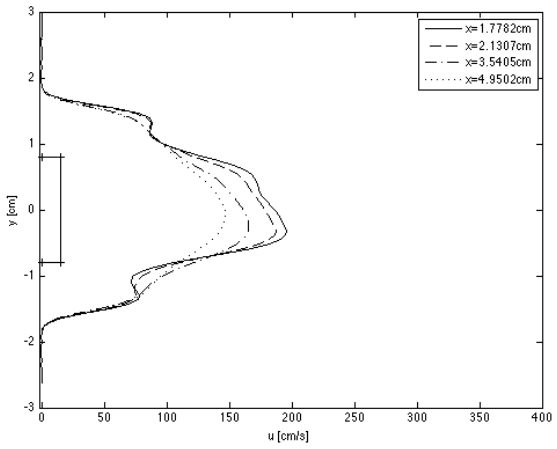

(d) 100% DC, tunnel speed=1.28 m/s

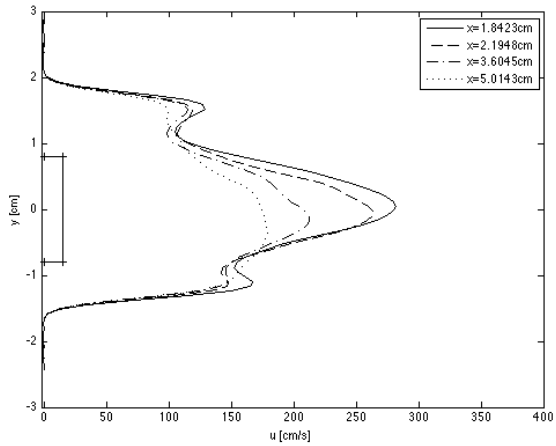

(e) Actuator off, tunnel speed=2.32 m/s

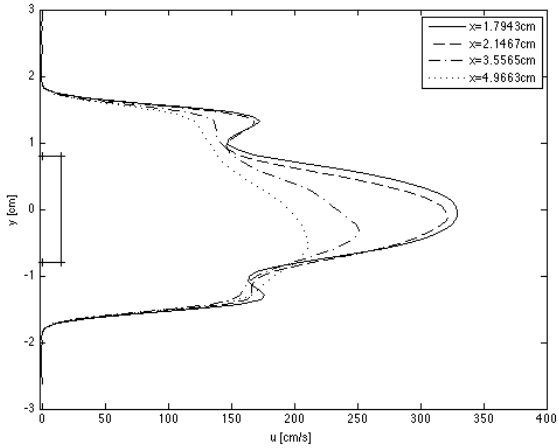

(f) 100% DC, tunnel speed=2.32 m/s

Figure 4.22: Velocity profiles for the tube with d_i=1.524 cm at tunnel speeds of 0.62 m/s, 1.28 m/s and 2.32 m/s.

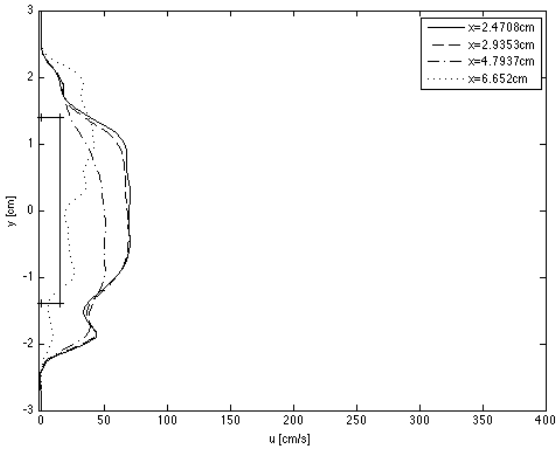

(a) Actuator off, tunnel speed=0.62 m/s

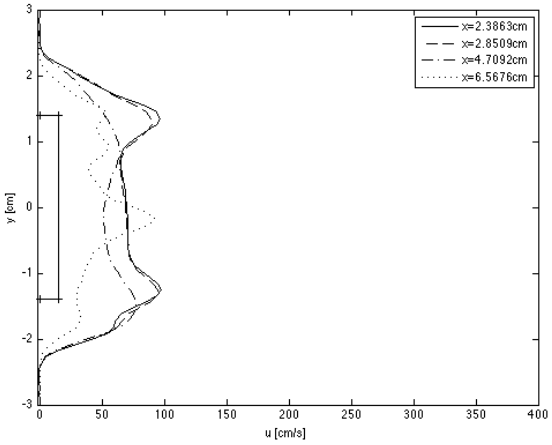

(b) 100% DC, tunnel speed=0.62 m/s

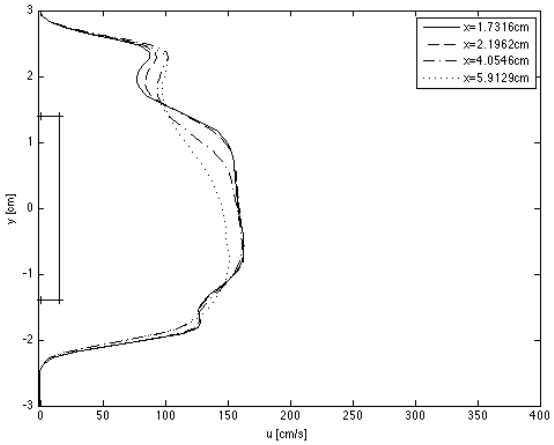

(c) Actuator off, tunnel speed=1.28 m/s

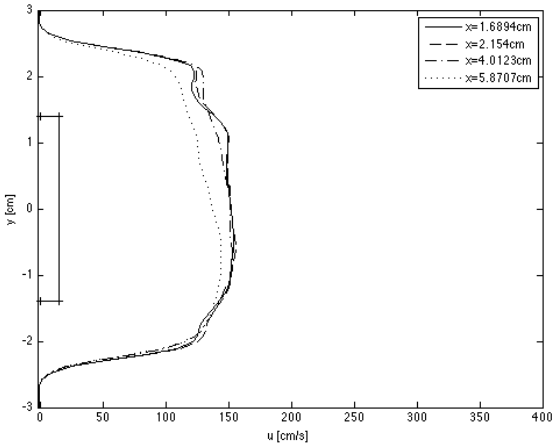

(d) 100% DC, tunnel speed=1.28 m/s

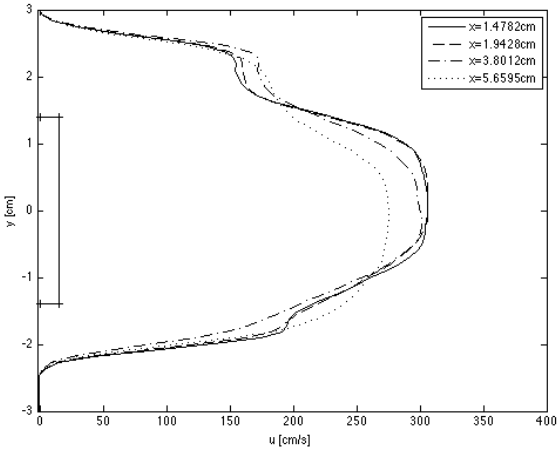

(e) Actuator off, tunnel speed=2.32 m/s

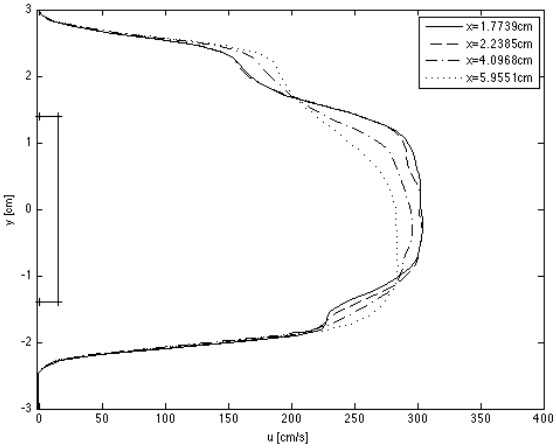

(f) 100% DC, tunnel speed=2.32 m/s

Figure 4.23: Velocity profiles for the tube with d_i=3.048 cm at tunnel speeds of 0.62 m/s, 1.28 m/s and 2.32 m/s.

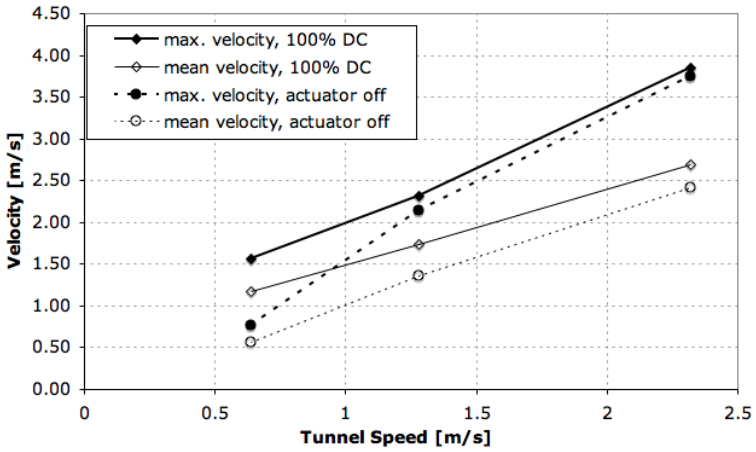

(a) d_i=1.016 cm

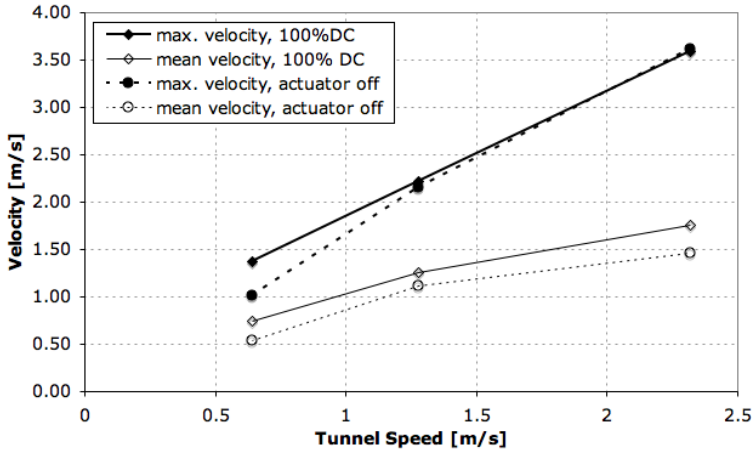

(b) d_i=1.524 cm

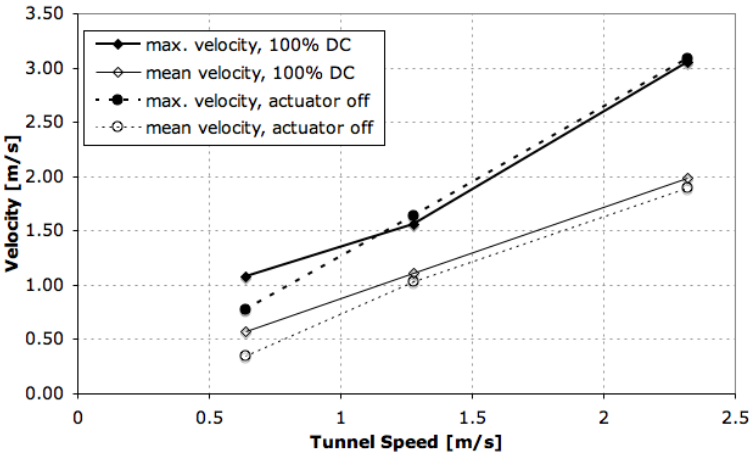

(c) d_i=3.048 cm

Figure 4.24: Variation of maximum and mean velocities with wind tunnel speed.

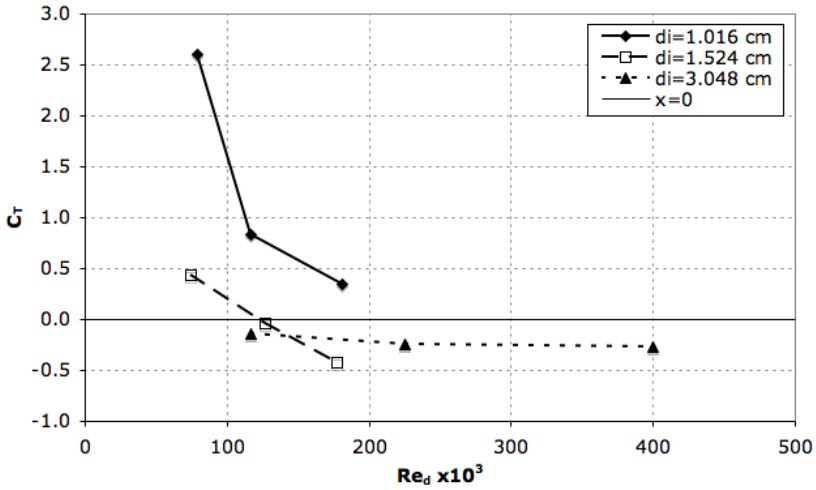

(a) C_T vs. Re_d

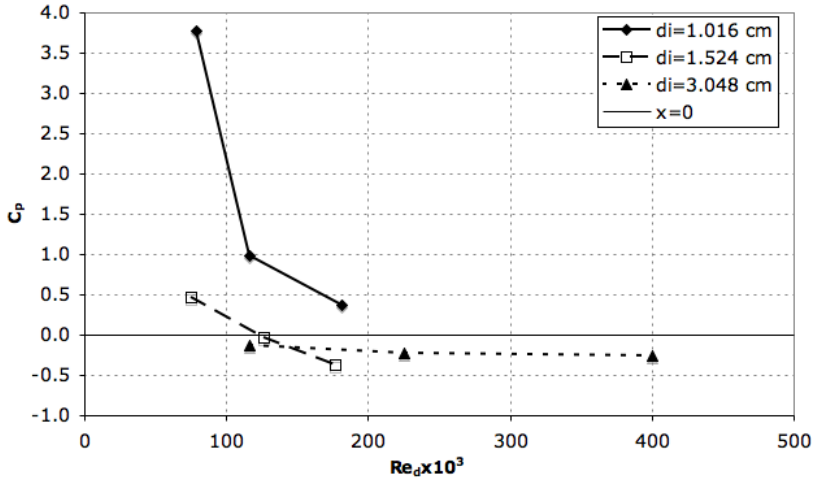

(b) C_P vs. Re_d

Figure 4.25: Variation of thrust and power coefficients with Re for different inner diameter thrusters.

4.2 Thruster Configuration in Staged Arrays

In addition to the runs with the single plasma thrusters, other sets of benchtop tests were carried out to observe the influence of pulsed actuation on staged arrays. This consists of the actuation of two or more plasma thrusters at different phase angles and forcing frequencies. Two sets of inner and exterior electrodes were placed in the three 5.08 cm long tubes of inner diameters d_i=0.635 cm, d_i=1.016 cm, d_i=1.27 cm shown in Fig. 4.26 and tested for the same frequencies of 1 Hz, 2 Hz, 5 Hz, 10 Hz, 100 Hz and 500 Hz with phase angles of 0 and 180 degrees. The duty cycle was kept at 50% and the plasma waveform frequency was changed to 6000 Hz. The same forcing frequencies were then used for a thruster of four sets of electrodes in series at an operating frequency of 5000 Hz and duty cycle of 50% with a phase angle of 180 degrees between consecutive sets to prevent the actuators from arcing and burning out.

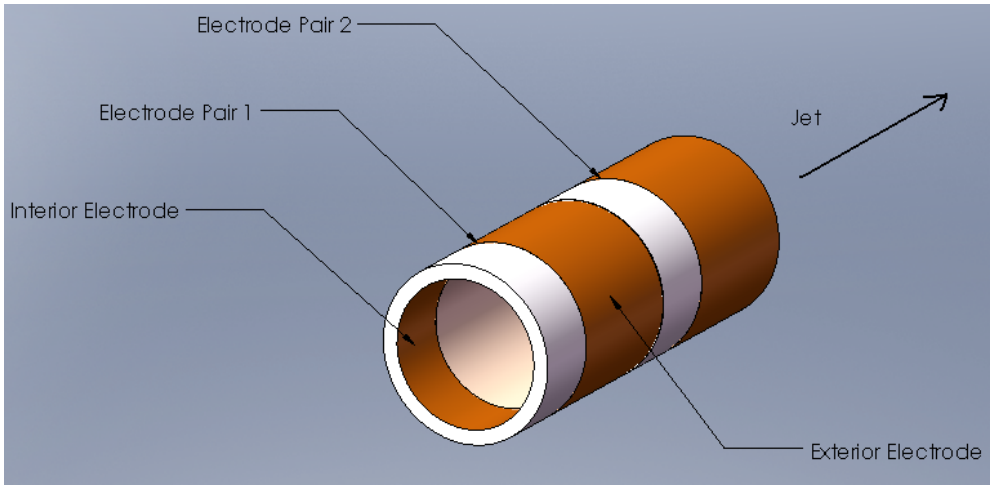

Figure 4.26: Plasma thruster in staged arrays.

The non-dimensional variation of the maximum velocities with forcing frequency for these staged arrays can be seen in Fig. 4.27. These velocities were non-dimensionalized with each of the steady case maximum velocities of the three tubes. Just as in the

single actuator case, the velocities increase up to a certain frequency after which they decrease for each diameter. The important thing to be observed is that the maximum velocities increase by a factor of more than two when two actuators are used in the same tube with 0 degree phase angle. Note that the velocity values for the single actuators are less than the previous tests. This is mainly because of the fact that a plasma frequency of 6000 Hz provides less efficient results than the previously used 5000 Hz and the power input is lower to prevent arcing between the actuators. When actuation is out of phase with a phase angle of 180 degrees, the effect increases even more and results in even higher velocities. After 100 Hz for the largest diameter tube in Fig. 4.27(a), however, pulsing the actuators in phase becomes more effective in increasing the velocity output. This becomes more evident in the smallest diameter tube of d_i=0.635 cm where in Fig. 4.27(a), the velocities are always higher for a phase angle of 0 degrees. The mean velocity distribution follow the same trend as the maximum velocities with only minor differences.

Fig. 4.28 is similar to the previous plots and show the variation of the maximum velocities with forcing frequency for the single and four stage thruster of inner diameter d_i=1.27 cm. The velocities were again non-dimensionalized with the steady case maximum velocity values. It can be seen that pulsing the actuators out of phase is most effective for the 2 Hz case; the difference in the non-dimensional maximum velocity values and thereby the efficiency of the staged arrays decrease as the frequencies are increased above 2 Hz at which the maximum velocities occur for the specific length-to-diameter (ℓ/d_i) ratio of this four stage thruster.

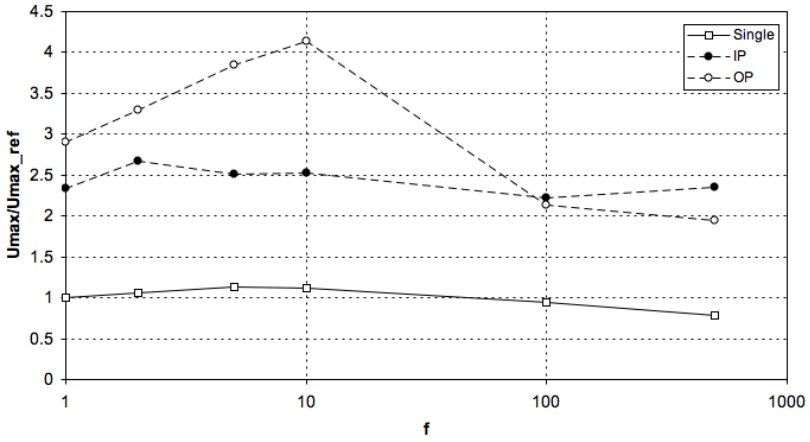

(a) d_i=1.27 cm

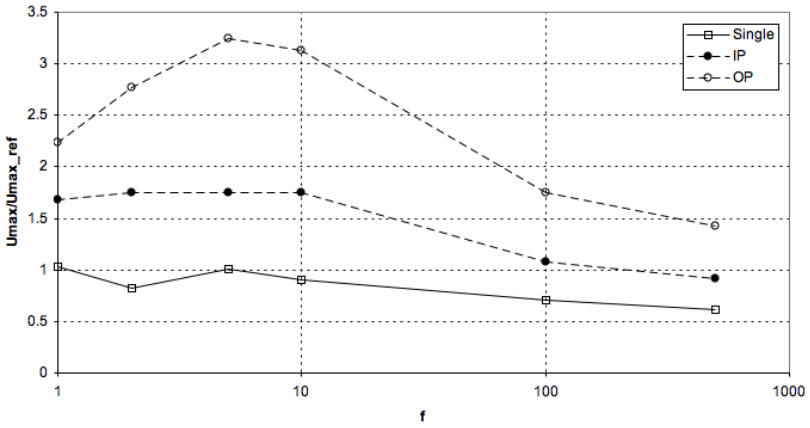

(b) d_i=1.016 cm

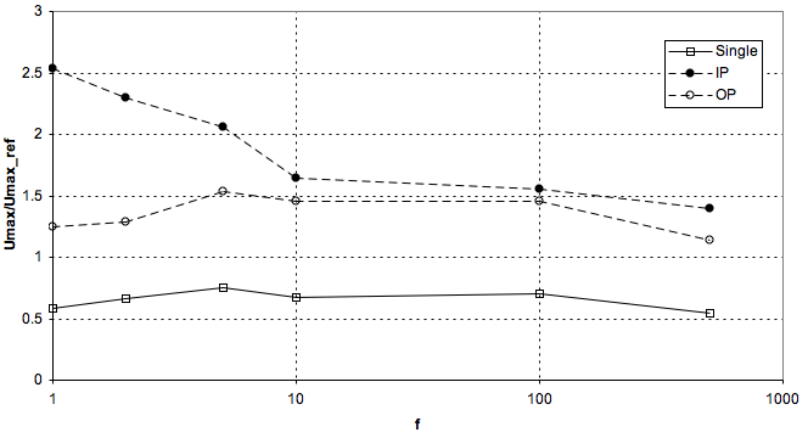

(c) d_i=0.635 cm

Figure 4.27: The effect of staged arrays & pulsed actuation on the maximum velocities for 50% DC.

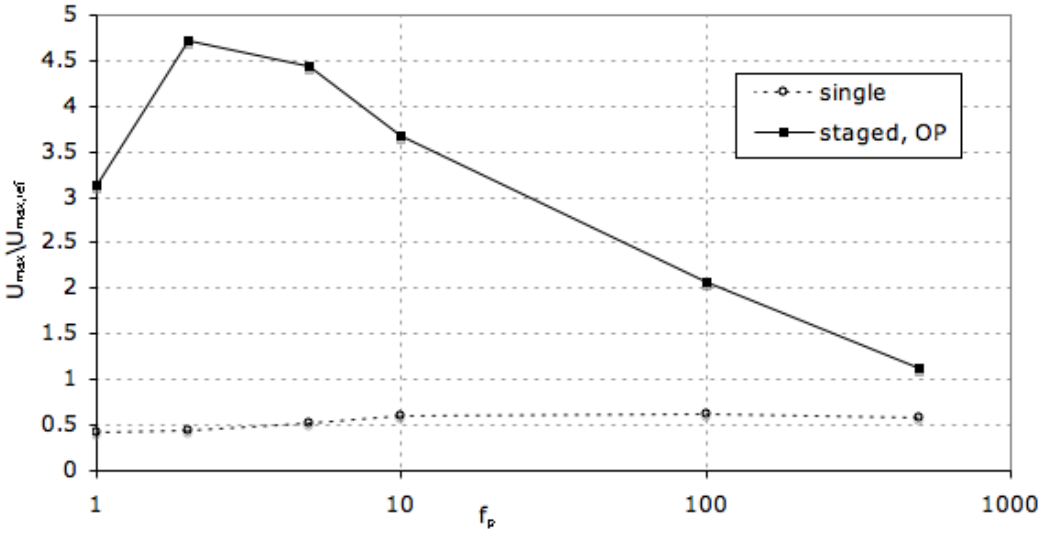

Figure 4.28: Maximum velocity vs. forcing frequency for a single and four stage plasma thruster of d_i=1.27 cm.

4.3 Power Calculations

As mentioned previously, current and voltage measurements for the two setups using different transformers were made with a NK Technologies AC current transducer and a North Star PVM-11 1000:1 high voltage probe. For the cases with a single actuator, the transformer by Electrofluid Systems was used. Current and voltage readings using this circuit board is given in Fig. 4.29. The power can be calculated by substituting the mean values of the current and voltage in to Eq. 4.7

$$P = IV \tag{4.7}$$

The power output obtained by this equation is per unit length, thus as an example, the power provided to the thruster with 1.27 cm inner diameter is calculated as 13.83 W. For the tests using two channels, the CMI 5012 transformers and a QSC RMX 1450 amplifier were used, with current and voltage measurements as seen in Fig. 4.30 and a power output of 11.76 W for a jet vectoring actuator of about 9 cm chord.

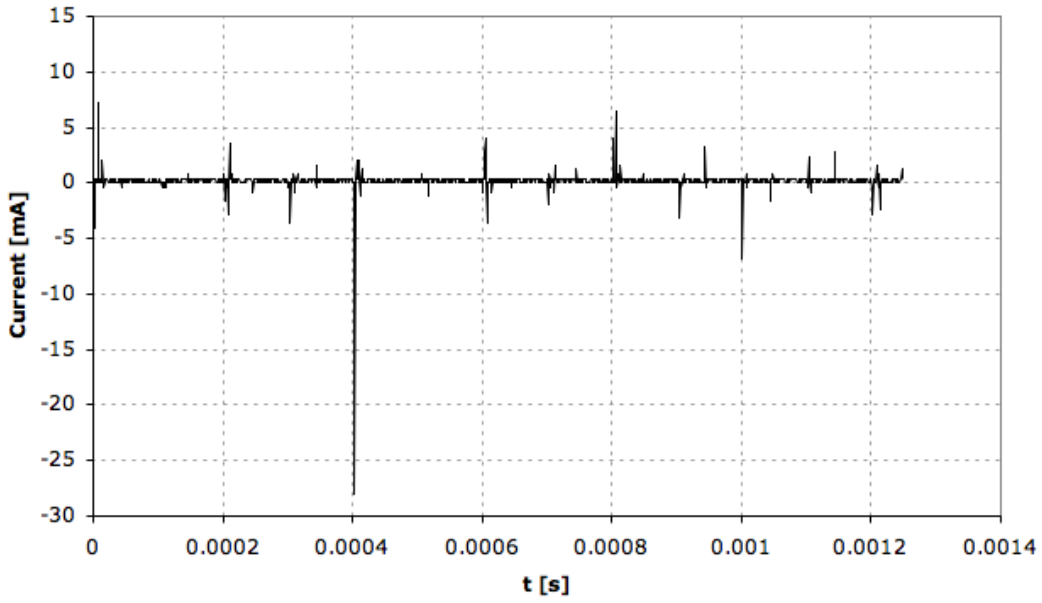

(a) Current vs. time.

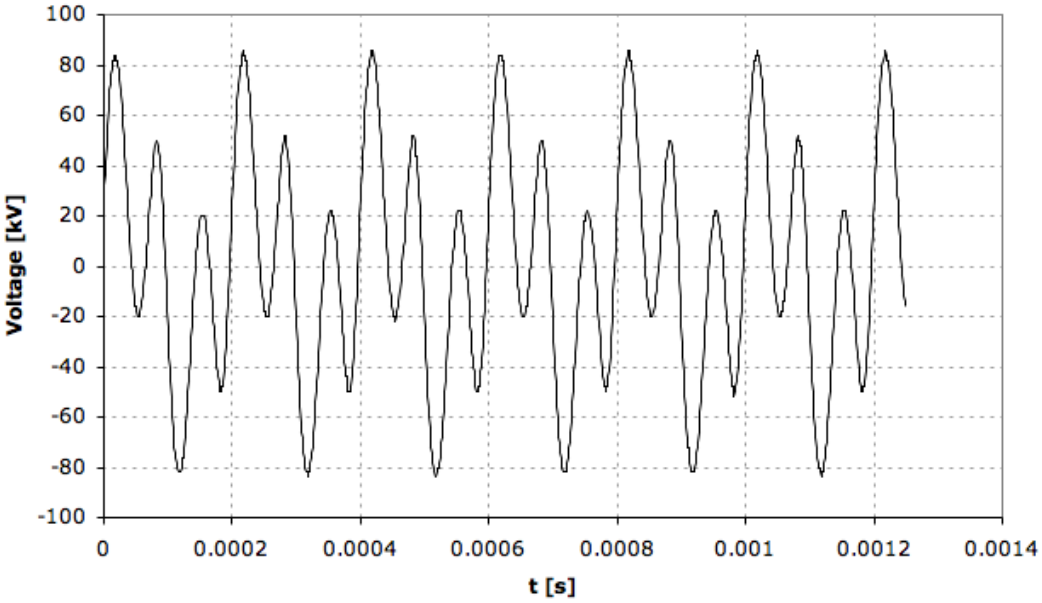

(b) Voltage vs. time.

Figure 4.29: Current and voltage output measurements using the Minipuls2 Circuit Board.

The maximum thrust that has been obtained up to this point using a single pulsed thruster is 4.695 mg, while the power being used is in the range of 10 W-20 W. The maximum velocity of 1.15 m/s obtained yields thrust required values of about 15 mg

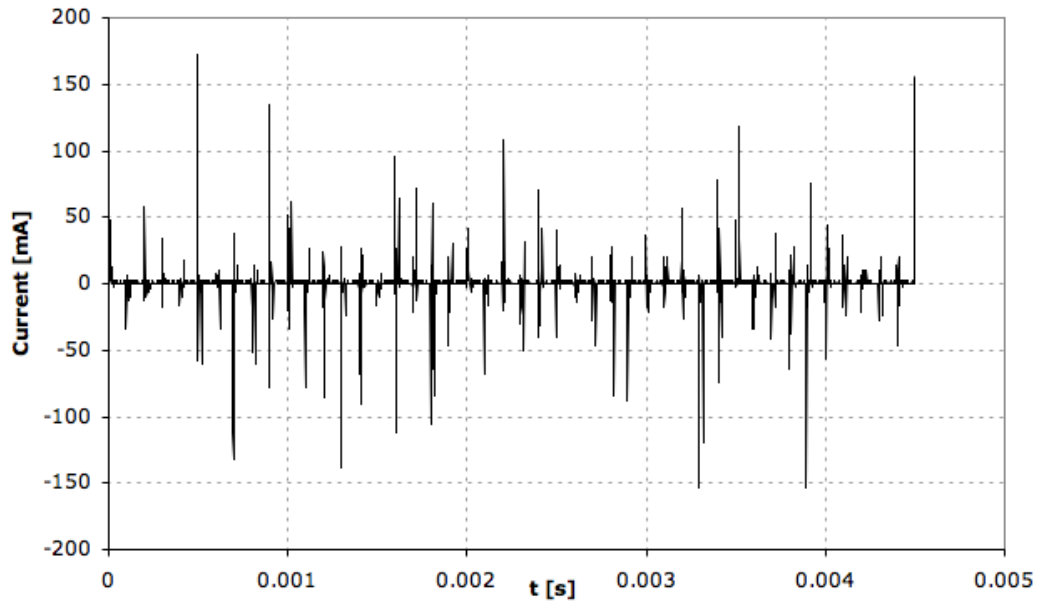

(a) Current vs. time.

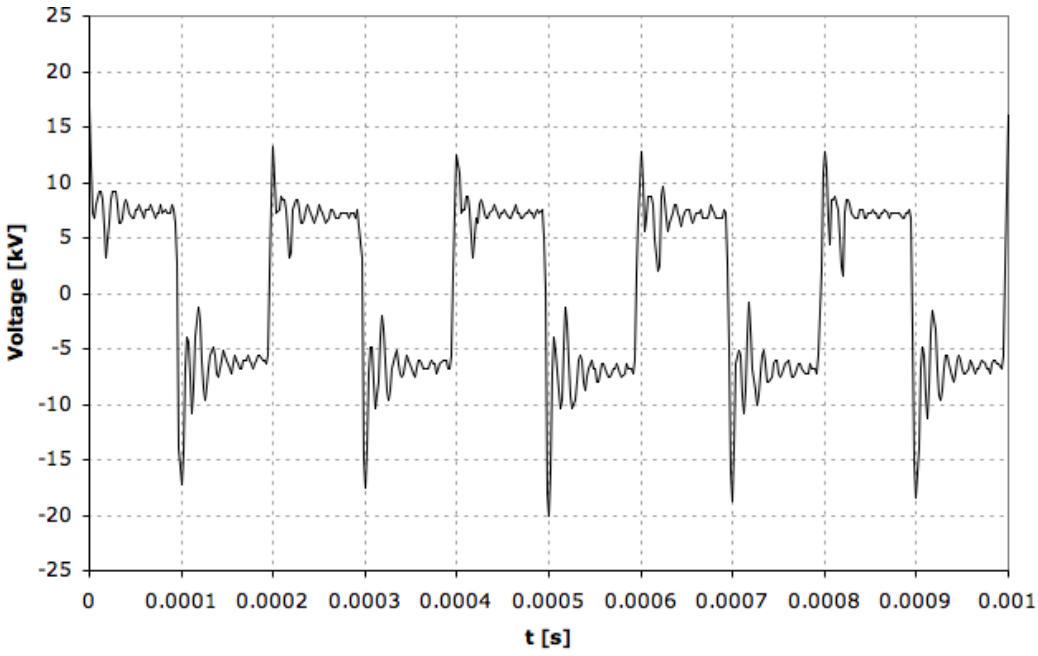

(b) Voltage vs. time.

Figure 4.30: Current and voltage output measurements using the CMI 5012 transformers.

for NAV sized vehicles. This value is found using Eq. 4.8 given below.

$$D = q_\infty S C_{Do} + (\frac{W}{S})^2 \frac{1}{\pi e A R} \frac{S}{q_\infty} \tag{4.8}$$

The wing loading in the above equation can be found from the great flight diagram where it is estimated as a function of velocity. It can be seen that the thrust required decreases with the wing area and loading, thus the actuators are more effective for smaller vehicles. 4.695 mg of thrust available is clearly not enough and the thrust to power ratio is considerably low. Thus, optimizing the velocity and thrust outputs from the actuators should be investigated more thoroughly. The thrust and endurance can be increased by increasing the power provided, which would have a penalty of increasing the battery weight and thus may not even result in an effective increase in the thrust to power ratio. There is also the fact that the measured power input includes losses in the transformer and inductive mismatch. These losses are greatly reduced when the inductance is matched. Consider the actuator efficiency defined as the ratio of power output to input below in Eq. 4.9.[62] The power output is simply the thrust denoted by F multiplied by the velocity output denoted by $\overline{u}_j$ where the thrust is calculated using the mass flow rate and the inner circular area of the thruster while $\overline{u}_i$ is the average plasma induced velocity and d_i is the inner diameter (with r_i as the respective inner radius) of the tube.

$$\eta = \frac{P_o}{P_i} = \frac{F\overline{u}_j}{P_i} = \frac{\dot{m}_o \overline{u}_j \overline{u}_j}{P_i} = \frac{\rho A \overline{u}_j^3}{P_i} = \frac{\rho \frac{\pi}{4} {d_i}^2 \overline{u}_j^3}{P_i} \tag{4.9}$$

Mass conservation is applied to a simple control volume consisting of the tube while assuming zero inlet velocity. Thus, a relation between the average plasma induced and exit velocities is found as

$$\frac{\overline{u}_j}{\overline{u}_i} = 2\left(\frac{h}{r_i}\right)\left(2 - \frac{h}{r_i}\right) \tag{4.10}$$

where h is the actuator influence length inside the tube. The variation of this velocity ratio was plotted in Fig. 4.31, where it could be seen that in going from

an infinitely small inner diameter to larger ones, the jet exit velocity increases and reaches the value of the plasma induced velocity for cases where the influence length is equal to the radius. Substituting this relation between the actuator velocities into the power output, Eq. 4.11 is obtained.

$$P_o = \rho\frac{\pi}{4}{d_i}^2\overline{u_j}^3 = \rho\frac{\pi}{4}{d_i}^2\left[2\overline{u_i}\left(\frac{h}{r_i}\right)\left(2-\frac{h}{r_i}\right)\right]^3 \tag{4.11}$$

Assuming the power input is constant with actuator length,

$$P_i \propto c \propto d_i \rightarrow P_i = C\pi d_i \tag{4.12}$$

where c is the circumference of the actuator and C is a constant with units of [W/m]. The efficiency of the actuator then becomes

$$\eta = \frac{\rho\frac{\pi}{4}{d_i}^2\left[2\overline{u_i}\left(\frac{h}{r_i}\right)\left(2-\frac{h}{r_i}\right)\right]^3}{C\pi d_i} = \rho C'{\overline{u}_i}^3\frac{h^3}{{d_i}^2}\left(1-\frac{h}{d_i}\right)^3 \tag{4.13}$$

where the induced velocity and influence length are fixed for a given actuator. Taking $h = 1mm$ and the constant C' as the inverse of the measured power value per unit inner diameter, a non-dimensional efficiency was plotted in Fig. 4.32. The inner diameter is non-dimensionalized by the influence length and the efficiency by its maximum value. It can be seen that the efficiency increases with the thruster inner diameter up to some critical value after which it starts decreasing. Note that the maximum efficiency occurs around a (d_i/h) ratio of 2.5, which corresponds to an inner diameter of 0.25 cm. The thrusters that have been used can be seen in the plot and range from d_i=0.635 cm to d_i=3.048 cm, so it is obvious that smaller inner diameters need to be employed in order to obtain the maximum efficiency.

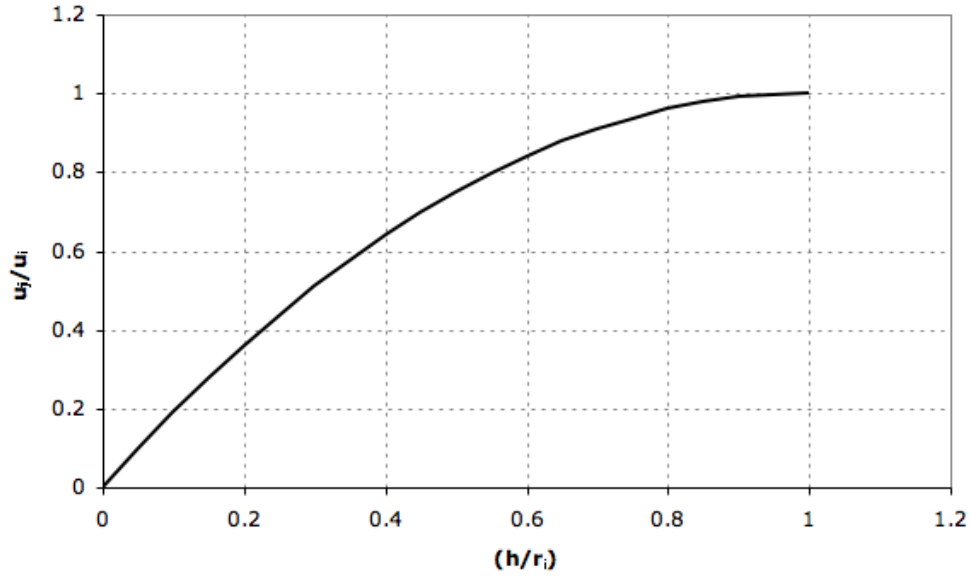

Figure 4.31: Variation of the ratio of average plasma induced and exit velocities with $\left(\frac{h}{r_i}\right)$.

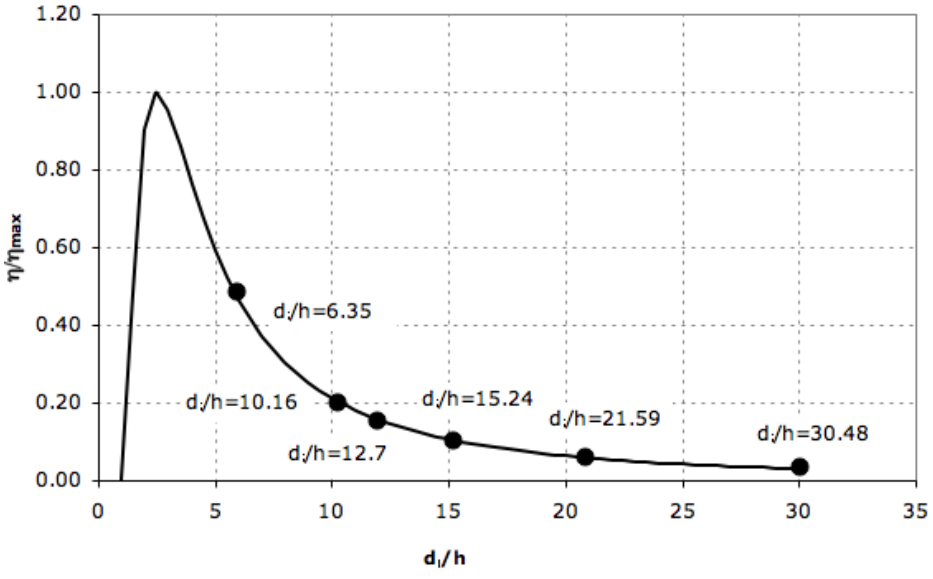

Figure 4.32: Variation of the efficiency of the thrusters with inner diameter.

CHAPTER 5

Jet Vectoring Plasma Actuator

Similar to the annular thruster configuration, both average and transient velocity measurements for the jet vectoring plasma actuator shown in Fig. 1.4 were acquired with the PIV system. Experiments were conducted with varying parameters such as the duty cycle and wind tunnel speed to observe their effect on the induced flow field where the actuator acts as a vortex generator jet. Unlike the plasma thrusters, no quiescent measurements were made and the duty cycle was the only input parameter varied throughout the tests. This is mainly due to the fact that changing the duty cycle has a greater sensitivity to the angle change and allows less power input. Extensive information on the parametric study for jet vectoring actuators in quiescent flow can be found in Bolitho.[54]

Flow visualization was once again employed to observe the detailed structure of the induced flow. A smoke-wire was placed at the entrance of the tunnel test section to seed the flow. The actuator in Fig. 5.1 is built on the alumina plates and pulsed at 250 Hz while the duty cycles are at 50% and 30% for the left and right channels, respectively. It can be seen from the streamlines close to the actuator surface in Fig. 5.1(a) that similar to a linear actuator, the flow is being pulled in and pushed back out. However, note that in Fig. 5.1(b), the streamlines are not straight, but tend to lean towards the left strip. This results from the fact that the left side is pulsed at a higher duty cycle of 50%, causing the plasma to be stronger and to pull the flow to itself. The behavior of the flow after being directed inwards can be seen more clearly in Fig. 5.2, where both channels are pulsed at 50% DC. The streamlines

closer to the plate surface are directed in and out around the leading edge while the upper streamlines are directed inwards at a further downstream distance. This causes braiding of the streamlines and this corkscrew structure propagates downstream with time as seen in Fig. 5.2(a) through (c).

For the first set of experiments, the jet vectoring actuator on the Alumina plate was employed at constant plasma and modulation frequencies of 9000 Hz and 250 Hz, respectively, with a phase angle of 180 degrees between the two channels and tunnel speed of 1.28 m/s. The forcing frequency of 250 Hz was chosen regarding the fact that it is above the critical frequency required to produce a jet in quiescent flow.[54] This is also verified by hotwire measurements obtained at the mid chord location 1.27 cm away from the actuator in the cross stream direction using different forcing frequencies. It could be seen in Fig. 5.3(a) that the velocities for the 100 Hz case are significantly lower than the others. As the frequency is increased above the critical forcing frequency, the increase in the mean velocity is reduced while the amount of deviation from the mean is larger due to the turbulent fluctuations, shown in Fig. 5.3(b). The duty cycles of the channels were varied to observe the effect on the flow field; one side was kept at a 50% DC while the other was varied from 0% to 50%. Then, the opposite case was observed where the initially constant duty cycle actuator was varied from 50% to 0% and the other was kept constant at 50%. Fig. 5.4 shows the absolute maximum vorticity values for each of these cases. It can be seen that for the cases of 0%/50% and 50%/0% duty cycles, which are simply linear actuators without vectoring, there is a significant amount of drop in the maximum vorticity. This could also be observed for the cases with a 40%, 30% and 20% DC for one side and 50% DC on the other. This is due to the fact that the plasma strengths on the two sides are not equal. For the first five vectoring cases, where the left side is kept at 50% DC, the vorticity values are significantly higher, implying that this side produces stronger plasma. The 50%/50% case should normally yield a lower vorticity if the

plasma strengths were equal since both sides would tend to cancel each other out. This is seen in the 40%/50% case where the vorticity reaches a minimum, changes sign and starts to increase again, which is expected with increasing discrepancy between the duty cycles of the two channels. These values would be as high as the case with the left side at 50% DC but since there is an asymmetry, the vorticity is dominated by the left side and is kept at lower values.

Even though it is not investigated in the experiments here, the effect of the yaw angle on the vortex strength is also significant and should be mentioned.[54] When there exists a yaw angle between the freestream and the actuators, the vortex from the boundary layer over the plate tends to increase the strength of the vortex produced by one side while decreasing the one created by the other side. This is illustrated in Fig. 5.5 where it could be seen that for the case with the yaw angle, ω_z adds to the cross stream component of the vortex created by the left side, ω_1.

The circulation distribution is also plotted against the radius in Fig. 5.6 for all cases and it can be seen that the higher the strength of the vortex created is, the larger the circulation values are for that case. As expected, the circulation values start increasing at the outer radius of the vortex, reach a maximum at the center and start decreasing again. Note that after the 40%/50% DC case where the vortex changes direction, the circulation values are negative. It is important to note that these circulation values are calculated using velocity, given by

$$\Gamma = \int \vec{V} \cdot \vec{dl}$$

which is better than calculating with vorticity that tends to under-predict the actual circulation values, given by

$$\Gamma = \int \vec{\omega} \cdot \vec{dA}$$

The difference between the two calculations is illustrated in Fig. 5.7 for the case with the left channel at 50% DC and the right at 0% DC.

In order to observe and track the position of the vortices for these cases, a hodograph was used where the coordinates of the vortex centers were plotted relative to the actuator, shown in Fig. 5.8. Note that the 0%/50% and 50%/0% cases are on opposite sides of the actuator since they are positioned in the direction of the near wall jet that is induced with a linear actuator. The near wall jet also explains the fact that these two cases yield the smallest vertical distance from the actuator. As the right side is varied and the left side is kept at 50% DC, it could be seen on the right side of the figure that as a result of vectoring, the jet and hence the vortex center starts moving away from the wall, following the direction of the jet. The same phenomena occurs on the left, but after the 10%/50% case, as just mentioned, the asymmetry in plasma strengths causes a certain randomness in the position of the vortex centers. If it were not for the asymmetry, the hodograph would appear as shown in Fig. 5.9. Streamlines and vorticity contours obtained from the PIV measurements are also shown in Fig. 5.10 - Fig. 5.20. As mentioned previously, the motion of the vortex can be observed in going from the 50%/0% case to the 0%/50% case; 180 degrees of vectoring from a near wall jet on the left side of the actuator to a near wall jet on the right side. The changes in the locations of the vortex is not as clear as in the hodograph since the range of the cross stream x-axis was varied to capture all of the vortex for each of the cases while the vertical position of the plate was also changed once during the experiments. The change in the sign of the the vorticity can also be observed in cases after the 40%/50% DC case in Fig. 5.16. This would be expected to be seen after the case where both channels are operated at 50% DC if the two sides were symmetric. For most of the cases with the right side kept at 50% DC, the asymmetry is very apparent where since the left side is stronger, the vortex resulting from actuation is visible along with the vortex of the right side rather than showing up as a single vortex on the right.

A second set of tests were conducted to observe the evolution of the vortex struc-

tures that form upon actuation. The jet vectoring actuator was pulsed once more at the same parameters; plasma and modulation frequencies of 9000 Hz and 250 Hz, 180 degrees of phase angle and a tunnel speed of 1.28 m/s. PIV data was acquired along the streamwise direction, at 0%, 25% , 50% , 75% and 100% chord locations. Fig. 5.21 shows the case for both channels pulsed at 50% DC where Fig. 5.21(a) is the variation of the maximum vorticity values with chordwise position. It is clear that the vortex is strongest around the mid-chord location (mid-chord for this case) and weakest at the leading edge. The circulation variation with radius is also plotted in Fig. 5.22 where it can be seen that as going downstream, circulation is added continuously. Note that, however, the bulk of it is introduced around the mid-chord region, also seen in Fig. 5.23, where the strongest vortex is observed. This is because further downstream, the vortex generated by the actuator is subsumed in the boundary layer and is unable to add to the strength of the initial vortex advecting downstream and moving away from the plate. Thus, the increase in the circulation is limited after mid-chord and separate vortices will be formed as in Fig. 5.24, meaning that there is no need for a large streamwise length for these actuators. The hodograph in Fig. 5.21(b) illustrates the motion of the vortex along the chord. Looking back at Fig. 5.8, it can be seen that the 50%/50% case at mid-chord location yields a vortex to the left of the actuator, which is consistent with these locations to the left of the actuator. Note that this motion resembles that of the one previously seen in the flow visualizations in Fig. 5.1, resulting in the braiding of the streamlines as they move downstream. Similar to the previous experiments, streamlines were plotted to show these effects on the location of the vortex illustrated in the hodograph. Observe in Fig. 5.25 that the vortex is barely visible and low in strength at the leading edge, after which it starts to grow in size and becomes the largest at the trailing edge with the highest strength at the mid-chord location. As previously explained, the vortex starts moving away from the wall and the plasma actuator is incapable of increasing

the strength of the detached vortex. The increasing size can also be observed in the flow visualizations with the growing boundary layer along the chord. A 3-D view of the field is also presented in Fig. 5.26 where the evolution of the vortex structure could be seen more clearly.

Similarly, for the case with the left side held at 10% DC and the right at 50% DC the maximum vorticity variation and the vortex locations were plotted as seen in Fig. 5.27(a) and (b). Note that the peak value of the maximum vorticity occurs around mid-chord again (at the 25% chord location this time), with a similar circulation distribution in Fig. 5.28 to the previous case, again implying that the circulation is mainly added in these regions, also illustrated in Fig. 5.29 while the hodograph is very clear in terms of the braiding motion just explained for the previous case. The 2-D plots of streamlines in Fig. 5.30 and the 3-D view in Fig. 5.31 illustrate this motion and the growth of the vortex along the streamwise direction. Thus, for these tests in the streamwise direction, it can be said that the motion and evolution of the vortex along the chord is basically the same regardless of the duty cycle of the two channels.

For the last set of runs, the jet vectoring actuator was placed in the chordwise direction on a NACA 0012 airfoil with a chord of 15.24 cm, span of 30.48 cm and an angle of attack of 10 degrees, as seen in Fig. 5.32. Instead of the Alumina, the Teflon plate of 0.16 cm thickness was used as the dielectric in order to have the flexibility to embed the actuator on the wing. Streamwise PIV measurements were taken for the region shown in Fig. 5.33 for two different tunnel speeds of 0.62 m/s and 1.28 m/s with the same forcing frequency of 250 Hz, phase angle of 180 degrees and plasma frequency of 9000 Hz as in the previous tests. Fig. 5.34 illustrates the effect of the actuator on separation and stall control at the lower tunnel speed using reverse flow probability. The red color represents flow that is opposite the direction of freestream while the blue is flow in the freestream direction. The colors in between are the cases where some of the flow is upstream and the rest is downstream, yellow for example,

means half of the velocity vectors are in the freestream direction while the other half is in the opposite direction. It can be seen that in Fig. 5.34(a) where the actuator is turned off, the separation region is very apparent while for any of the other three cases in Fig. 5.34(b), (c) and (d), the actuator acts as a vortex generator, energizes the boundary layer and suppresses separation. It could also be observed that the any of the two vectoring cases are more effective in controlling the separation than the linear case, while the 50%/50% DC case yields better control than the 30%/50% DC, resulting from the fact that the vortex in the previous case is stronger than the latter. For the higher speed of 1.28 m/s, however, it can be observed in Fig. 5.35 that the 0%/50% DC case is actually more efficient than the vectoring cases while the 50%/50% DC case still yields better results than the 30%/50% DC case, which is also consistent with the maximum vorticity values in Fig. 5.4. The effectiveness of all the actuators decrease with increasing tunnel speed, although it is possible that the upstream motion observed in the RFP plots could be the vortex generated by the actuators mounted on the airfoil. Although it has not been done in this case, boundary layer profiles would be useful to verify whether there is separation or not for these higher speeds with the actuators on.

Figure 5.1: 3-D smokewire flow visualization in freestream for the jet vectoring plasma actuator.

(a) t=0.93 s

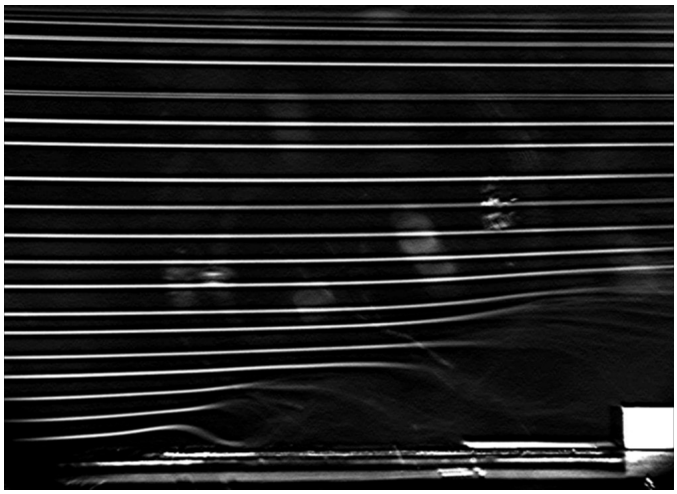

(b) t=1 s

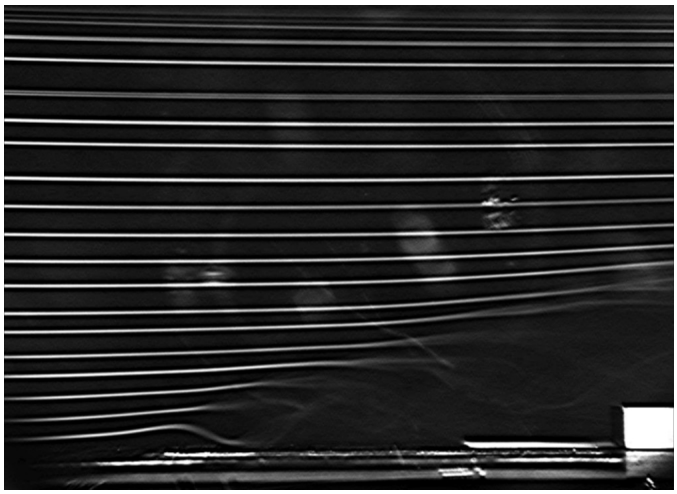

(c) t=1.07 s

Figure 5.2: 2-D smokewire flow visualization in freestream for the jet vectoring actuator.

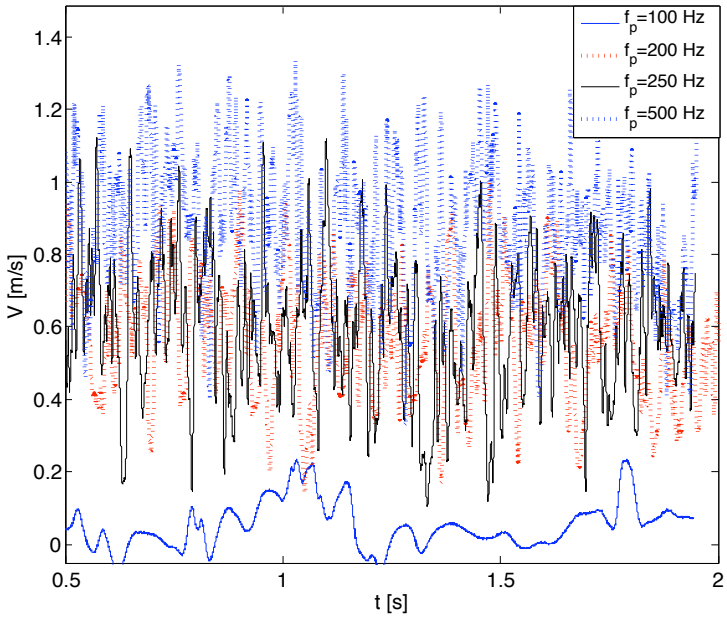

(a) Velocity vs. time.

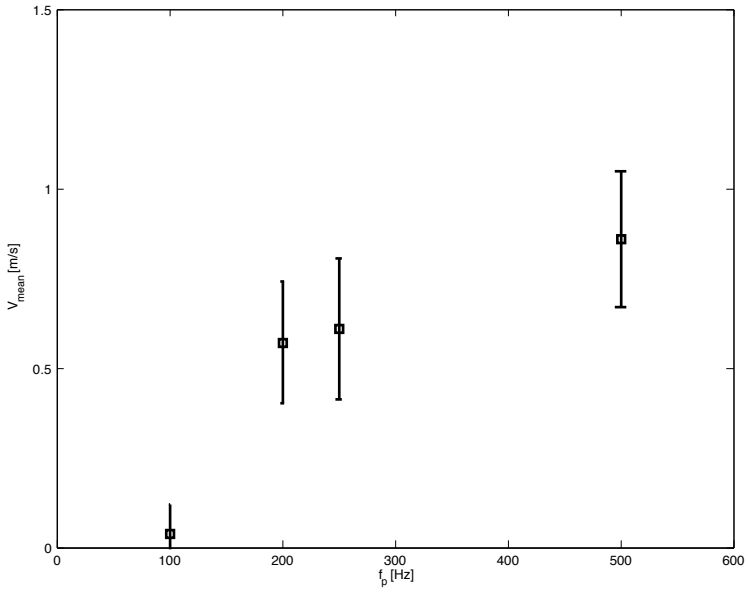

(b) Velocity vs. forcing frequency.

Figure 5.3: Hotwire measurements for the jet vectoring actuator with both sides at 50% DC.

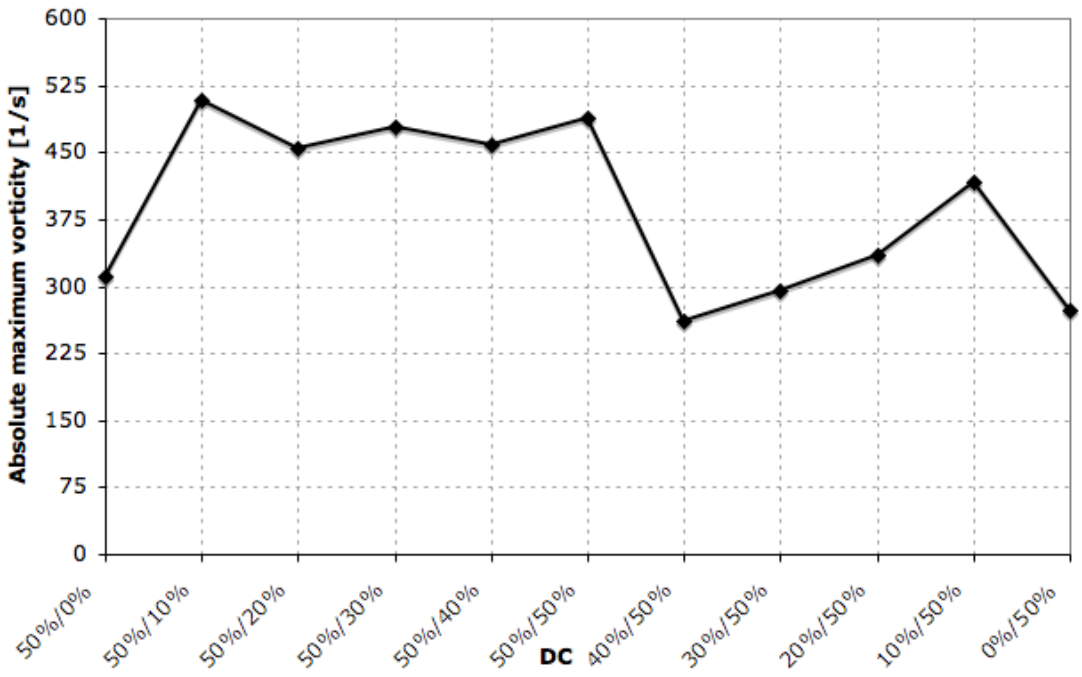

Figure 5.4: Variation of absolute maximum vorticity with changing duty cycles in both channels.

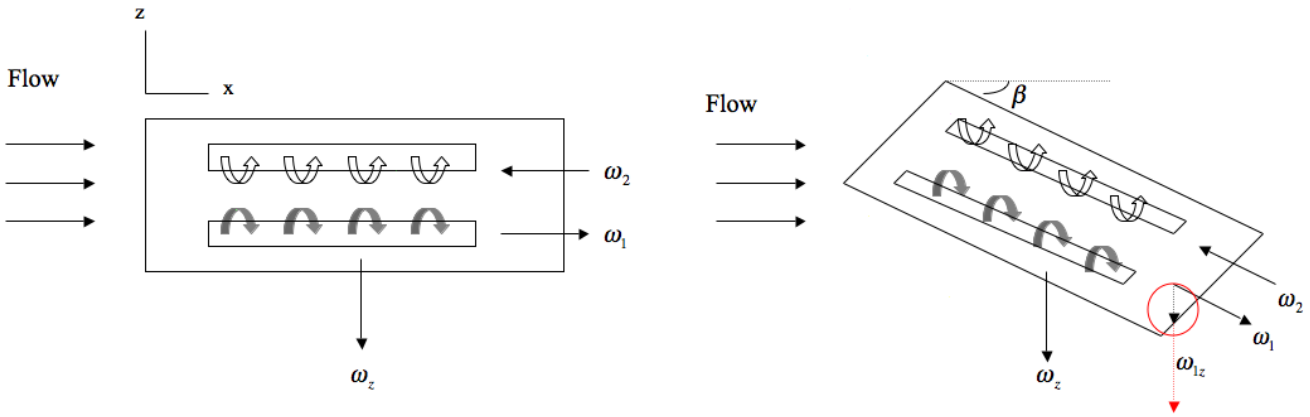

Figure 5.5: Effect of yaw angle on vortex strength.

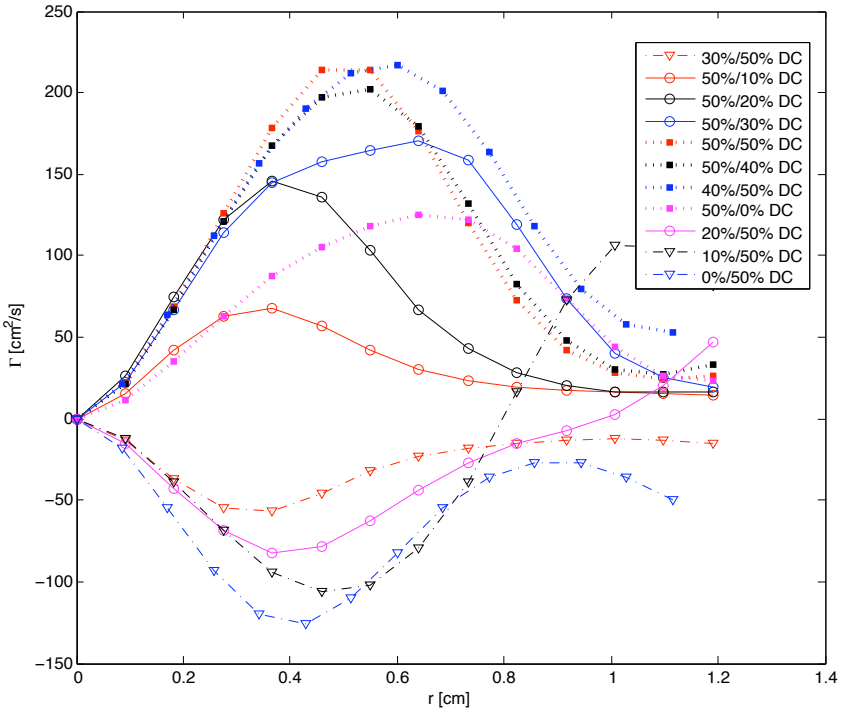

Figure 5.6: Circulation vs. radius for varying duty cycles in both channels.

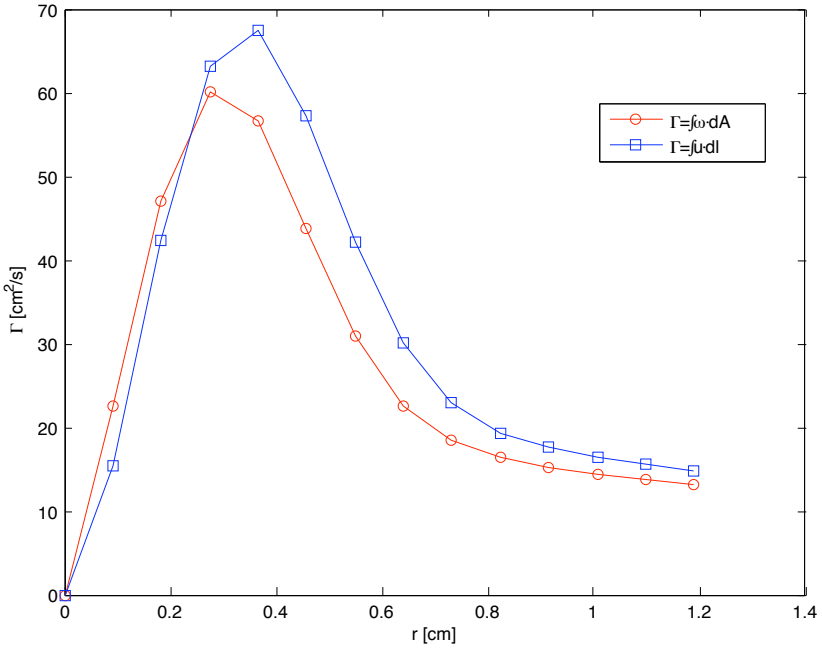

Figure 5.7: Circulation calculation using velocity vs. vorticity for the 50%/0% DC case.

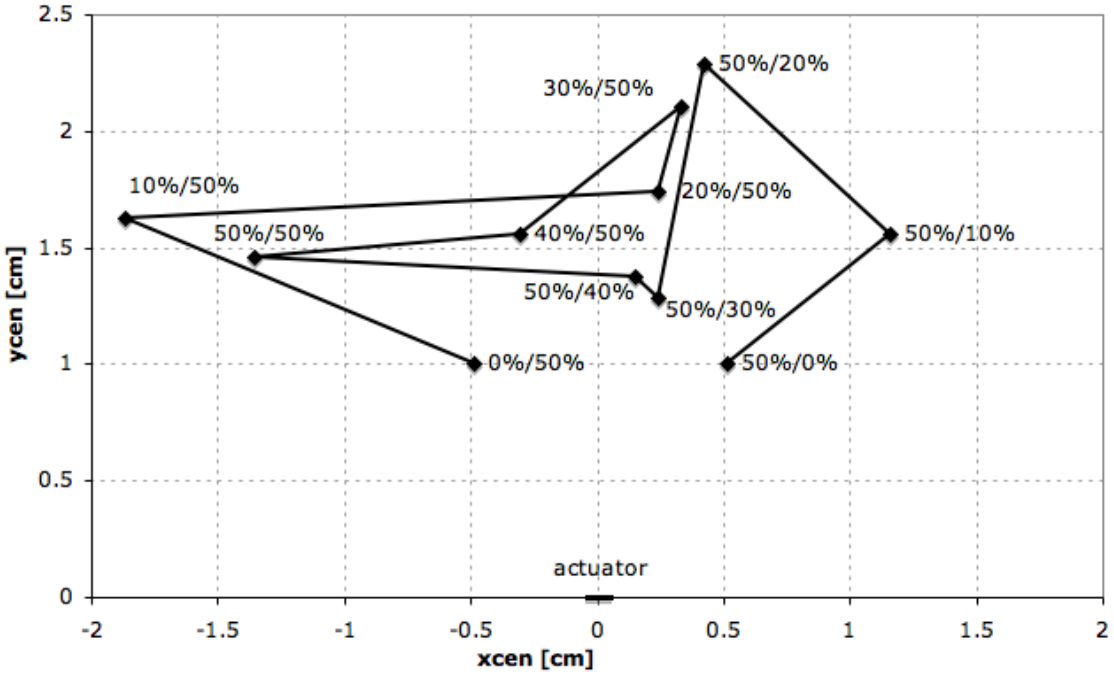

Figure 5.8: Hodograph for jet vectoring actuator with varying duty cycles in both channels.

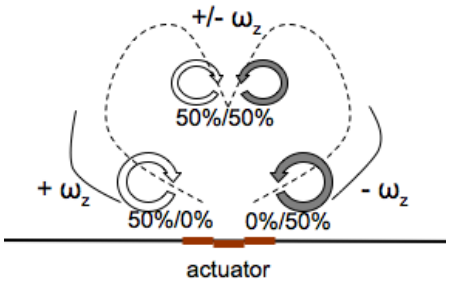

Figure 5.9: Expected hodograph for jet vectoring actuator with equal plasma strength on both sides.

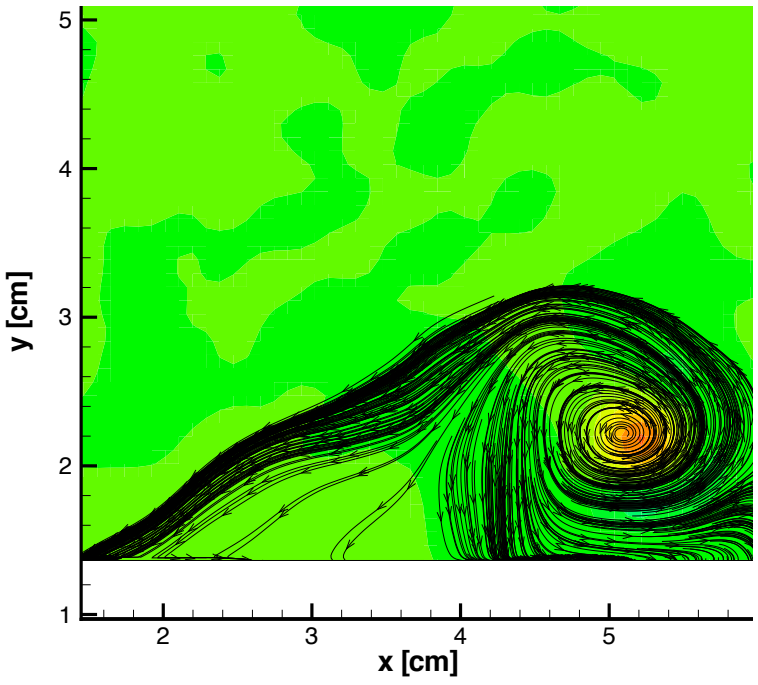

Figure 5.10: Streamlines and vorticity contours for jet vectoring with 50%/0% DC for the left and right channels, respectively.

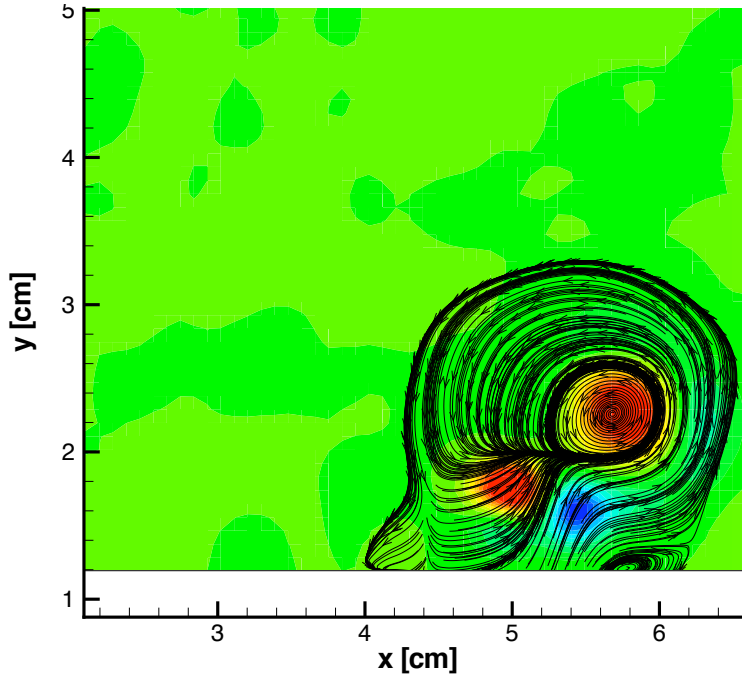

Figure 5.11: Streamlines and vorticity contours for jet vectoring with 50%/10% DC for the left and right channels, respectively.

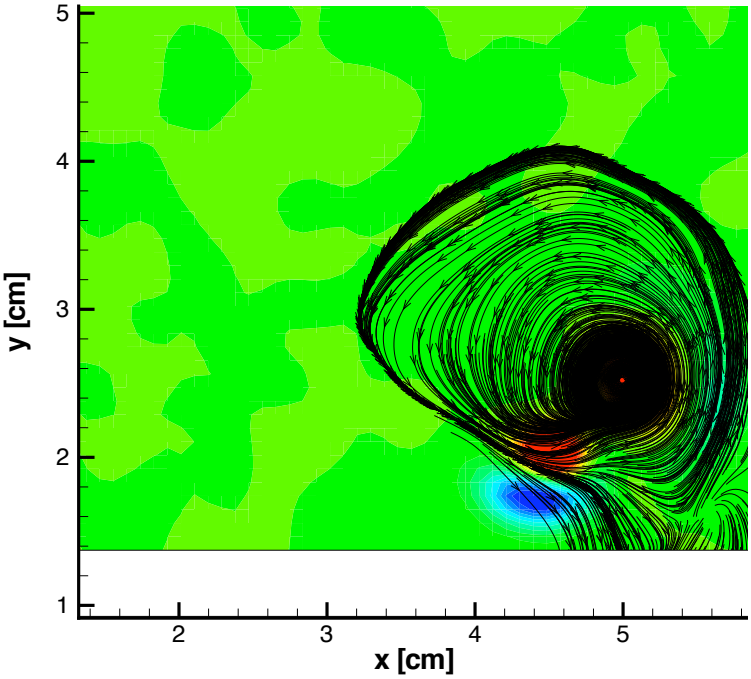

Figure 5.12: Streamlines and vorticity contours for jet vectoring with 50%/20% DC for the left and right channels, respectively.

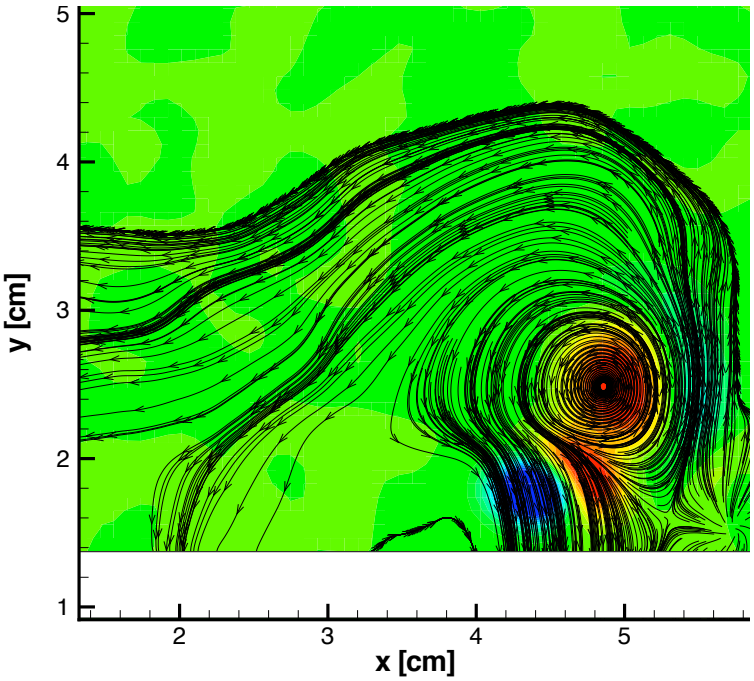

Figure 5.13: Streamlines and vorticity contours for jet vectoring with 50%/30% DC for the left and right channels, respectively.

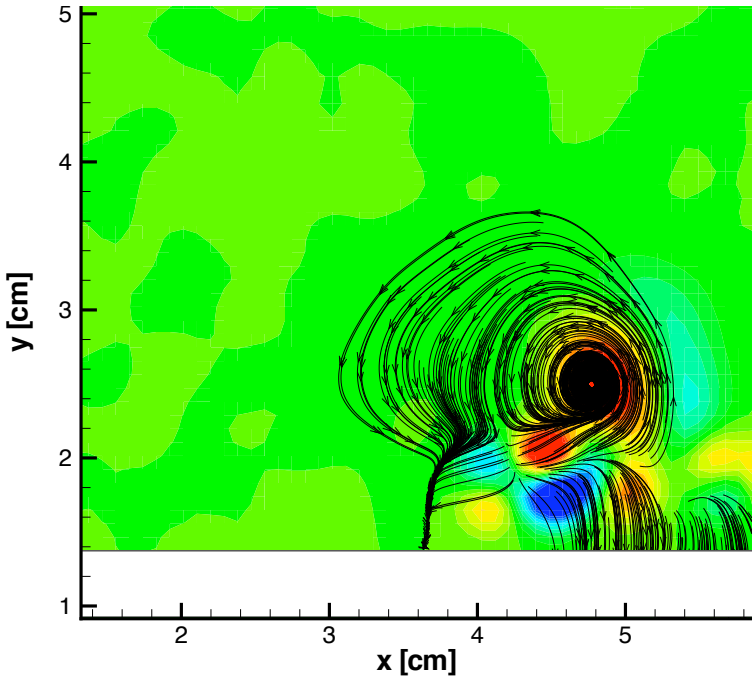

Figure 5.14: Streamlines and vorticity contours for jet vectoring with 50%/40% DC for the left and right channels, respectively.

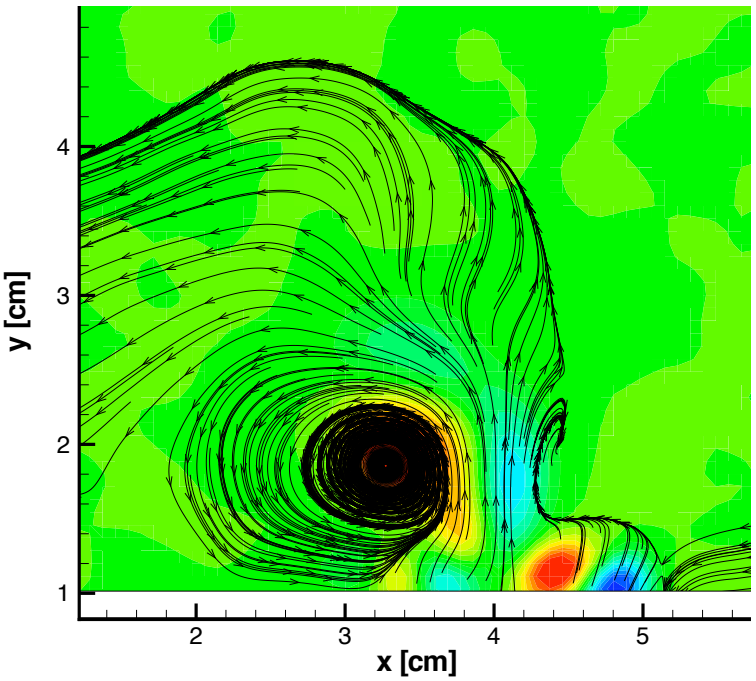

Figure 5.15: Streamlines and vorticity contours for jet vectoring with 50%/50% DC for the left and right channels, respectively.

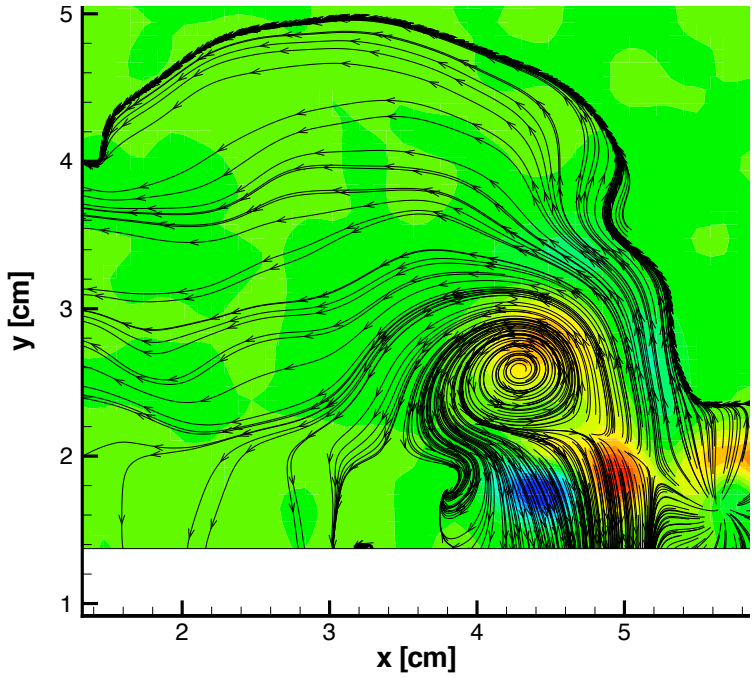

Figure 5.16: Streamlines and vorticity contours for jet vectoring with 40%/50% DC for the left and right channels, respectively.

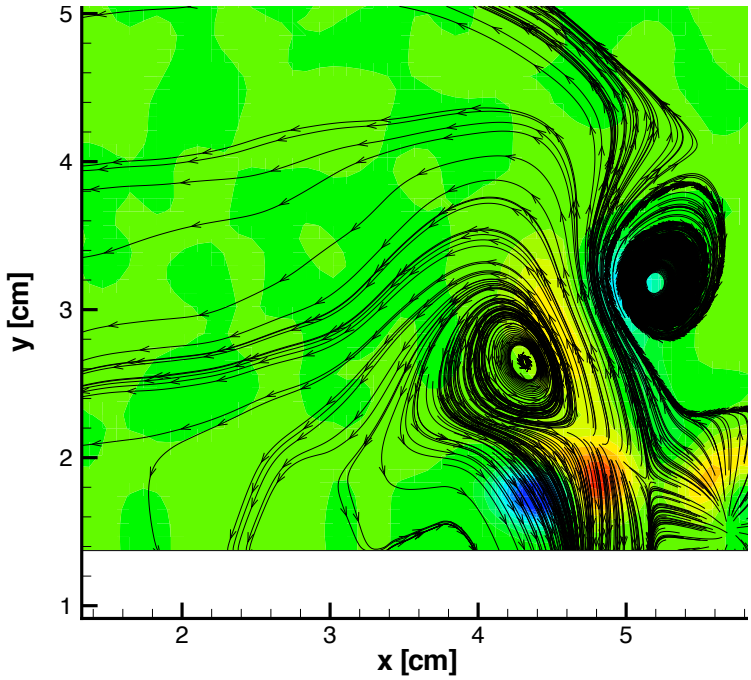

Figure 5.17: Streamlines and vorticity contours for jet vectoring with 30%/50% DC for the left and right channels, respectively.

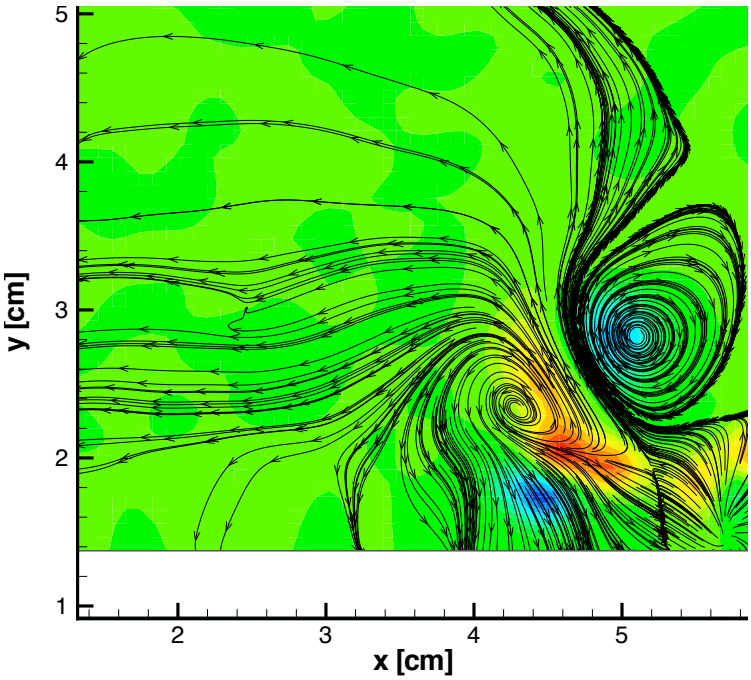

Figure 5.18: Streamlines and vorticity contours for jet vectoring with 20%/50% DC for the left and right channels, respectively.

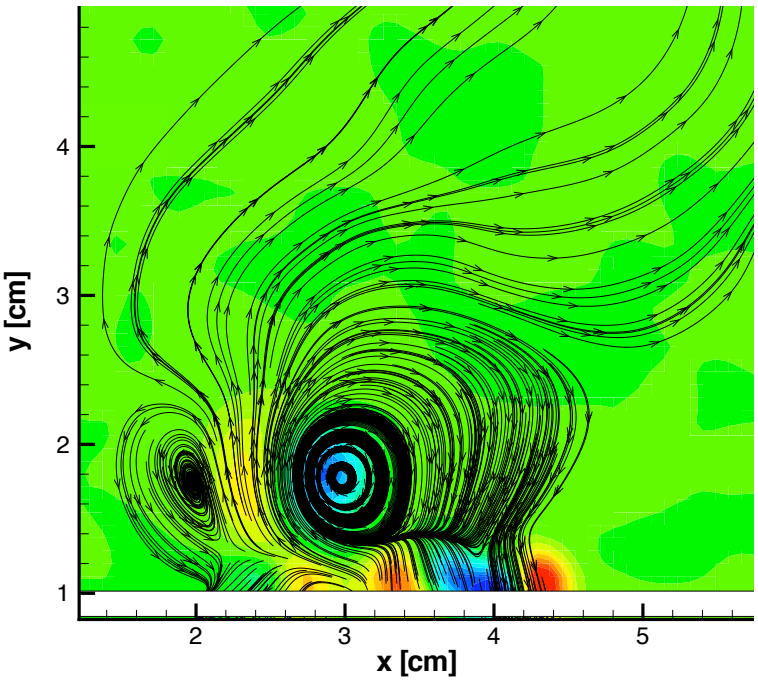

Figure 5.19: Streamlines and vorticity contours for jet vectoring with 10%/50% DC for the left and right channels, respectively.

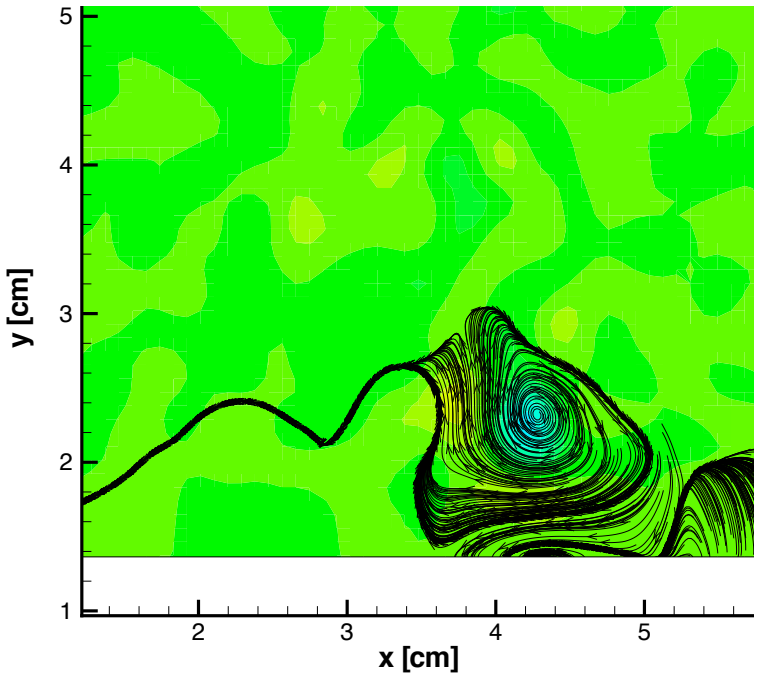

Figure 5.20: Streamlines and vorticity contours for jet vectoring with 0%/50% DC for the left and right channels, respectively.

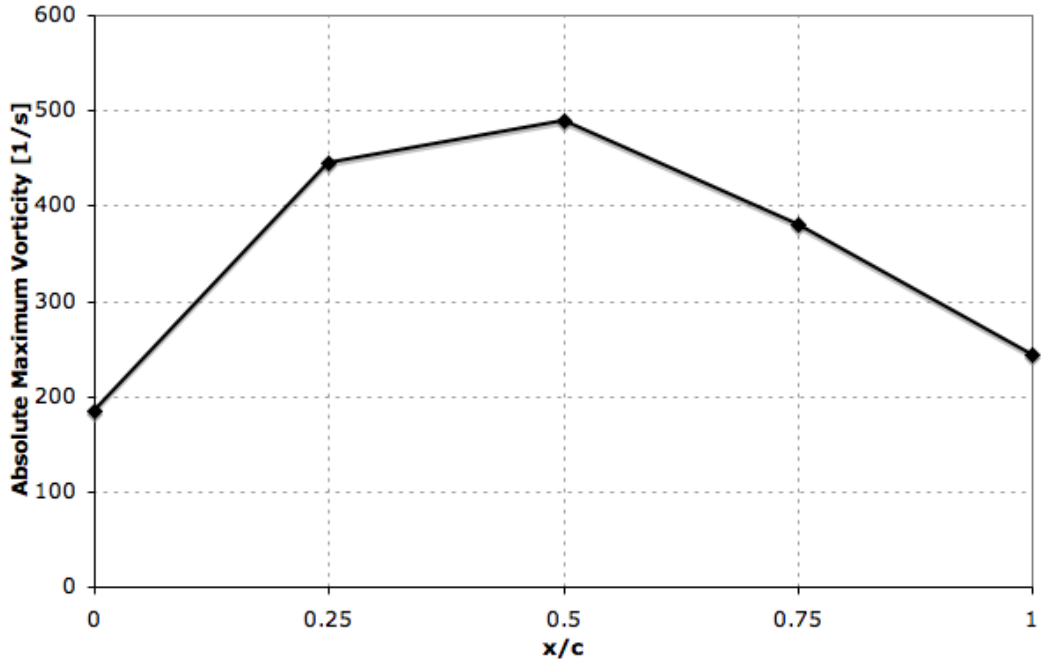

(a) Absolute maximum vorticity vs. chord location.

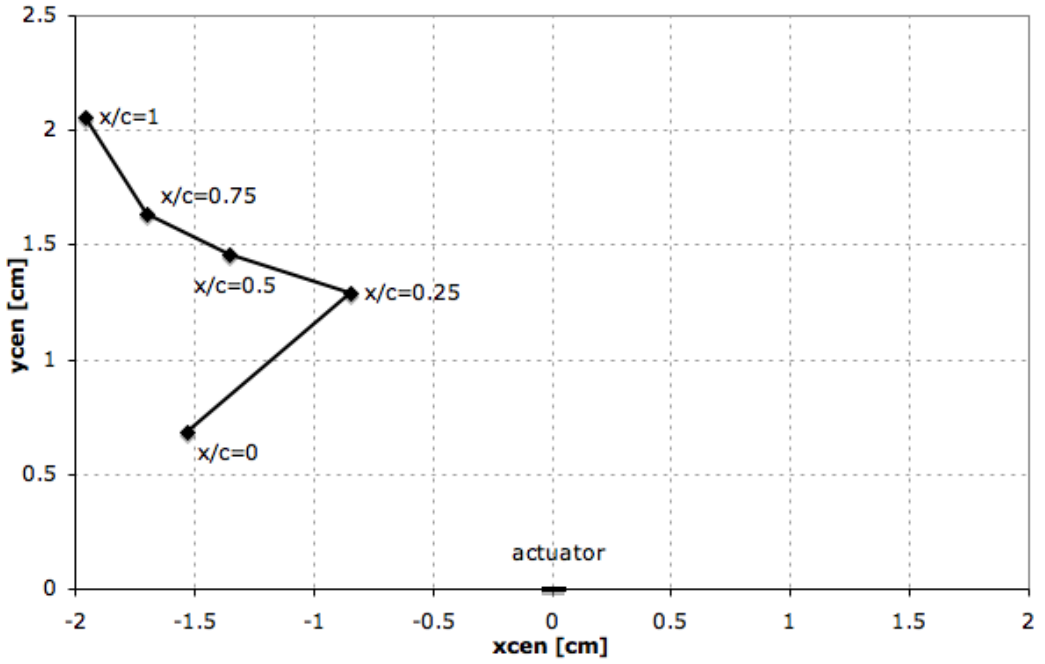

(b) x vs. y-coordinates of vortex centers.

Figure 5.21: Variation of vortex strength and position with chord location for both channels at 50% DC.

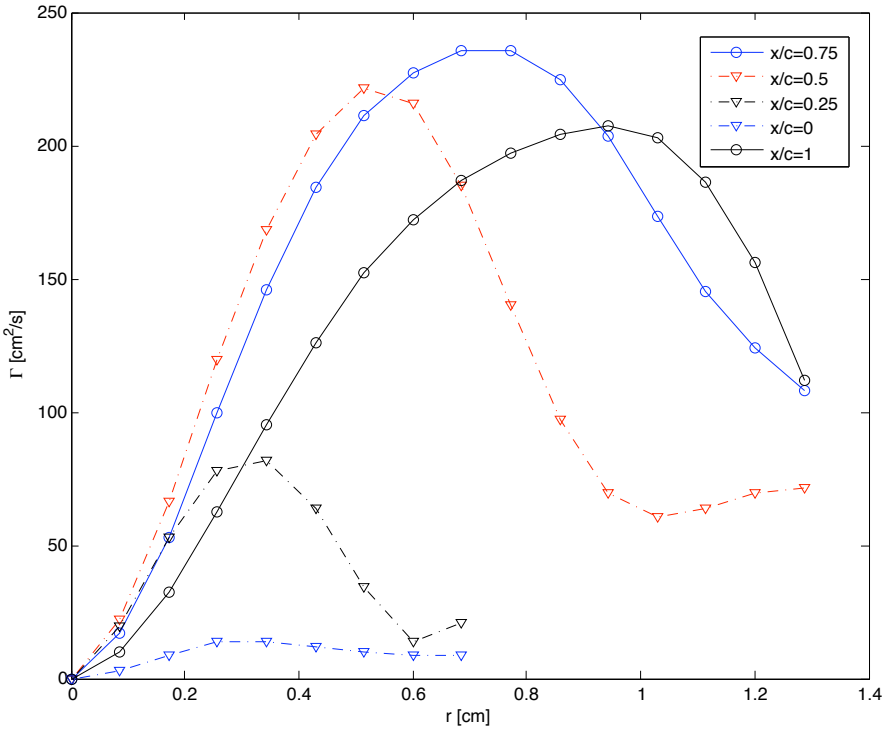

Figure 5.22: Circulation vs. radius with varying chord location for both channels at 50% DC.

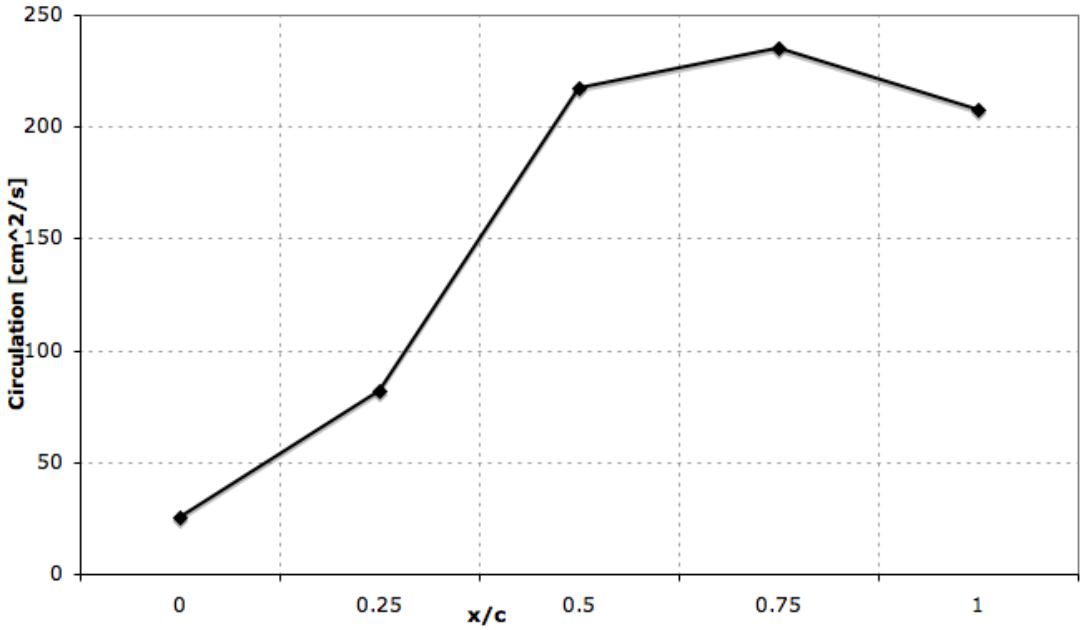

Figure 5.23: Circulation vs. chord location for both channels at 50% DC.

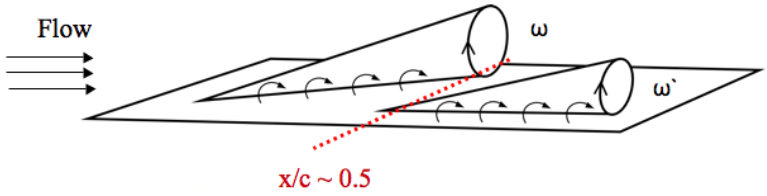

Figure 5.24: Formation of separate vortices along the streamwise direction.

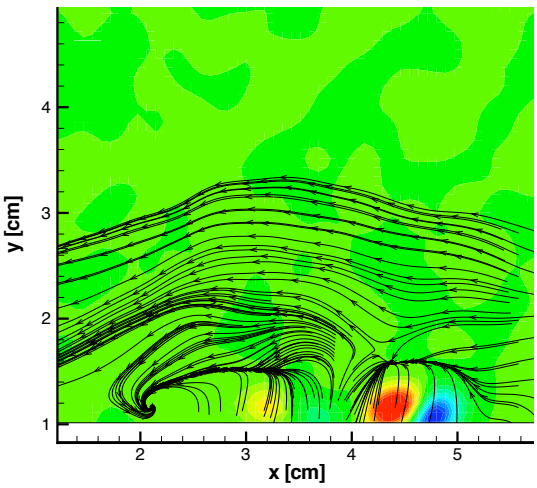

(a) x/c=0

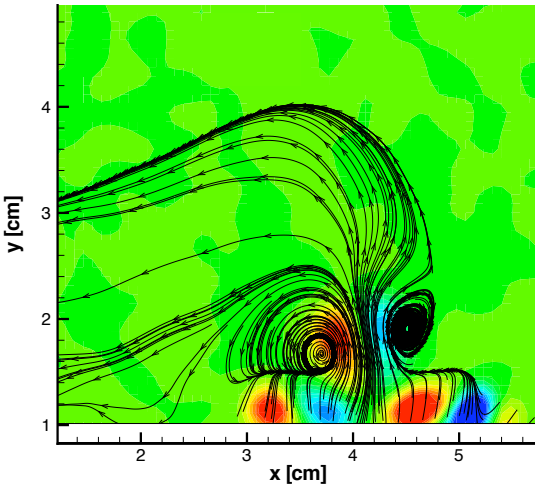

(b) x/c=0.25

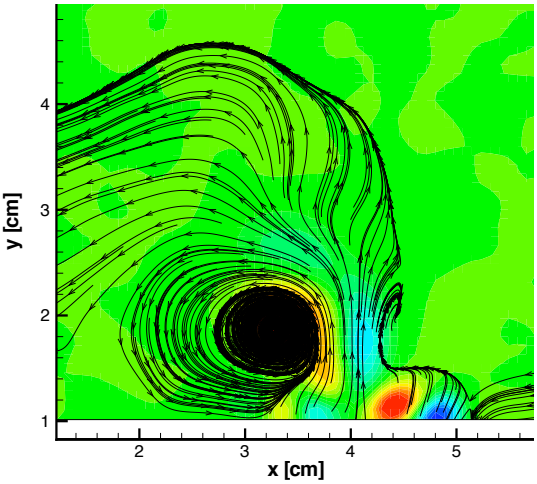

(c) x/c=0.5

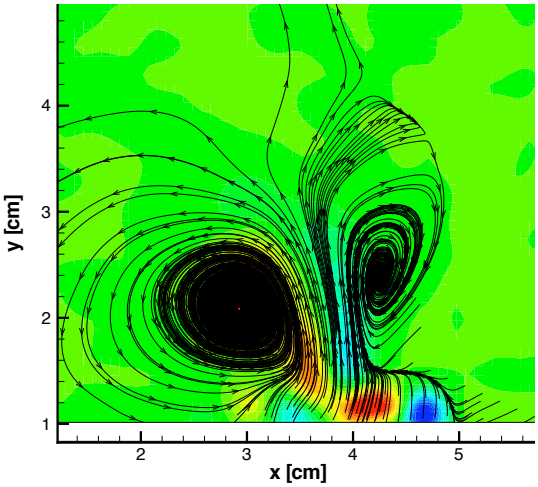

(d) x/c=0.75

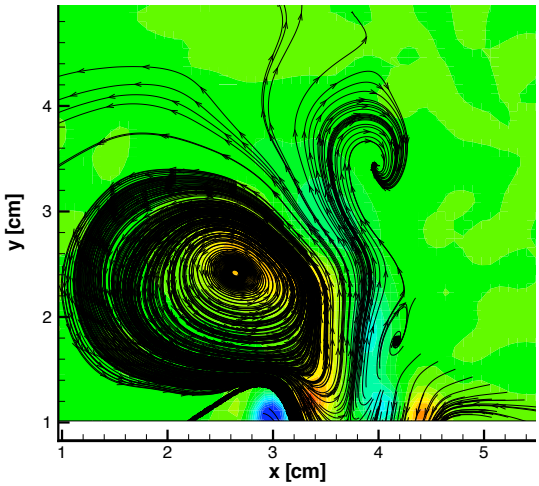

(e) x/c=1

Figure 5.25: Evolution of the vortex structure along the chord length for both channels at 50% DC.

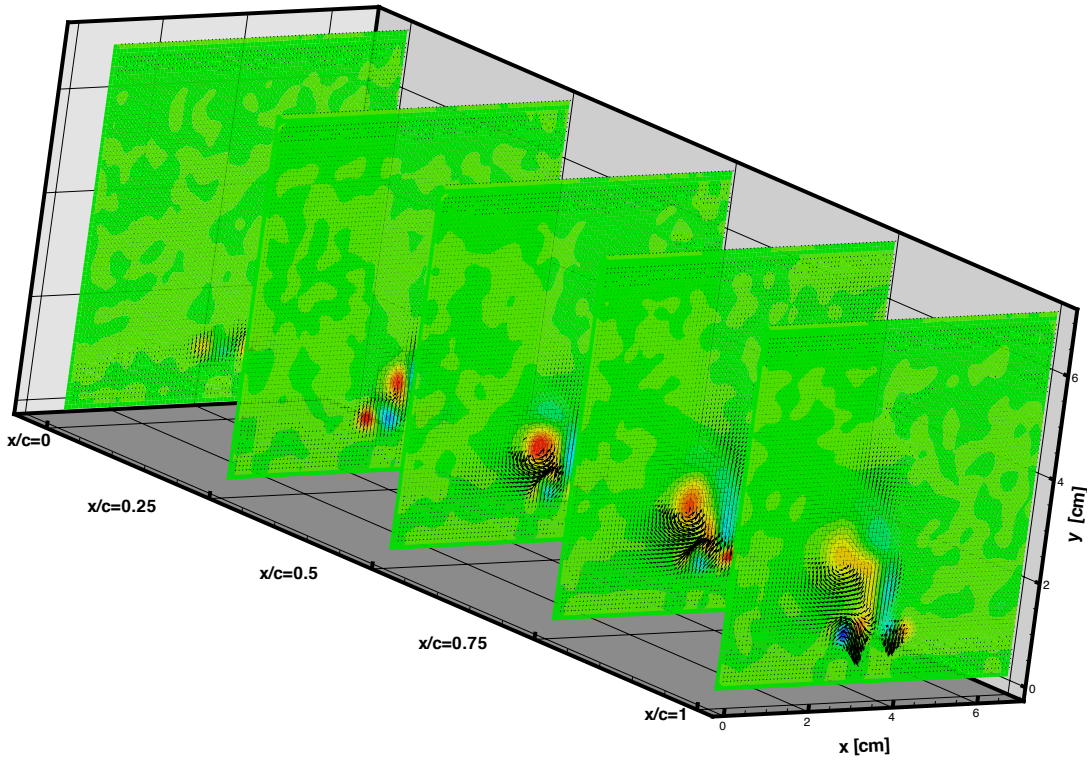

Figure 5.26: 3-D view of the field at various chord lengths for both channels at 50% DC.

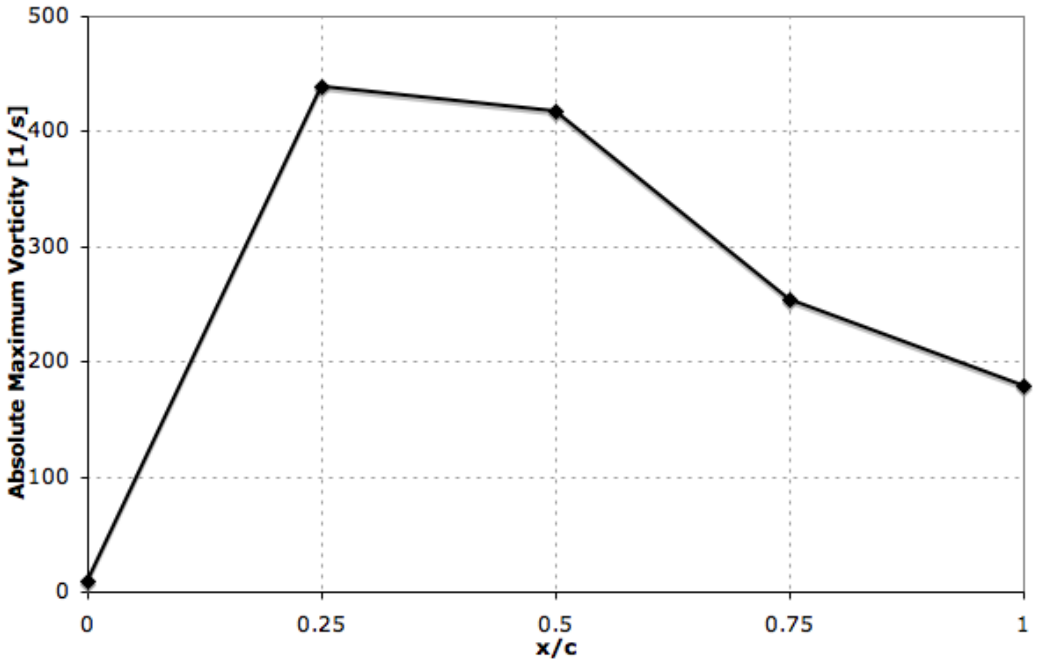

(a) Absolute maximum vorticity vs. chord location.

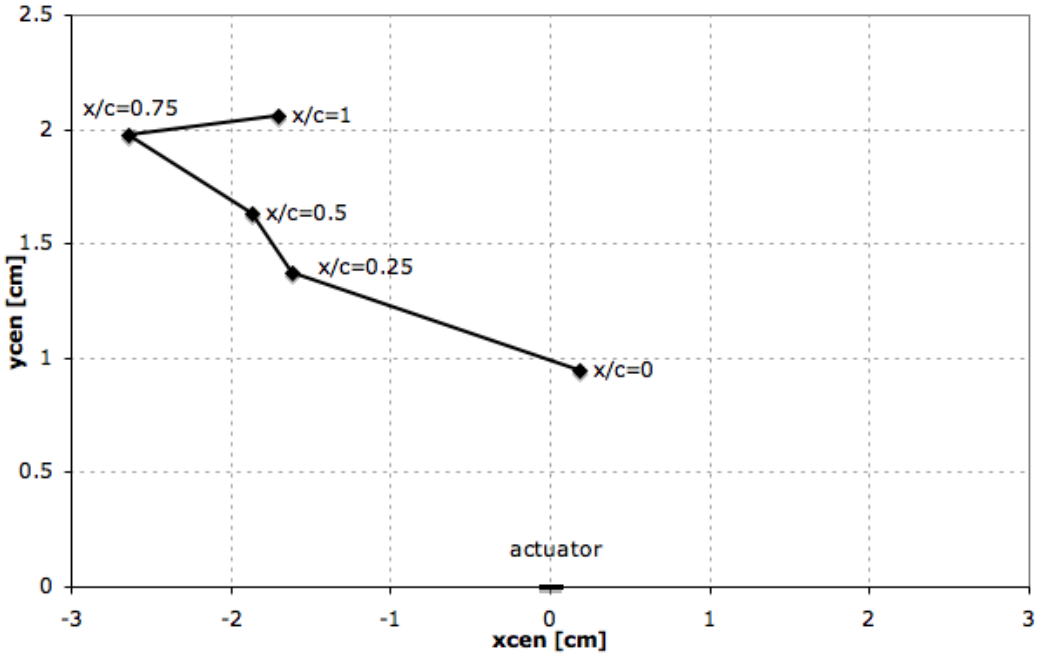

(b) x vs. y-coordinates of vortex centers.

Figure 5.27: Variation of vortex strength and position with chord location for one channel at 10% DC and the other at 50% DC.

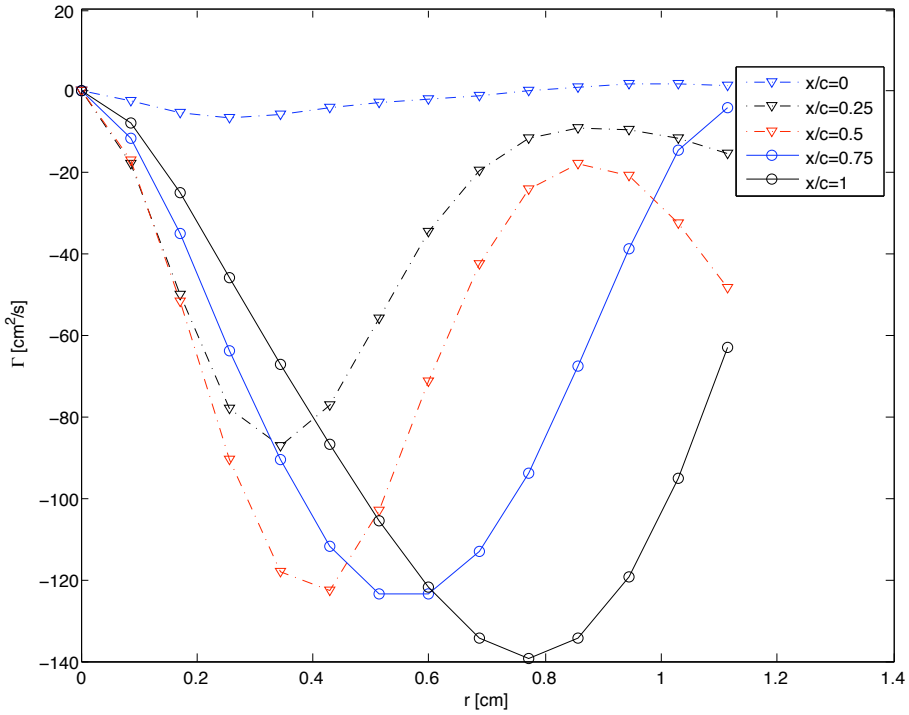

Figure 5.28: Circulation vs. radius with varying chord location for one channel at 10% DC and the other at 50% DC.

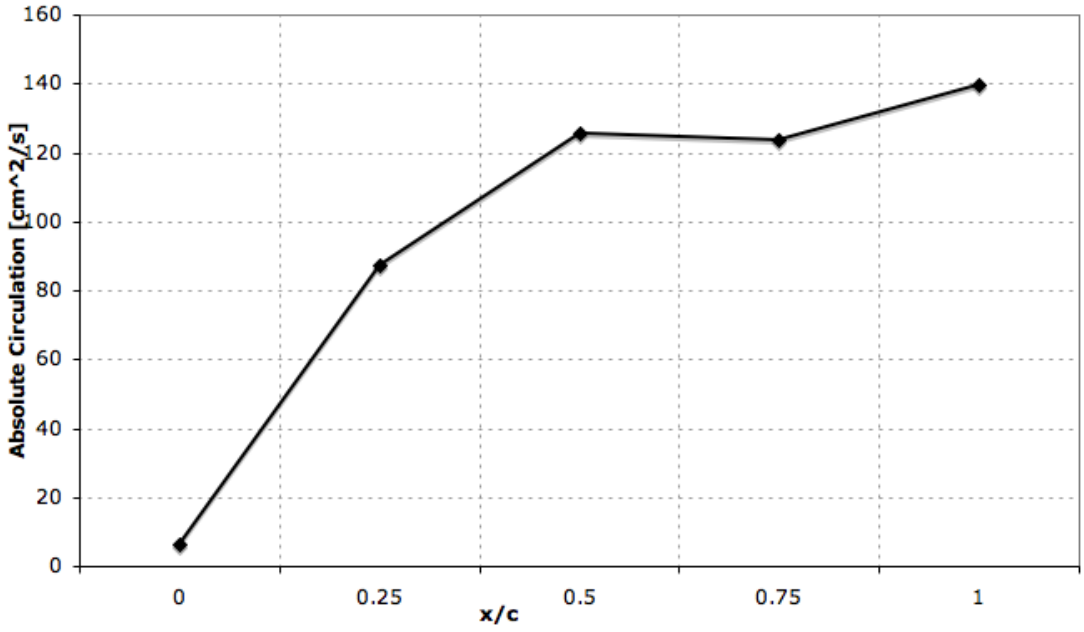

Figure 5.29: Absolute circulation vs. chord location for one channel at 10% DC and the other at 50% DC.

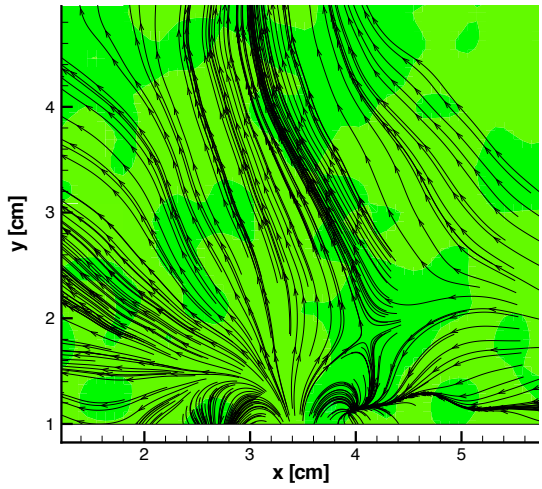

(a) x/c=0

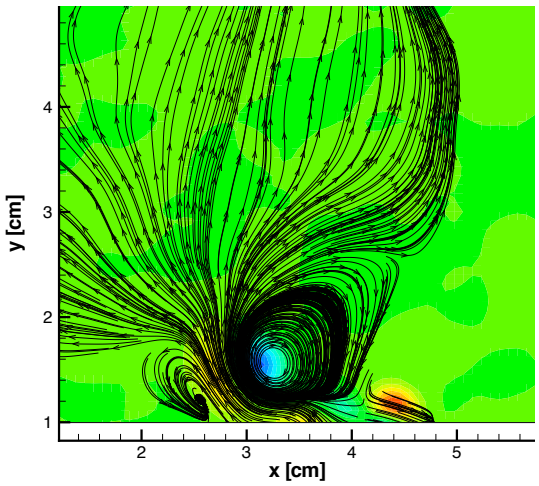

(b) x/c=0.25

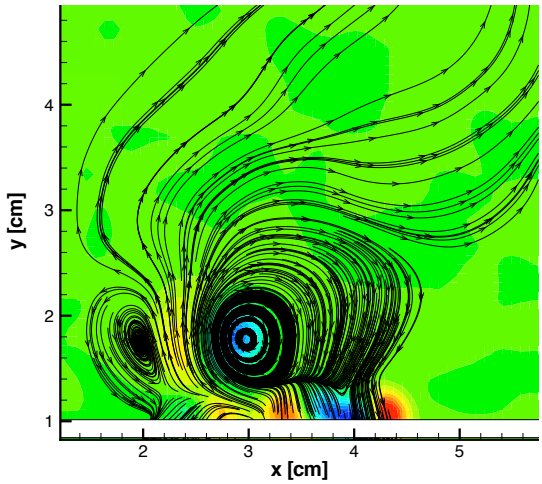

(c) x/c=0.5

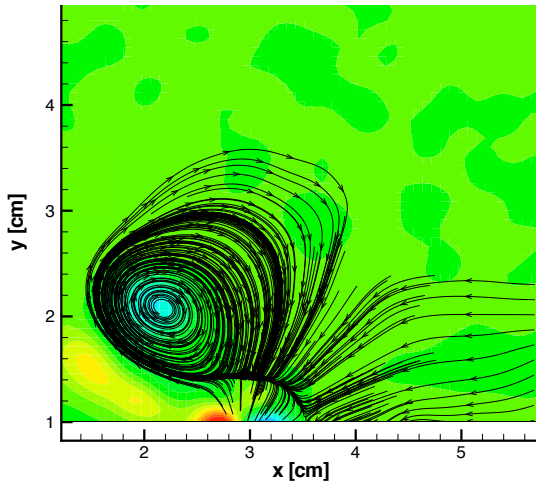

(d) x/c=0.75

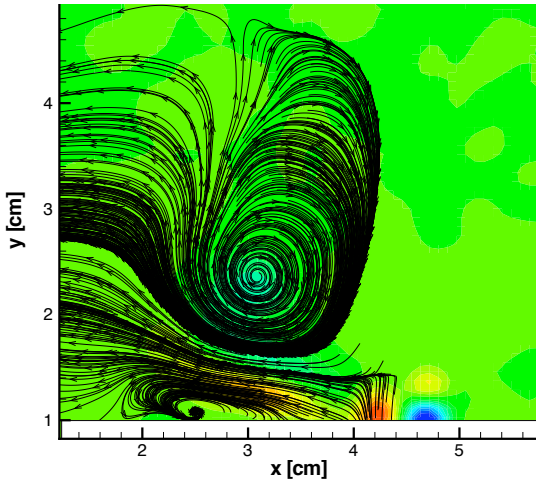

(e) x/c=1

Figure 5.30: Evolution of the vortex structure along the chord length for one channel at 10% DC and the other at 50% DC.

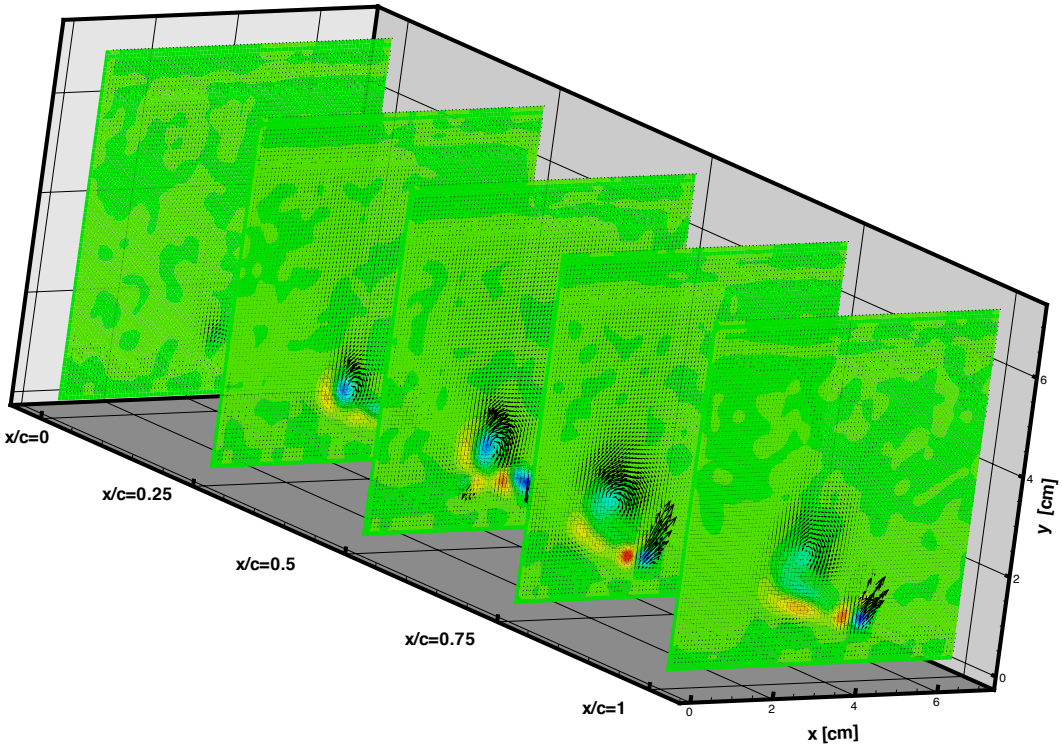

Figure 5.31: 3-D view of the field at various chord lengths for one channel at 10% DC and the other at 50% DC.

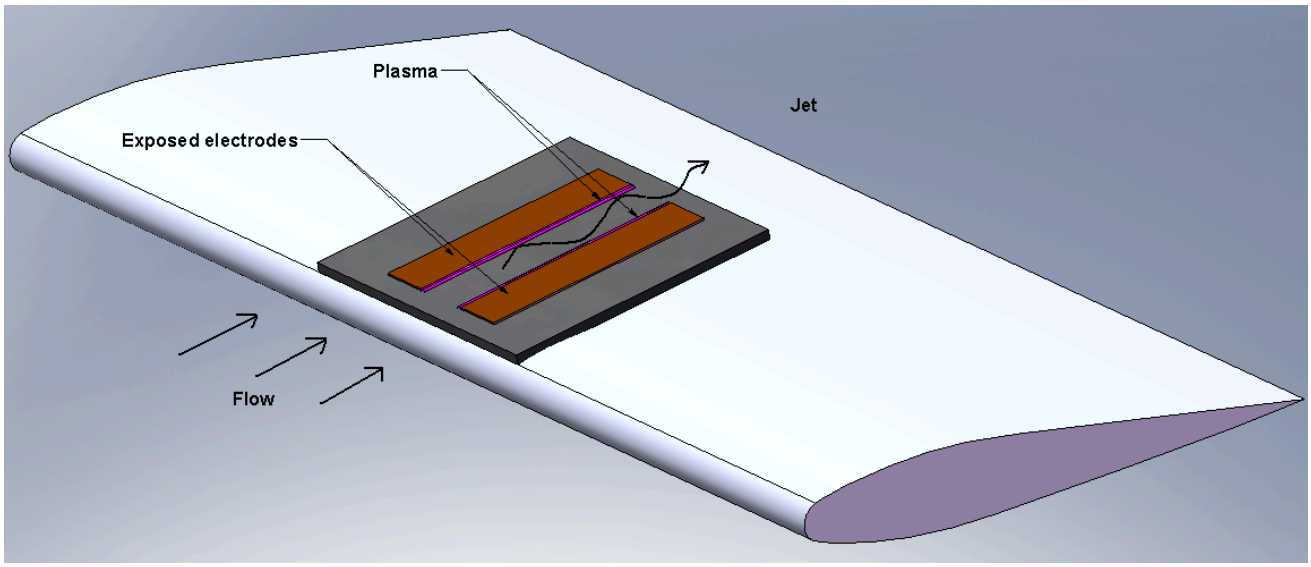

Figure 5.32: Schematic of the actuators on the wing with NACA 0012 airfoil for the tunnel tests.

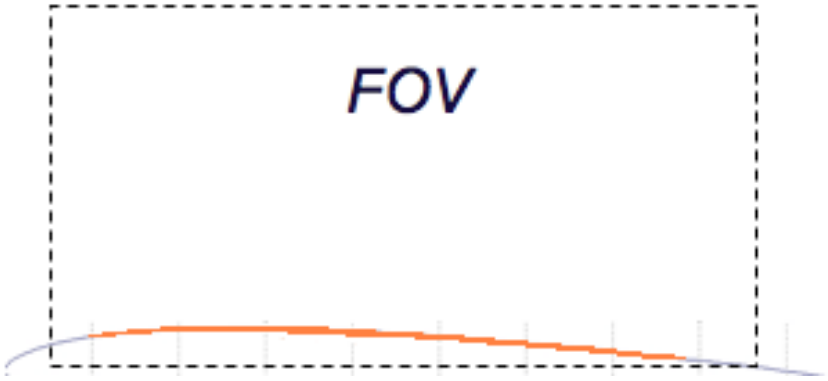

Figure 5.33: Field of view over the airfoil.

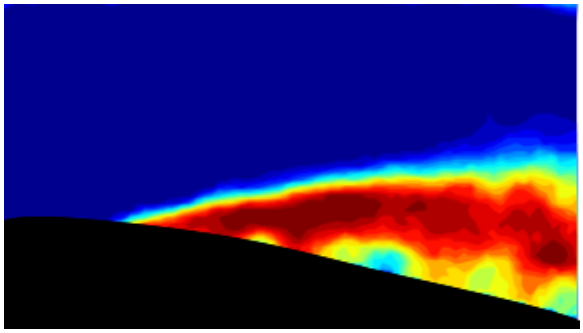

(a) actuator off

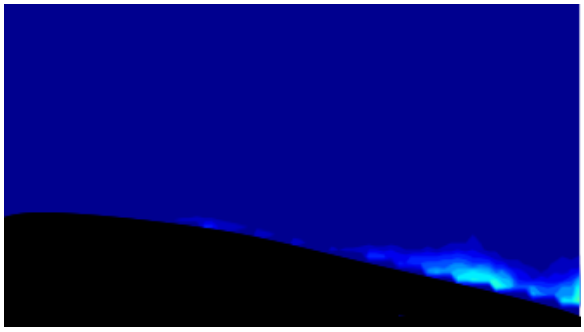

(b) 0%/50% DC

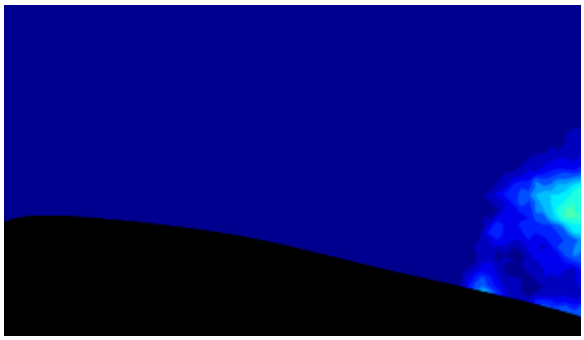

(c) 30%/50% DC

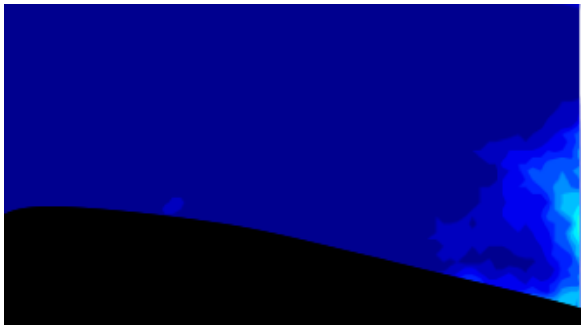

(d) 50%/50% DC

Figure 5.34: Reverse flow probability on the NACA 0012 airfoil with 0.62 m/s tunnel speed and a.o.a=10 degrees.

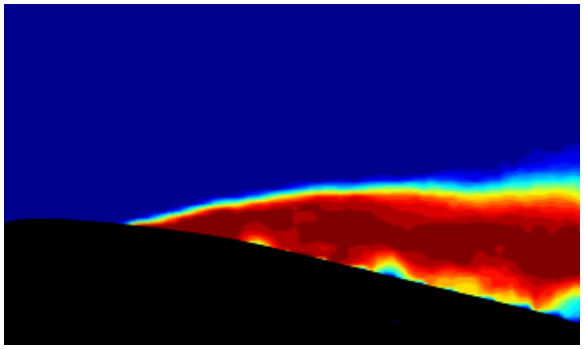

(a) actuator off

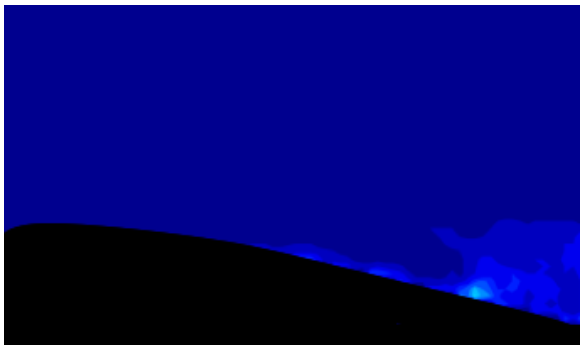

(b) 0%/50% DC

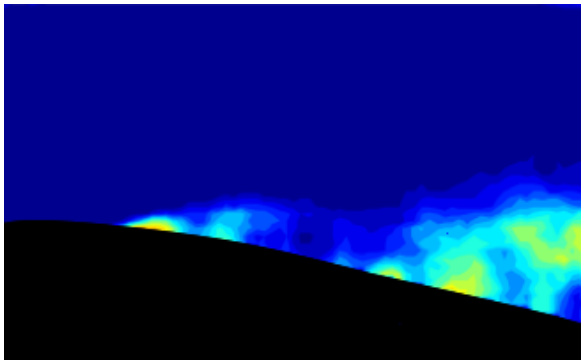

(c) 30%/50% DC

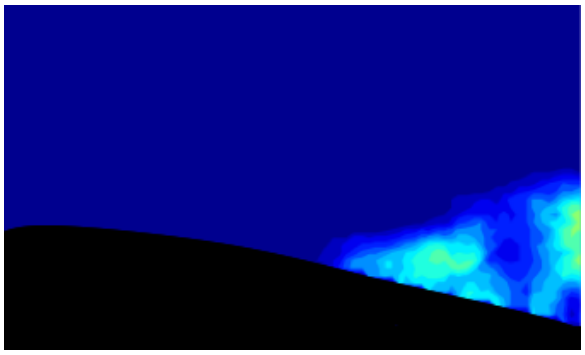

(d) 50%/50% DC

Figure 5.35: Reverse flow probability on the NACA 0012 airfoil with 1.28 m/s tunnel speed and a.o.a=10 degrees.

CHAPTER 6

Conclusions

Regarding the tests conducted, it could be concluded that the plasma actuator configuration investigated here can be used as a micro thruster. The results indicate that there should be optimum values to the varied parameters to obtain the most evenly distributed velocity profile and the maximum thrust. Of the three tubes of different ℓ/d_i ratios, it is observed that the tube with the largest diameter of d_i=1.27 cm induces the highest velocities although the 0.635 cm diameter tube does have greater maximum velocities then the 1.016 cm diameter tube. The average velocity distribution for these tubes are also very similar which shows that the flat profile of the smaller tube and the broader profile of the larger tube yield close average velocities. The thrust is the maximum for the 1.27 cm diameter tube and decreases with decreasing diameter, unlike the velocity. The effect of the duty cycle was investigated for each tube at different modulation frequencies. It was found that the velocities do increase with the duty cycle, but it was also seen that this effect decreases with increasing frequency. Peak values for thrust, maximum and average velocities all occur at different frequencies for each different diameter tube. For the 1.016 cm diameter tube, it was also observed that the peak for the maximum velocity occurs at a different forcing frequency than that of the thrust and average velocity raising a question to be answered with future work. The velocity profiles for all six tubes of different diameters for a constant frequency and DC demonstrate the influence of the (ℓ/d_i) effect clearly, shown in Fig. 6.1. The profiles are nearly parabolic for the smaller diameter cases; the maximum velocities occur near the centerline. As the diameter

increases, the centerline velocities are reduced and higher velocities can be seen in the near wall regions. For the largest diameters, the near wall velocities are the largest leaving very low centerline velocities in the flow field.

For the experiments in the wind tunnel, it was seen that the thruster with inner diameter d_i=1.016 cm has the most significant effect on the jet exit characteristics. As the tunnel speed is increased from 0.62 m/s to 2.32 m/s, this effect is decreased and the changes in the profiles become harder to distinguish. This is also observed for the higher diameters where the tubes of inner diameters d_i=1.524 cm and d_i=3.048 cm can only alter the exit velocity profiles at lower tunnel speeds while the largest thruster is practically ineffective at the highest speed of 2.32 m/s.

The effect of using staged arrays while pulsing them in phase and out of phase increases the velocity output drastically; values up to five times the single actuator case are obtained. Even though the effect of a 180 degree phase angle results in higher velocities than 0 degrees, the smallest diameter tube does not follow this trend and yields higher velocities with in phase actuation for every forcing frequency. This is also observed for the largest inner diameter of d_i=1.27 cm where after 100 Hz, pulsing in phase becomes more efficient than out of phase, another question to be addressed with future work.

Tests with the jet vectoring actuator show that the jet direction can be controlled 180 degrees by changing the duty cycle of the channels with respect to one another, shown in Fig. 6.2. The maximum vorticity values for the linear cases with 0%/50% and 50%/0% duty cycles are less than any vectoring case with different duty cycles on each channel. As for these vectoring cases, the tests with a 40%, 30% and 20% DC for one side and 50% DC on the other yield low vorticity as well, resulting from the asymmetry of plasma strength on the two channels. Because of this asymmetry, while the least amount of vorticity is expected for both channels at 50% DC, this occurs for the 40%/50% case where the vorticity reaches a minimum, changes sign

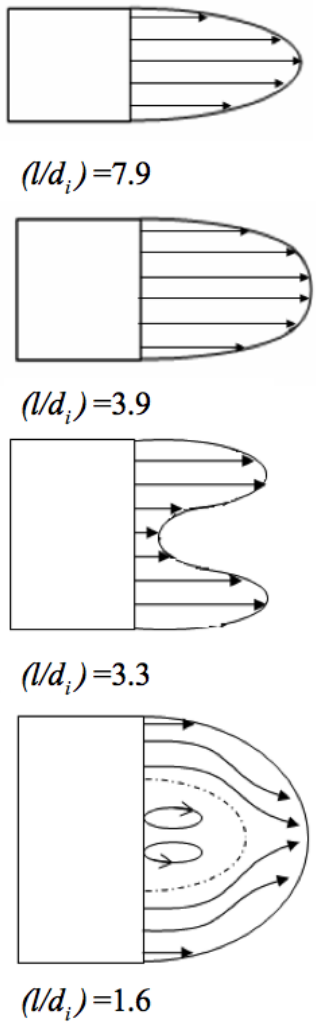

Figure 6.1: Effect of length-to-diameter ratio on the velocity profiles.

and starts to increase again with increasing discrepancy between the duty cycles of the two channels. This increase, however does not reach the values for the cases with the left side at 50% DC since the weaker right side is the main contributor to the vorticity now. A hodograph with the coordinates of the vortices illustrates that their movement is in the direction of the vectoring. Streamwise PIV measurements show that there is a significant amount of growth in the vortex along the chord from the leading edge to the trailing edge while the location of the vortex centers via hodographs and velocity vectors illustrate the braiding motion along the chord. The

maximum strength is observed at 50% chord for the case with both sides at 50% DC and at 25% chord for the left side at 10% DC and the right at 50%. The values do not vary drastically between the quarter-chord and mid-chord for each case though, meaning that the maximum strength is achieved around the mid-chord regions. As the radial circulation distributions illustrate, the circulation is mainly introduced in this region, and its continuous increase is less as the vortex is subsumed inside the boundary layer at further downstream distances. Regarding results above, it is evident that the jet vectoring actuator can be used for rapid change of the vortex sign, location and distribution, which is an improvement over a linear configuration for flow control.

The jet vectoring actuator placed on the wing proves to be effective in controlling separation, where at the lower speed of 0.62 m/s, appreciable separation control is achieved for all three cases of 0%/50%. 30%/50% and 50%/50% duty cycle values for the left and right channels, respectively. However, pulsing the actuator with 50% DC on both sides yields the best results since it generates the strongest vortex, followed by the 30%/50% and 0%/50% cases. This proves that the jet vectoring actuator is more efficient than a simple linear one, but at higher tunnel speeds the actuator decreases in efficiency and employing a linear actuator results in better flow control. Overall, though, it has been shown that the jet vectoring plasma actuator can be used as a vortex generator device to provide flow control.

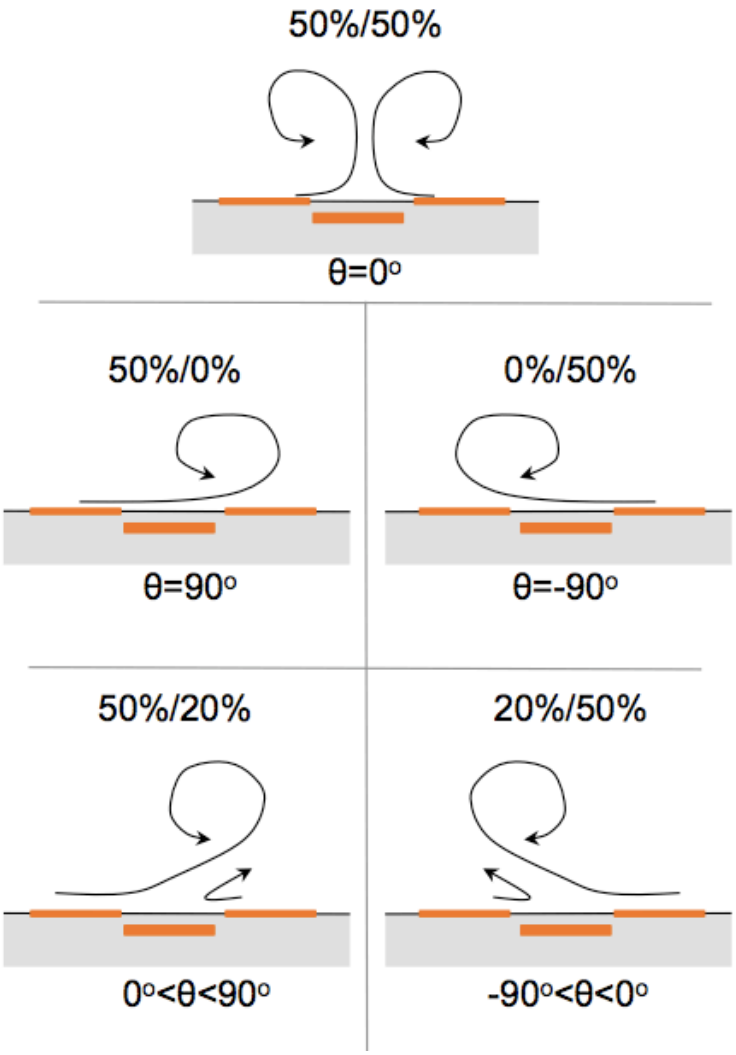

Figure 6.2: Unsteady jet vectoring by varying the duty cycles of the two channels with respect to each other.

APPENDIX A

Input Files and MATLAB Scripts

The PIV system utilized for measurements consists of frame grabbing software XCAP and processing software that makes use of the Wall Adaptive Lagrangian Parcel Tracking (WaLPT) algorithm as discussed previously. The following are the necessary input files and MATLAB scripts to process the captured images prior to post-processing for which the script is also provided here.

A.1 WaLPT Input File

The image pairs captured are processed through the WaLPT algorithm using the ASCII input file given below. This file includes information on the specific set of images, the wall parameters and the wall geometry defined by the mask file generated in MATLAB, illustrated in the next section.

```
lptmode, 0=singlepass, 1=small to large, 2=large to small, 3= LPT
2 2 0 1
input file names ( one line per file )
run1.lst
processed\run1
image size nxc, nyc, pixr
1008 1018 10 1.00
flow size, nxf, nyf
1008 1018
flow offset, xf, yf
```

```
0 0
window size, nxw, nyw, 2**n
32 32
amod, min, max windows dimensions 2**n, correlaltion level corlvl
0 8  32 0.50
step size, nxs, nys
12 12
window type, wtype 1-7, see source listing
1
peak type, ptype 0=grid,1=parabolic,2=gaussian
2
laundary type, ltype 0=no laundering,1=rejection
0
extension parameter, 0= none, zero padding, 1= smooth (nth order)
1
filter widths (1/) fltrwx,fltrwy; 0= no filtering, 1,2,.. higher
10 10 1
wall parameters: nwalls, parex, motion, intflag, outmask
2 0 0 0 0
wall geometry file
mask1_8bit.bin
motion parameters: dxcg, dycg ,rot
0.0 0.00 0.00
0.00 0.00 0.00
0.00 0.00 0.00
```

A.2 MATLAB Scripts

A.2.1 Mask Generation

The frame grabbing package stores the images in a 10-bit binary format. In order to define the wall geometry to be used in the input file for the WaLPT algorithm, one of the images is masked in this 10-bit format. The code below converts this file to a 8-bit format in order for the processing algorithm to use it.

```
%FIRST MASK
path2='/Users/ceren/Desktop/vectoring/10.15.08/processed/'
maskfile=strcat(path2,'mask1_10bit.bin')
maskfile2=strcat(path2,'mask1_8bit.bin');
nxc=1008;
nyc=1018;
colormap(gray);

% load 10 bit xcap image as 16 bit image
fid=fopen(maskfile,'r');
maskimage=fread(fid,[nxc,nyc],'int16');
st=fclose(fid);
figure(1);
imagesc(maskimage.'),axis off,title('original mask');

% set values in array to floor and ceiling of the raw xcap image
for i=1:nxc;
    for j=1:nyc;
        if maskimage(i,j)<240;
```

```
            maskimage(i,j)=0;
        else
            maskimage(i,j)=255;
        end
    end
end

%save the mask file(s)
fid=fopen(maskfile2,'w');
fwrite(fid,maskimage,'int8');
st=fclose(fid);

% display mask
figure(2);
colormap(gray);
imagesc(maskimage.'),axis off,title('final mask');
%end
```

A.2.2 Post-processing

The WaLPT algorithm outputs tensor files to be read by the MATLAB script below which is used to obtain velocity, vorticity and other flow variables.

```
function plasma4
% program to analyze plasma PIV data sets generated by the WaLPT PIV program

run='9'
```

```
flag=1; %(flag==2 writes instantaneous tecplot files)

%set base path of files
basepath=strcat('/Users/ceren/Desktop/vectoring/10.15.08/processed/')

%total number of pairs
none=1; nlas=63;
ntot=nlas-none+1;

%check array size
k=1; [ny,nx,nyc,nxc]=tensfunc2(run,k,basepath)

%create empty arrays
uav=zeros(ntot,nx,ny);
vav=zeros(ntot,nx,ny);
vortav=zeros(ntot,nx,ny);
contav=zeros(ntot,nx,ny);
un=zeros(nx,ny);
vn=zeros(nx,ny);
vorn=zeros(nx,ny);
conn=zeros(nx,ny);
corn=zeros(nx,ny);
ctru=zeros(nx,ny);
ctrv=zeros(nx,ny);
urms=zeros(nx,ny);
dvdxn=zeros(1,ny);
```

```
%conversion info - spatial and temporal scales to give units in cm/s
scale=134;  %pixels/cm
pulse=50;  %microseconds

%conversion factors to cm/s
convel=(scale*pulse/1000000);  %[s/cm]
convor=(pulse/1000000); %[s]

%create xs and ys arrays for scaling
scale=scale*nx/nxc %vectors/cm
xs=[1:nx]./scale; ys=[1:ny]./scale; %xs and ys arrays in cm

%characteristic velocity based on 5400 fpm (~30 m/s)
uf=30;

%read in data files
for i=none:nlas
    [u,v,vort,cont,corr,dvdx]=tensfunc(run,i,basepath);
    un=u+un;
    vn=v+vn;
    vorn=vort+vorn;
    conn=cont+conn;
    corn=corr+corn;

%arrays of instantaneous values
    uav(i,:,:)=u;
    vav(i,:,:)=v;
```

```
    wav(i,:,:)=vort;
    vortav(i,:,:)=vort;
    contav(i,:,:)=cont;
    dvdxn=dvdxn+dvdx(nx,:);
    avecorr(i)=median(median(corr));
    for j=1:nx
        for k=1:ny
            if u(j,k) < 0
                ctru(j,k)=ctru(j,k)+1;
            end
            if v(j,k) < 0
                ctrv(j,k)=ctrv(j,k)+1;
            end
        end
    end
end

%%%%%%%%%%%%%% PROCESSING %%%%%%%%%%%%%%%%%%%%
%calculate averages
un=un/ntot;
vn=vn/ntot;
vorn=vorn/ntot;
conn=conn/ntot;
corn=corn/ntot;
dvdxn=dvdxn/ntot;
ctru=ctru/ntot;
ctrv=ctrv/ntot;
```

```
%scale data
un=un/convel;
vn=vn/convel;
vorn=vorn/convor;
uav=uav/convel;
vav=vav/convel;
muav=squeeze(median(uav(none:nlas,:,:),1));
mvav=squeeze(median(vav(none:nlas,:,:),1));
mwav=squeeze(median(wav(none:nlas,:,:),1));

fprintf('\nThinking....\n')
urms=std(uav,0,1);
urms=squeeze(urms);
vrms=std(vav,0,1);
vrms=squeeze(vrms);

un=rot90(un,-1);vn=rot90(vn,-1);
vorn=rot90(vorn,-1);conn=rot90(conn,-1);
corn=rot90(corn,-1);
dvdxn=rot90(dvdxn,-1); %dudyn=rot90(dudyn,-1);
%dudxn=rot90(dudxn,-1); dvdyn=rot90(dvdyn,-1);
urms=rot90(urms,-1);vrms=rot90(vrms,-1);

%skin friction coef.
mu=0.0000185;
shear=mu*dvdxn;
```

```
cf=shear/(0.5*1.23*uf^2);


%% PLOTTING
offset=0;
xulim=nx-offset;
yulim=ny-(offset);
yllim=offset;
xllim=offset;


%set edge regions to zero if need be
un(:,1)=0; vn(:,1)=0; vorn(:,1)=0;
un(:,2)=0; vn(:,2)=0; vorn(:,2)=0;
un(1,:)=0; vn(1,:)=0; vorn(1,:)=0;
un(2,:)=0; vn(2,:)=0; vorn(2,:)=0;
un(1,:)=0; vn(1,:)=0; vorn(1,:)=0;
un(:,ny-1)=0; vn(:,ny-1)=0; vorn(:,ny-1)=0;
un(:,ny)=0; vn(:,ny)=0; vorn(:,ny)=0;


%mean velocity magnitude
mag=sqrt(un.^2+vn.^2);
zs=[1:5]*5;
    fprintf('\n Writing tecplot file of averaged data\n\n')
    Imax=ny; Jmax=nx; Kmax=5;
    tecid=fopen(strcat(basepath,'tecrun',num2str(run),'.dat'),'w');
    fprintf(tecid,'variables = "i", "j", "k", "x", "y", "z", "u", "v", "w" "vorn"\n'
    fprintf(tecid,'zone i=%i j=%i k=%i f=point \n',Imax,Jmax,Kmax);
    k=5
```

```
    for j=1:Jmax
        %3d plot
        for i=1:Imax
                u(i,j,k)=un(i,j);
                v(i,j,k)=vn(i,j);
                vor(i,j,k)=vorn(i,j);
            fprintf(tecid,'%i %i %i %f %f %f %f %f %f %f\n',j,i,k,
            xs(j),ys(i),zs(k),-v(i,j,k),u(i,j,k),0,vor(i,j,k));
        end
    end
    fclose(tecid);

if flag==2;
    fprintf('\n Writing tecplot files of instantaneous data')
    Imax=ny; Jmax=nx;
    for k=none:nlas
        fprintf('.')
        kbat=int2str(k);
        tecid=fopen(strcat(basepath,'tecrun',num2str(run),'_',kbat,'.dat'),'w');
        fprintf(tecid,'variables = "i", "j", "x", "y", "u", "v", "vorn"\n');
        fprintf(tecid,'zone i=%i j=%i f=point \n',Imax,Jmax);
        for j=1:Jmax
            for i=1:Imax
                fprintf(tecid,'%f %f %f %f %f %f\n',j,i,
                xs(j),ys(i),uav(k,j,i),vav(k,j,i),wav(k,j,i));
            end
        end
```

```
        fclose(tecid);
    end
    fprintf('\n\n')
end

%% PLOTS
figure(1);
colormap jet;
contourf(mag,20),axis equal,axis([0 80 0 80]),
title('Velocity Magnitude'),axis ij,shading flat;
colorbar;

figure(2);
colormap jet;
contourf(vorn,50),axis on, axis equal,axis([0 80 0 80]),
title('Vorticity'),axis ij,shading flat;
colorbar;

%%%Circulation calculation%%
%find center of vortex
[xcen,ycen]=ginput(1);
xcen=round(xcen)
ycen=round(ycen)
gamma_vor=0;
gamma_vel=0;
boxwidth=10;
dx=xs(2)-xs(1)
```

```
radius=[0:boxwidth]/scale;


for iter=1:boxwidth
    cbox=iter;
    hold on;
    plot([xcen-cbox,xcen-cbox],[ycen-cbox,ycen+cbox],'y-')
    plot([xcen+cbox,xcen+cbox],[ycen-cbox,ycen+cbox],'y-')
    plot([xcen-cbox,xcen+cbox],[ycen-cbox,ycen-cbox],'y-')
    plot([xcen-cbox,xcen+cbox],[ycen+cbox,ycen+cbox],'y-')
    plot([xcen],[ycen],'c.','markersize',20)
    hold off;

    %circulation via vorticity
    for i=xcen-cbox:xcen+cbox
        for j=ycen-cbox:ycen+cbox
            gamma_vor= (gamma_vor+vorn(j,i));
        end
    end
    gamma_vor=gamma_vor*dx^2

    %circulation via velocity
    for i=xcen-cbox:xcen+cbox
        gamma_vel=(un(ycen+cbox,i)+gamma_vel)
    end
    for j=ycen+cbox:ycen-cbox
        gamma_vel=(vn(j,xcen+cbox)+gamma_vel);
    end
```

```
    for i=xcen+cbox:xcen-cbox
        gamma_vel=(-un(ycen-cbox,i)+gamma_vel);
    end
    for j=ycen-cbox:ycen+cbox
        gamma_vel=(-vn(j,xcen-cbox)+gamma_vel);
    end
    gamma_vel=gamma_vel*dx

    gamma_itervor(iter)=gamma_vor;
    gamma_itervel(iter)=gamma_vel;
end

gamma_itervor=[0,gamma_itervor];
gamma_itervel=[0,gamma_itervel];

figure(3);
contourf(ctrv,20),axis off, axis equal,axis([0 80 0 80]),
title('RFP'),axis ij,shading flat;
colorbar;

figure(4);
quiver(muav,mvav,10),axis equal,axis([0 80 0 80]),axis ij;
[dumx,dumy]=ginput(1)

figure(5);
colormap jet;
contourf(dvdx.',50),axis off, axis equal,axis([0 80 0 80]),
```

```
title('RMS Velocity Variation'),axis ij,shading flat;
colorbar;

figure(6);
colormap jet;
contourf(corn.',[0 .1 .2 .3 .4 .5 .6 .7 .8 .9 1.0]),axis off, axis equal,
title('Average PIV Correlation: Run 4'),axis ij;
colorbar;

figure(7)
plot(avecorr,'b-o');
xlabel('frame number, N'),ylabel('median corr'),title('Median Image Correlation');
grid on;

%%% This section makes profiles going "up"
figure(8);
plot(ys,vn(:,30),'-k'),ylabel('v [cm/s]'),xlabel('x [cm]'),axis([0 10 -10 40]);
hold on
plot(ys,vn(:,40),'-b');
plot(ys,vn(:,50),'-r');
plot(ys,vn(:,60),'--k');
hold off

leg1=(30-dumy)/scale;
leg2=(40-dumy)/scale;
leg3=(50-dumy)/scale;
leg4=(60-dumy)/scale;
```

```
legend(strcat('y=',num2str(leg1),'cm'),strcat('y=',num2str(leg2),'cm'),
strcat('y=',num2str(leg3),'cm'),strcat('y=',num2str(leg4),'cm'))

offset=2.0;

%%% This section makes profiles going "right"
figure(9);
plot(un(35,:),xs-offset,'-k'),xlabel('u [cm/s]'),ylabel('y [cm]'),axis([-2 400 -3 3]
hold on
plot(un(40,:),xs-offset,'--k');
plot(un(60,:),xs-offset,'-.k');
plot(un(80,:),xs-offset,':k');
plot([0,15],[0.5,0.5],'-k+');
plot([0,15],[-0.5,-0.5],'-k+');
plot([15,15],[-0.5,0.5],'-k+')
hold off

leg1=(35-dumx)/scale;
leg2=(40-dumx)/scale;
leg3=(60-dumx)/scale;
leg4=(80-dumx)/scale;

legend(strcat('x=',num2str(leg1),'cm'),strcat('x=',num2str(leg2),'cm'),
strcat('x=',num2str(leg3),'cm'),strcat('x=',num2str(leg4),'cm'))

%average velocity and maximum velocty vectors
```

```
ylim1=10;
ylim2=30;
for j=1:80
    meanu(j)=(1./(xs(ylim2:ylim2)-xs(ylim1:ylim1)))*
    trapz(xs(ylim1:ylim2),un(j,ylim1:ylim2));
end
[maxun,dumun]=max(un,[],2);

figure(10);
plot(ys,maxun),xlabel('x [cm]');
hold on
plot(ys(1:80),meanu,'r-');
hold off

figure(11);
plot(uav(:,round(dumx),round(dumy)),'b-');
hold on
plot(vav(:,round(dumx),round(dumy)),'r--');
hold off

figure(12);
plot(radius,gamma_itervel),xlabel('r [cm]'),ylabel('Circulation_{vel} [cm^2/s]');

figure(13);
plot(radius,gamma_itervor),xlabel('r [cm]'),ylabel('Circulation_{vor} [cm^2/s]');

%single ave and max velocities
```

```
fprintf('\nMax velocity is %5.2f cm/s\n',max(max(mag(50:70,10:30))));
avg_vel=mean(meanu(1:80));
fprintf('\nMean jet velocity is %5.2f cm/s\n',avg_vel);
maxvor=max(max(abs(vorn(55:60,10:20))));
fprintf('\nMax vorticity is %5.2f s^-1\n',maxvor);
force=0.5*1.23*(mean(max(mag))/100)^2;
fprintf('\nForce per unit area based on mean velocity is %5.2f N/m^2\n',force);



return;
%end of main routine and loop

function [e1,e2,vorticity,continuity,corr,dvdx]=tensfunc(run,batch,basepath)
% MATLAB Script to read WALPT data and image files.
% Jamey Jacob, Jan. 18 2000
% Version 1.1, last modified Feb. 15, 2000
% Miner version May 30, 2001 - only data read
%
% For use with MATALB release 11 (5.3)
% Ticker will not work with older versions (see "movie")
% jdjacob@uky.edu
bat=int2str(batch);
% file and path names
if batch < 10
    bat=strcat('.00',bat);
else
    if batch < 100
```

```
        bat=strcat('.0',bat);
    else
        bat=strcat('.',bat);
    end
end
lptfile=strcat('run',run,bat);
lptima1=strcat('image1.lpt');lptima2=strcat('image2.lpt');
u_infinity=0;
v_infinity=0;

%set paths and file names
path=strcat(basepath);
rdfile=strcat(path,lptfile);
imfile1=strcat(path,lptima1);
imfile2=strcat(path,lptima2);

% read data file into header and tensor arrays

fprintf(' Reading single tensor file %s in %s\n',lptfile,path)
fid=fopen(rdfile,'r');
header=fread(fid,64,'int16');
  version=header(1);                % walpt version number (starting with 300)
  nxc =header( 2) ; nyc =header( 3); % camera size
  nxuv=header( 4) ; nyuv=header( 5); % velocity array size
  nxw =header( 6) ; nyw =header( 7); % window sizes in pixels
  nxs =header( 8) ; nys =header( 9); % step sizes in pixels
  nxf =header(10) ; nyf =header(11); % flow region size in pixels
```

```
  xf  =header(12) ; yf  =header(13); % flow region offset in pixels
  nbits=header(14);                  % pixel depth of original flow images
  % read tensor components from file in succession
  e1=fread(fid,[nxuv,nyuv],'float'); % u
  e2=fread(fid,[nxuv,nyuv],'float'); % v
  e3=fread(fid,[nxuv,nyuv],'float'); % du/dx
  e4=fread(fid,[nxuv,nyuv],'float'); % dv/dx
  e5=fread(fid,[nxuv,nyuv],'float'); % du/dy
  e6=fread(fid,[nxuv,nyuv],'float'); % dv/dy
  e7=fread(fid,[nxuv,nyuv],'float'); % correlation
st=fclose(fid);

%rotate fields
e1=e1.';
e2=e2.';
e3=e3.';
e4=e4.';
e5=e5.';
e6=e6.';
e7=e7.';

% add (subtract) v_infinity to the velocity field to change
% reference frames to object's frame for tow-tank
% runs.  Set u_infinity to zero to run in lab frame.

for i=1:nyuv
   for j=1:nxuv
```

```
      if e1(i,j)<=999
         e1(i,j)=e1(i,j)-u_infinity;
      end
   end
end

for i=1:nyuv
   for j=1:nxuv
      if e2(i,j)<=999
         e2(i,j)=e2(i,j)+v_infinity;
      end
   end
end

% Check and replace the "missing" 1000 in velocity fields with zeros
% (option XXXX in walpt).
% (This option is for use with IDL or similar programs.)
for i=1:nyuv
   for j=1:nxuv
   if e1(i,j) > 999
           e1(i,j) = 0;
                   end
                   if e2(i,j) > 999
                        e2(i,j) = 0;
                   end
    end
end
```

```
%Items to return
corr=e7;

% Calculate vorticity,continuity
  vorticity=e5-e4;    %du/dy-dv/dx
continuity=e3+e6;   %du/dx+dv/dy

%return velocity gradient for wall skin friction calculation (in this case, dv/dx)
dvdx=e4;
return

function [nx,ny,nxc,nyc]=tensfunc2(run,batch,basepath)
% MATLAB Script to read WALPT data and image files.
% Jamey Jacob, Jan. 18 2000
% Version 1.1, last modified Feb. 15, 2000
% Miner version May 30, 2001 - only data read
%
% For use with MATALB release 11 (5.3)
% Ticker will not work with older versions (see "movie")
% jdjacob@uky.edu
bat=int2str(batch);
% file and path names
if batch < 10
    bat=strcat('.00',bat);
else
    if batch < 100
```

```
        bat=strcat('.0',bat);
    else
        bat=strcat('.',bat);
    end
end
lptfile=strcat('run',run,bat);
lptima1=strcat('image1.lpt');lptima2=strcat('image2.lpt');
u_infinity=0;
v_infinity=0;

%set path and file names
path=strcat(basepath);
rdfile=strcat(path,lptfile);
imfile1=strcat(path,lptima1);
imfile2=strcat(path,lptima2);

% read data file into header and tensor arrays

fprintf(' Reading tensor file %s in %s to determine array size\n',lptfile,path)
fid=fopen(rdfile,'r');
header=fread(fid,64,'int16');
  version=header(1);                % walpt version number (starting with 300)
  nxc =header( 2) ; nyc =header( 3); % camera size
  nxuv=header( 4) ; nyuv=header( 5); % velocity array size
  nxw =header( 6) ; nyw =header( 7); % window sizes in pixels
  nxs =header( 8) ; nys =header( 9); % step sizes in pixels
  nxf =header(10) ; nyf =header(11); % flow region size in pixels
```

```
  xf  =header(12) ; yf  =header(13); % flow region offset in pixels
  nbits=header(14);                  % pixel depth of original flow images

  % read tensor components from file in succession
  e1=fread(fid,[nxuv,nyuv],'float'); % u
  e2=fread(fid,[nxuv,nyuv],'float'); % v
  e3=fread(fid,[nxuv,nyuv],'float'); % du/dx
  e4=fread(fid,[nxuv,nyuv],'float'); % dv/dx
  e5=fread(fid,[nxuv,nyuv],'float'); % du/dy
  e6=fread(fid,[nxuv,nyuv],'float'); % dv/dy
  e7=fread(fid,[nxuv,nyuv],'float'); % correlation
st=fclose(fid);
nx=nxuv;
ny=nyuv;
return
```

BIBLIOGRAPHY

[1] T. C. Corke, E. J. Jumper, M. Post, D. Orlov, and T. E. McLaughlin, "Application of weakly-ionized plasmas as wing flow-control devices," AIAA Paper 2002–0350, 40th AIAA Aerospace Sciences Meeting and Exhibit, Reno, NV, Jan. 2002.

[2] L. S. Hultgren and D. E. Ashpis, "Demonstration of separation delay with glow-discharge plasma actuators," AIAA Paper 2003–1025, 41 st AIAA Aerospace Sciences Meeting and Exhibit, Reno, NV, Jan. 2003.

[3] M. L. Post and T. C. Corke, "Separation control using plasma actuators – dynamic stall control on an oscillating airfoil," AIAA Paper 2004–2517, 2nd AIAA Flow Control Conference, Portland, OR, June 2004.

[4] T. E. McLaughlin, M. D. Munska, J. P. Vaeth, T. E. Dauwalter, J. R. Goode, and S. G. Siegal, "Plasma-based actuators for cylinder wake vortex control," AIAA Paper 2004–2129, 2nd AIAA Flow Control Conference, Portland, OR, June 2004.

[5] J. D. Jacob, R. Rivir, C. Carter, and J. Estevadeordal, "Boundary layer flow control using ac discharge plasma actuators," AIAA Paper 2004–2128, 2nd AIAA Flow Control Conference, Portland, OR, June 2004.

[6] J. D. Jacob, K. Ramakumar, R. Anthony, and R. B. Rivir, "Control of laminar and turbulent shear flows using plasma actuators," TSFP 4-225, 4th International Symposium on Turbulence and Shear Flow Phenomena, Williamsburg, VA, June 2005.

[7] J. Huang, T. C. Corke, and F. O. Thomas, "Plasma actuators for separation control of low-pressure turbine blades," *AIAA Journal*, vol. 44, no. 1, pp. 51–57, 2006.

[8] A. Santhanakrishnan and J. D. Jacob, "On plasma synthetic jet actuators," AIAA Paper 2006–0317, 44th AIAA Aerospace Sciences Meeting and Exhibit, Reno, NV, Jan. 2006.

[9] A. Santhanakrishnan and J. D. Jacob, "Flow control with plasma synthetic jet actuators," *J. Phys. D: Appl. Phys.*, vol. 40, 2007.

[10] M. McQuilling, B. Hollon, and J. D. Jacob, "Active separation flow control in a low pressure turbine blade cascade model," AIAA Paper 2003–0615, 41st Aerospace Sciences Meeting and Exhibit, Reno, NV, Jan. 2003.

[11] M. McQuilling and J. D. Jacob, "Effect of chord location on separation control with vortex generator jets on low pressure turbine blades," AIAAaper 2004–2205, 2nd AIAA Flow Control Conference, Portland, OR, June 2004.

[12] J. P. Bons, L. C. Hansen, J. P. Clark, P. J. Koch, and R. Sondergaard, "Designing low-pressure turbine blades with integrated flow control," ASME Paper gt2005-68962, ASME Turbo Expo 2005, Reno, NV, June 2005.

[13] A. Gross and H. Fasel, "Investigation of low-pressure turbine separation control," AIAA Paper 2007-0520, 45th Aerospace Sciences Meeting and Exhibit, Reno, NV, Jan. 2007.

[14] A. Krzysiak, "Control of flow separation using self-supplying air-jet vortex generators," *AIAA Journal*, vol. 46, no. 9, 2008.

[15] A. Glezer and M. Amitay, "Synthetic jets," *Annual Rev. of Fluid Mech.*, vol. 34, pp. 503–529, 2002.

[16] B. L. Smith and A. Glezer, "Jet vectoring using synthetic jets," *J. Fluid Mech.*, vol. 458, pp. 1–34, 2002.

[17] T. Suzuki, "Effects of a synthetic jet acting on a separated flow over a hump," *J. Fluid Mech.*, vol. 547, pp. 331–359, 2006.

[18] J. Dandois, E. Garnier, and P. Sagaut, "Numerical simulation if active separation control by a synthetic jet," *J. Fluid Mech.*, vol. 574, pp. 25–58, 2007.

[19] R. B. Kotapati, R. Mittal, and L. N. C. III, "Numerical study of a transitional synthetic jet in quiescent external flow," *J. Fluid Mech.*, vol. 581, pp. 287–321, 2007.

[20] M. Malik, L. Weinstein, and M. Hussani, "Ion wind drag reduction," AIAA Paper 83–0231, 21st AIAA Aerospace Sciences Meeting and Exhibit, Reno, NV, Jan. 1983.

[21] T. C. Corke and E. Maltis, "Phase plasma arrays for unsteady flow control," AIAA Paper 2000–2320, Fluids 2000, Denver, CO, 2000.

[22] J. D. Jacob, "Some experiments on boundary layer flow control using ac discharge plasma actuators," Air Force Summer Faculty Fellowship Program Final Report, AFRL, WPAFB, Aug. 2003.

[23] J. W. Baughn, C. O. Porter, B. L. Peterson, T. E. McLaughlin, C. L. Enloe, G. I. Font, and C. Baird, "Momentum transfer for an aerodynamic plasma actuator with an imposed boundary layer," AIAA Paper 2006–168, 44th AIAA Aerospace Sciences Meeting and Exhibit, Reno, NV, Jan. 2006.

[24] A. Labergue, L. Leger, E. Moreau, and G. Touchard, "Effect of a plasma actuator on an airflow along an inclined wall: P.i.v and wall pressure measurements,"

[25] T. C. Corke and M. L. Post, "Overview of plasma flow control: Concepts, optimization, and applications," AIAA Paper 2005–563, 43rd AIAA Aerospace Sciences Meeting and Exhibit, Reno, NV, Jan. 2005.

[26] M. L. Post and T. C. Corke, "Flow control with single dielectric barrier plasma actuators," AIAA Paper 2005–4630, 35th AIAA Fluid Dynamics Conference and Exhibit, Toronto, Ontario, Canada, June 2005.

[27] T. C. Corke and B. Mertz, "Plasma flow control optimized airfoil," AIAA Paper 2006–1208, 44 th AIAA Aerospace Sciences Meeting and Exhibit, Reno, NV, Jan. 2006.

[28] J. Lopera, T. T. Ng, M. P. Patel, S. Vasudevan, and T. C. Corke, "Aerodynamic control of 1303 uav using windward surface plasma actuators on a separation ramp," AIAA Paper 2007–0636, 45th Aerospace Sciences Meeting and Exhibit, Reno, NV, Jan. 2007.

[29] C. Porter, T. McLaughlin, C. Enloe, G. Font, J. Roney, and J. Baughn, "Boundary layer control using a dbd plasma actuator," AIAA Paper 2007–0786, 45th Aerospace Sciences Meeting and Exhibit, Reno, NV, Jan. 2007.

[30] N. Benard, J. P. Bonnet, G. Touchard, and E. Moreau, "Flow control by dielectric barrier discharge actuators: Jet mixing enhancement," *AIAA Journal*, vol. 46, no. 9, 2008.

[31] C. L. Enloe, T. E. McLaughlin, R. D. VanDyken, K. D. Kachner, E. J. Jumper, and T. C. Corke, "Mechanisms and responses of a single dielectric barrier discharge plasma actuator: Plasma morphology," *AIAA Journal*, vol. 42, no. 3, pp. 589–594, 2004.

[32] C. L. Enloe, T. E. McLaughlin, R. D. VanDyken, K. D. Kachner, E. J. Jumper, T. C. Corke, M. Post, and O. Haddad, "Mechanisms and responses of a single

dielectric barrier discharge plasma actuator: Geometric effects," *AIAA Journal*, vol. 42, no. 3, pp. 595–604, 2004.

[33] N. Benard and N. Balcon, "Electric wind produced by a single dielectric barrier discharge actuator operating in atmospheric flight conditions-pressure outcome," AIAA Paper 2008–3792, 39th Plasmadynamics and Lasers Conference, Seattle, WA, 2008.

[34] N. Benard, N. Balcon, and E. Moreau, "Electric wind produced by a surface dielectric barrier discharge operating over a wide range of relative humidity," AIAA Paper 2009-488, 47th Aerospace Sciences Meeting and Exhibit, Orlando, FL, Jan. 2009.

[35] C. L. Enloe, G. I. Font, T. E. McLaughlin, and D. M. Orlov, "Surface potential and longitudinal electric field measurements in the aerodynamic plasma actuator," *AIAA Journal*, vol. 46, pp. 2730–2740, Nov. 2008.

[36] C. L. Enloe, M. G. McHarg, and G. I. Font, "Plasma-induced force and self-induced drag in the dielectric barrier discharge aerodynamic plasma actuator," AIAA Paper 2009-1622, 47th Aerospace Sciences Meeting and Exhibit, Orlando, FL, Jan. 2009.

[37] J. R. Roth, D. M. Sherman, and S. P. Wilkinson, "Boundary layer flow control with a one atmosphere uniform glow discharge plasma," AIAA Paper 98–0328, 36th AIAA Aerospace Sciences Meeting and Exhibit, Reno, NV, Jan. 1998.

[38] J. R. Roth, X. Dai, J. Rahel, and D. M. Shermann, "The physics and phenomenology of paraelectric one atmosphere uniform glow discharge plasma (OAUGDP) actuators for aerodynamic flow control," AIAA Paper 2005–781, 43rd AIAA Aerospace Sciences Meeting and Exhibit, Reno, NV, Jan. 2005.

[39] J. R. Roth and X. Dai, "Optimization of the aerodynamic plasma actuator as an electrohydrodynamic (ehd) electrical device," AIAA Paper 2006–1203, 44th AIAA Aerospace Sciences Meeting and Exhibit, Reno, NV, Jan. 2006.

[40] R. Rivir, A. White, C. Carter, and B. Ganguly, "Ac and pulsed plasma flow control," AIAA Paper 2004–0847, 42 nd AIAA Aerospace Sciences Meeting and Exhibit, Reno, NV, Jan. 2004.

[41] C. O. Porter, J. W. Baughn, T. E. McLaughlin, C. L. Enloe, and G. I. Font, "Temporal force measurements on an aerodynamic plasma actuator," AIAA Paper 2006–104, 44th AIAA Aerospace Sciences Meeting and Exhibit, Reno, NV, Jan. 2006.

[42] C. L. Enloe, T. E. McLaughlin, and G. I. Font, "Frequency effects on the efficiency of the aerodynamic plasma actuator," AIAA Paper 2006–166, 44 th AIAA Aerospace Sciences Meeting and Exhibit, Reno, NV, Jan. 2006.

[43] T. Abe, Y. Takizawa, and S. Sato, "A parametric experimental study for momentum transfer by plasma actuator," AIAA Paper 2007–187, 45st AIAA Aerospace Sciences Meeting and Exhibit, Reno, NV, Jan. 2007.

[44] J. W. Gregory, C. L. Enloe, G. I. Font, and T. E. McLaughlin, "Force production mechanisms of a dielectric-barrier discharge plasma actuator," AIAA Paper 2007–0185, 45th Aerospace Sciences Meeting and Exhibit, Reno, NV, Jan. 2007.

[45] A. V. Likhanskii, M. N. Sheneider, S. O. Macheret, and R. B. Miles, "Optimization of dielectric barrier discharge plasma actuators driven by repetitive nanosecond pulses," AIAA Paper 2007–633, 45 th AIAA Aerospace Sciences Meeting and Exhibit, Reno, NV, Jan. 2007.

[46] D. F. Opaits, S. H. Zaidi, M. N. Shneider, R. B. Miles, A. V. Likhanskii, and S. O. Macheret, "Improving thrust by suppressing charge build-up in pulsed dbd

plasma actuators," AIAA Paper 2009-487, 47th Aerospace Sciences Meeting and Exhibit, Orlando, FL, Jan. 2009.

[47] A. R. Hoskinson and N. Hershkowitz, "2-d simulations of single and double dbd plasma actuators with finite electrode thickness," AIAA Paper 2009-484, 47th Aerospace Sciences Meeting and Exhibit, Orlando, FL, Jan. 2009.

[48] A. R. Hoskinson and N. Hershkowitz, "Comparisons of force measurement methods for dbd plasma actuators in quiescent air," AIAA Paper 2009-485, 47th Aerospace Sciences Meeting and Exhibit, Orlando, FL, Jan. 2009.

[49] A. Santhanakrishnan, K. Ramakumar, and J. D. Jacob, "Characteristics of a plasma synthetic jet," ORAL PRESENTATION, Bulletin of the American Physical Society Fluid Dynamics Division, Annual Meeting, Nov. 2005.

[50] T. Segawa, H. Furutani, H. Yoshida, T. Jukes, and K.-S. Choi, "Wall normal jet under elevated temperatures produced by surface plasma actuator," AIAA Paper 2007–0784, 45th Aerospace Sciences Meeting and Exhibit, Reno, NV, Jan. 2007.

[51] C. Porter, A. Abbas, K. Cohen, T. McLaughlin, and C. Enloe, "Spatially distributed forcing and jet vectoring with a dielectric barrier discharge plasma actuator," AIAA Paper 2008–1374, 46th Aerospace Sciences Meeting and Exhibit, Reno, NV, Jan. 2008.

[52] N. Benard, J. Jolibois, G. Touchard, and E. Moreau, "A directional plasma-jet device generated by double dbd actuators - an active vortex generator for aerodynamic flow control," AIAA Paper 2008–3763, 4th Flow Conference, Seattle, WA, 2008.

[53] M. Bolitho and J. Jacob, "Thrust vectoring flow control using plasma synthetic

jet actuators," AIAA Paper 2008–1429, 46th Aerospace Sciences Meeting and Exhibit, Reno, NV, Jan. 2008.

[54] M. Bolitho, "Jet vectoring and vorticity generation using plasma actuators," Master's thesis, Oklahoma State University, Stillwater, Oklahoma, May 2008.

[55] M. Sholl and Ö. Savaş, "A fast lagrangian PIV method for study of general high-gradient flows," AIAA Paper 1997–0493, 35th AIAA Aerospace Sciences Meeting, Reno, NV, Jan. 1997.

[56] L. Tsuei and Ö. Savaş, "Treatment of interfaces in particle image velocimetry," *Experiments in Fluids*, vol. 29, pp. 203–214, 2000.

[57] J. Harlan and D. Smith, "An experimental study of an annular jet with zero blockage ratio," 60th Annual Meeting of the American Physical Society Divison of Fluid Dynamics, Salt Lake City, UT, Nov. 2007.

[58] J. C. Bera, M. Michard, N. Grosjean, and G. Comte-Bellot, "Flow analysis of two-dimensional pulsed jets by particle image velocimetry," *Experiments in Fluids*, vol. 31, pp. 519–532, 2001.

[59] A. S. Santhanakrishnan, *Characterization and Flow Physics of Plasma Synthetic Jet Actuators.* PhD thesis, University of Kentucky, 2007.

[60] B. L. Smith and A. Glezer, "The formation and evolution of synthetic jets," *Phys. Fluids*, vol. 10, pp. 2281–2297, Sept. 1998.

[61] H. Schlichting and K. Gersten, *Boundary Layer Theory.* New York: Springer-Verlag, 8 ed., 2000.

[62] J. Jacob and A. Santhanakrishnan, "Scaling of plasma synthetic jet actuators," *59th Annual Meeting of the American Physical Society Divison of Fluid Dynamics, Tampa Bay, FL, Nov. 2006.*

VITA

Arzu Ceren Öztürk

Candidate for the Degree of

Doctor of Philosophy

Thesis: NOVEL APPLICATIONS OF PLASMA ACTUATORS

Major Field: Mechanical & Aerospace Engineering

Biographical:

Personal Data: Born in Antalya, TURKEY on September 19, 1986.

Education:

Received B.S. degree from Middle East Technical University, Ankara, TURKEY, 2007, in Aerospace Engineering

Completed the requirements for the degree of Master of Science with a major in Mechanical & Aerospace Engineering at Oklahoma State University in May, 2009.

Name: Arzu Ceren Öztürk Date of Degree: May, 2009

Institution: Oklahoma State University Location: Stillwater, Oklahoma

Title of Study: NOVEL APPLICATIONS OF PLASMA ACTUATORS

Pages in Study: 147 Candidate for the Degree of Master of Science

Major Field: Mechanical & Aerospace Engineering

The current study investigates the effectiveness of two different dielectric barrier discharge plasma actuator configurations, a 3-D annular geometry for use in micro thrusters and internal duct aerodynamics and a jet vectoring actuator that acts as a vortex generator and flow control device. The first configuration consists of a closed circumferential arrangement which yields a body force when a voltage difference is applied across the inner and outer electrodes separated by a dielectric. The primary flow is driven by this zero-net mass flux jet at the wall that then entrains fluid in the core of the duct. PIV experiments in both quiescent flow and freestream are conducted on tubes of different diameters while varying parameters such as the modulation frequency, duty cycle and tunnel speed. The values of the induced velocities increase with the forcing frequency and duty cycle although there is a peak value for the forcing frequency after which the velocity and thrust decrease for each thruster. The velocities and thrust increase as the inner diameter of the tubes are increased while the velocity profiles show a great difference with the (l/d_i) ratio; recirculation occurs after going below a critical value. Experiments in the wind tunnel illustrate that the jet exit characteristics significantly change upon actuation in freestream flow but the effect tends to diminish with increasing inner diameters and tunnel speeds. Using staged arrays of these thrusters result in higher velocities while operating at both in phase and out of phase.

The jet vectoring configuration consists of a single embedded electrode separated from two exposed electrodes on either side by the dielectric. The embedded electrode is grounded while the exposed electrodes are driven with a high frequency high voltage input signal. PIV measurements of the actuator in a freestream show that vectoring the jet yields stronger vortices than a linear configuration and increasing the difference between the duty cycles of the channels increases the vortex strength. It is seen that while the vortex is barely visible at the leading edge with little strength, it grows significantly large in the streamwise direction and reaches its maximum strength around mid-chord locations while the circulation distribution shows that the bulk of the circulation is added here. The motion of the vortex along this direction illustrates a braiding phenomena that can be observed via flow visualizations. Streamwise PIV data for this configuration on a wing with a NACA 0012 airfoil is used to plot the reverse flow probability, which in turn reveals that the use of the jet vectoring actuator as a vortex generator jet does suppress separation, but the actuator tends to lose its efficacy with increasing tunnel speeds.

ADVISOR'S APPROVAL: Dr. Jamey Jacob